Development of a high-order MHD simulation code and its application to the study of magnetic turbulence driven by the magneto-rotational instability

博 士 論 文

Development of a high-order MHD simulation code and its application to the study of magnetic turbulence driven by the magneto-rotational instability

（高次精度 MHD シミュレーションコードの開発と
それを用いた磁気回転不安定性が駆動する磁気乱流の研究）

平井　研一郎

平成 28 年

Doctoral Thesis

Development of a high-order MHD simulation code and its application to the study of magnetic turbulence driven by the magneto-rotational instability

Kenichiro Hirai

Department of Geophysics
Graduate School of Science
Tohoku University

Thesis Committee Members

Associate Professor Yuto Katoh (Chair, Supervisor)
Associate Professor Naoki Terada
Professor Takahiro Obara
Professor Yasumasa Kasaba
Associate Professor Soshi Kawai
Associate Professor Atsushi Kumamoto

2016

博士論文

高次精度 MHD シミュレーションコードの開発と
それを用いた磁気回転不安定性が駆動する磁気乱流の研究

東北大学大学院理学研究科
地球物理学専攻

平井　研一郎

論文審査委員

加藤　雄人　准教授（指導教員・主査）
寺田　直樹　准教授
小原　隆博　教授
笠羽　康正　教授
河合　宗司　准教授
熊本　篤志　准教授

平成 28 年

Acknowledgment

Foremost, I would like to express the deepest appreciation to my supervisor, Associate Prof. Yuto Katoh for his continuous support. His advice, comments, and encouragement have been great help in my study. I would also like to express my gratitude to Associate Prof. Naoki Terada and Associate Prof. Soshi Kawai. I received a lot of helpful advice and suggestions on simulation and coding technique as well as physical consideration from them.

I am deeply grateful to Associate Prof. Atsushi Kumamoto, Emeritus Prof. Hiroshi Oya, and the late Prof. Takayuki Ono for their fruitful advice, suggestions, and encouragement. I also want to thank to Associate Prof. Yosuke Matsumoto, Assistant Prof. Takahiro Miyoshi, Dr. Takashi Minoshima, and Mr. Kota Hirabayashi for their helpful advice and suggestions on physical consideration and simulation techniques.

I extend my deep thanks to Prof. Yasumasa Kasaba, Prof. Takahiro Obara, Associate Prof. Hiroaki Misawa, Associate Prof. Isao Murata, Associate Prof. Takeshi Sakanoi for their valuable advice.

I wish to express my special thanks to members of the Space and Terrestrial Plasma Physics Laboratory for their constant encouragement.

This work was supported by Tohoku University Division for Interdisciplinary Advanced Research and Education.

Finally, I would like to express heartfelt thanks to my wife, Satomi, my parents, Yoshiaki and Akiko, and my sister and her husband, Yoko and Keichi for their continuous support and encouragement.

Abstract

In accretion disks, magneto-rotational instability (MRI) (Balbus & Hawley, 1991) makes the disk gas in the magnetic turbulent state and drives efficient mass accretion into a central star. MRI drives turbulence through the evolution of the parasitic instability (Goodman & Xu, 1994) which is related to both Kelvin-Helmholtz (K-H) instability and magnetic reconnection. Although previous numerical simulations identified the enhancement of parasitic instability (Lesur & Longaretti, 2011; Murphy & Pessah, 2015) and reported that the maximum growth wavenumber of parasitic instability at the first peak is larger value than analytical estimation (Rembiasz et al., 2016), the detailed process of driving magnetic turbulence and the role of small-scale flow on it are not fully revealed.

We investigate the driving mechanism of the magnetic turbulence via the MRI and parasitic instability in accretion disks, and reveal the role of small-scale waves and flow structures for it by using the newly developed high-order MHD simulation code. We developed the MHD simulation code by employing the MHD scheme proposed by Kawai (2013). This scheme is based on the high-order compact difference scheme (Lele, 1992) and high-order compact-type filtering scheme (Lele, 1992; Gaitonde & Visbal, 2000), and localized artificial diffusivity (LAD) method. To parallelize without diminishing the accuracy, we also employ pipeline algorithm. We carried out some numerical tests and confirmed that the developed code has following capabilities; high wavenumber accuracy, capturing discontinuities accurately, and the conservation of the solenoidal condition. From these numerical tests, we could confirm that developed code works properly and has the capabilities for resolving MRI-driven turbulence.

We apply the developed code to the local disk model by using the shearing box approximation (Hawley et al., 1995), and carry out three-dimensional ideal MHD simulation of MRI-driven turbulence. We define the initial saturation of the turbulent stress as 'first peak' and arbitrarily chosen peak in fully developed phase as 'nonlinear peak', and investigate detailed structure at these two peaks. We show

the anisotropic wave enhancement in two-dimensional wavenumber spectra of vertical velocity due to the excitation of parasitic instability at the first peak. The fastest enhancement wavenumber is much larger than that obtained analytically.We find that this feature is because the interaction of vertically located growing vortices induced by parasitic instability makes the layered structure of disturbed flow narrower and faster, and then the jet-like structure induces much smaller and faster growing K-H-like instability just before the peak. We also show the analysis results of the arbitrarily chosen nonlinear peak. The anisotropic wave enhancement of parasitic instability is observed in two-dimensional wavenumber spectra of vertical velocity only at the small wavenumber region. This indicates that a nonlinear peak is created in an environment where large-scale and anisotropic parasitic mode waves and isotropic turbulent waves coexist. The restructured channel flow starts to collapse at the nonlinear peak, but the mechanism is not obvious. We show that large-scale vortices induced by restructured flow effectively advect small-scale shear structures from the shear region toward the flow region of the restructured channel, and the advected structure seems to mix and break the restructured channel structure. We determine that the peak creation and driving magnetic turbulence mechanism, i.e., the collapse mechanism of channel flow structure, is related to the destruction of large-scale structure by small-scale flow in both linear phase and nonlinear phase.

Next, we investigate the physical diffusion effects to the turbulent stress and peak creation mechanism. We carry out three-dimensional MHD simulations with changing initial Reynolds number Re and initial magnetic Reynolds number Rm. The time evolution of turbulent stresses until the first peak take almost the same value in the case of lower diffusivities. On the other hand, the turbulent stress at the first peak in the larger viscosity cases ($Re \sim 1$) take larger values. This trend should reflect the quenching effect of K-H instability analytically shown by Pessah & Goodman (2009) and Pessah (2010). The time evolutions of stress after the first peak are different in all diffusivity models. To see the trend of the values of the first peak, nonlinear peak, and temporally averaged value, we investigate these values in Re and Rm space. In the strong diffusivity cases ($Re, Rm \sim 1$), the viscosity increases the peak value at not only first peak but also peaks in nonlinear phase and the magnetic diffusivity increases the value only at first peak and does not affect (or decreases) the nonlinear peaks. On the other hand, there is no trend of nonlinear peaks and averaged values in lower diffusivity cases ($Re, Rm \geq 100$). The dependence of magnetic Prandtl number is also not identified in our

calculation, unlike Lesur & Longaretti (2007). The possible cause of this different feature from previous study is the setting of aspect ratio of the simulation box. We investigate detailed structure of the flow and its difference in several diffusivity models. At the first peak, wave enhancement of v_z directing 45 degrees from radial direction is observed in two-dimensional wavenumber space in $Re = Rm = 1000$ and $Re = Rm = 100$ diffusivity models. The direction of wave enhancement of B_z in the condition of $Re = Rm = 100$ is not 45 degrees but approximately 135 degrees. In the case of $Re = Rm = 10$ model, not only B_z but also v_z have 135 degrees anisotropy. Theses results indicate that the dominant mode of parasitic instability is modified from K-H mode to magnetic reconnection mode. The fastest growth wavenumber in the condition of $Re = Rm = 1000$ is larger than the theoretically obtained fastest growth wavenumber. This wavenumber slightly becomes small in the condition of $Re = Rm = 100$, and takes a similar value to the theoretical wavenumber of parasitic instability in the condition of $Re = Rm = 10$. These results indicate that the viscous effect controls fastest growth wavelength at the first peak. From above results and discussions, we conclude the diffusion terms modify the distribution of wavenumber spectra at the first peak though the linear property of MRI is almost similar. We also show the analysis result at the nonlinear peak, which is arbitrarily chosen peak in fully developed turbulence. The 2-dimensional wavenumber spectra of both v_z and B_z at the nonlinear peak have 45 degree wave enhancement in all the $Re = Rm = 1000$, 100, and 10 models. The difference between these three models are appeared as whether or not the smaller scale turbulent flow coexist. We confirm that the smoothing effects due to diffusivities slightly increases the value of nonlinear peak in relatively high diffusivity model such as $Re = Rm = 10$. On the other hand, we conclude that smoothing effect hardly modify the value of nonlinear peak in relatively low diffusivity model such as $Re = Rm = 100$ and 1000.

From our simulation and analysis, the excited structure of parasitic instability at the first peak is changed relatively largely due to the diffusion effect, but in the nonlinear peak, the diffusion effects hardly affect to both the average value of the stress and the structures of wavenumber spectra related to parasitic instability.

Contents

Chapter 1

Introduction

1.1 Accretion disks

Accretion disks are one of the most important and fundamental astronomical objects in the universe. Accretion disks are the disk structure existing around the massive central body, such as black holes, neutron stars, active galactic nuclei, protostars, and so on. In particular, the accretion disks around protostars are much denser and colder than others, and so called protoplanetary disks. Figure 1.1 shows (a) the accretion disk around active galactic nucleus NGC 4261 observed by Hubble Space Telescope (Jaffe et al., 1993) and (b) the protoplanetary disk in Orion nebula observed by Hubble Space Telescope (McCaughrean & O'dell, 1996). The

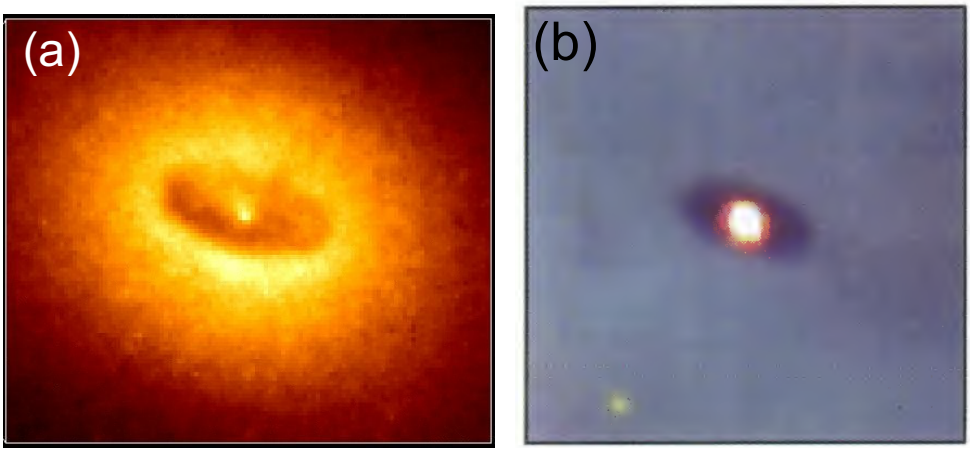

Fig. 1.1: Panel (a): The accretion disk around active galacic nucleus NGC 4261 (Jaffe et al., 1993). Panel (b): the protoplanetary disk in Orion nebula (McCaughrean & O'dell, 1996). Both are taken by Hubble Space Telescope.

bright points of both panels represent the central massive bodies and the surrounding dark disk structures are the accretion disk and protoplanetary disk. Although the size, gas density, and energy are much different between the accretion disks around the active galactic nucleus or black hole and the protoplanetary disks, the fundamental physics are considered to be basically resemble.

The disks are basically maintained by the force balance of the gravitational force and centrifugal force, thus the angular velocity of disk is Keplerian angular velocity written as

$$\Omega_{\rm K} = \sqrt{\frac{GM}{r^3}} \propto r^{-\frac{3}{2}}, \tag{1.1}$$

where r, M, and G represent the radius from the central body, mass of the central body, and gravitational constant, respectively. The angular velocity is sometimes slightly modified due to the presence of the global pressure gradient force though disk gas is usually considered to be rotating with $\Omega_{\rm K}$. For this reason, the radial distribution of angular velocity is often treated as $\Omega \propto r^{-q}$ in general, where q is a rotational parameter which corresponds to 3/2 for the Keplerian angular velocity. The rotational velocity $v_\phi = r\Omega$ becomes slower on the outside of the disk; this relation is so called differential rotation. While disk gas is basically balanced with gravitational force and centrifugal force, the large luminosity from accretion disks is observed, and thus it is believed that the disk gas is accreted toward central star because of the existence of viscosity in the differential rotating disk. Shakura & Sunyaev (1973) shows that mass accretion ratio $\dot{M}$ in such a differential rotating disk with viscosity written as

$$\dot{M} = -2\pi\Sigma\nu\frac{r}{\Omega}\frac{d\Omega}{dr}\left(1-\sqrt{\frac{r_{\rm in}}{r}}\right)^{-1}, \tag{1.2}$$

where Σ is the surface density defined as $\int_{-\infty}^{\infty}\rho dz$, ρ is gas density, z represents vertical direction of the disk, ν is kinematic viscosity which is assumed to be vertically constant, and $r_{\rm in}$ represents the radius of the inner boundary of accretion disks (see also Fukue et al., 2014). Considering that the disk gas is rotating with Keplerian angular velocity, i.e., $\Omega = \Omega_{\rm K} \propto r^{-\frac{3}{2}}$, and r is much larger than $r_{\rm in}$, Equation (1.2) becomes

$$\dot{M} \sim 3\pi\Sigma\nu. \tag{1.3}$$

The estimated mass accretion rate calculated by using typical surface density and molecular viscosity in protoplanetary disks, such that $\Sigma \sim 10^3\,{\rm g\,cm^{-2}}$, $\nu = 2\times$

$10^5\,\mathrm{cm^2 s^{-1}}$ (see e.g., Armitage, 2007), becomes

$$\dot{M} \sim 1.9 \times 10^9\,\mathrm{g\,s^{-1}} \sim 3.0 \times 10^{-17}\,M_\odot\,\mathrm{yr^{-1}},$$

where $M_\odot$ denotes the mass of sun. The mass accretion rate obtained by observational studies is, however, $\sim 10^{-8\sim-6}\,M_\odot\,\mathrm{yr^{-1}}$ for protoplanetary disks (e.g., Hartmann et al., 1998; Hartmann, 2001), and $\sim 10^{-9}\,M_\odot\,\mathrm{yr^{-1}}$ for accretion disks around the white dwarfs and neutron stars (e.g., Balbus & Hawley, 1998). Thus, the molecular viscosity is insufficient for the explanation of the mass accretion rate. The probable source for mass accretion instead of molecular viscosity is the turbulent viscosity. To see what the turbulent viscosity is, we consider the incompressible momentum equation of MHD equations. We assume coordinate system whose x, y, and z coordinates correspond to the radial, azimuthal, and vertical direction of the accretion disk, and that coordinate system is rotating around the disk with angular velocity Ω. In this coordinate system, the incompressible momentum equation is written as

$$\rho\frac{\partial \boldsymbol{v}}{\partial t} + \boldsymbol{\nabla}\cdot\left[\rho\boldsymbol{v}\boldsymbol{v} - \frac{\boldsymbol{B}\boldsymbol{B}}{4\pi} + \left(p + \frac{B^2}{8\pi}\right)\boldsymbol{I}\right] = \boldsymbol{\nabla}\cdot\mathbf{R} + 2q\Omega^2\rho x\hat{\boldsymbol{e}}_x - 2\rho\boldsymbol{\Omega}\times\boldsymbol{v}, \quad (1.4)$$

where ρ, p, $\boldsymbol{v}$, and $\boldsymbol{B}$ are the density, pressure, velocity, and magnetic field, and x is radial distance from the coordinate center, and $\mathbf{R}$ is incompressible viscous stress tensor defined as

$$\mathrm{R}_{ij} \equiv \mu\left(\frac{\partial v_j}{\partial x_i} + \frac{\partial v_i}{\partial x_j}\right), \quad (1.5)$$

where μ is dynamic viscosity. We assume ρ and p are homogeneous. We decompose velocity and magnetic field into spatially averaged value with the disturbed component, i.e., $\boldsymbol{v} = \bar{\boldsymbol{v}} + \boldsymbol{v}'$ and $\boldsymbol{B} = \bar{\boldsymbol{B}} + \boldsymbol{B}'$, where over bar and dash respectively denote spatial averaged value and disturbed component, and spatially average over Equation (1.4). By applying this operation, Equation (1.4) can be rewritten to the equation of averaged value as

$$\begin{aligned}&\rho\frac{\partial \bar{\boldsymbol{v}}}{\partial t} + \boldsymbol{\nabla}\cdot\left[\rho\bar{\boldsymbol{v}}\bar{\boldsymbol{v}} - \frac{\bar{\boldsymbol{B}}\bar{\boldsymbol{B}}}{4\pi} + \left(p + \frac{\bar{B}^2}{8\pi}\right)\boldsymbol{I}\right]\\ &= \boldsymbol{\nabla}\cdot\bar{\mathbf{R}} + \boldsymbol{\nabla}\cdot\left[-\rho\left\langle\boldsymbol{v}'\boldsymbol{v}'\right\rangle + \frac{\left\langle\boldsymbol{B}'\boldsymbol{B}'\right\rangle}{4\pi} - \frac{\left\langle B'^2\right\rangle}{8\pi}\boldsymbol{I}\right] + 2q\Omega^2\rho x\hat{\boldsymbol{e}}_x - 2\rho\boldsymbol{\Omega}\times\bar{\boldsymbol{v}}.\end{aligned} \quad (1.6)$$

Here, we use relations of spatially averaging that are $\langle \bar{f} \rangle = \bar{f}$ and $\langle f' \rangle = \langle \bar{f} f' \rangle = 0$. Comparing the first and second terms of R.H.S. of Equation (1.6), it can be seen that the second term, which is composed by the products of disturbed components, works as the equivalent to the viscosity for the equation of spatially averaged momentum. From this fast, a dynamic turbulent viscosity $\mu_{\rm tur}$ can be defined to satisfy the following equation.

$$\mu_{\rm tur}\left(\frac{\partial \bar{v}_j}{\partial x_i} + \frac{\partial \bar{v}_i}{\partial x_j}\right) = \left\langle -\rho v_i' v_j' + \frac{B_i' B_j'}{4\pi} \right\rangle - \frac{\langle B'^2 \rangle}{8\pi}\delta_{ij}. \tag{1.7}$$

In the accretion disks, only the radial derivative of the azimuthal component of the averaged velocity has a finite value, i.e., only $\partial \bar{v}_y / \partial x \neq 0$. Therefore, Equation (1.7) can be rewritten for accretion disks as

$$-\rho \nu_{\rm tur} \frac{\partial \bar{v}_y}{\partial x} = \left\langle \rho v_x' v_y' - \frac{B_x' B_y'}{4\pi} \right\rangle \equiv \langle W_{xy} \rangle \,, \tag{1.8}$$

where $\nu_{\rm tur} = \mu_{\rm tur}/\rho$ is the kinematic turbulent viscosity, and $W_{xy} \equiv \rho v_x' v_y' - B_x' B_y'/4\pi$ is so called turbulent stress for accretion disks. Shakura & Sunyaev (1973) suggested that spatially averaged turbulent stress $\langle W_{xy} \rangle$ can be scaled by the density and sound speed c_s written as

$$\langle W_{xy} \rangle = \alpha \rho c_s^2, \tag{1.9}$$

where α is a dimensionless parameter that indicates the scale of turbulent stress. By using Equation (1.9), Equation (1.8) can be rewritten for $\nu_{\rm tur}$ as

$$\nu_{\rm tur} \sim \alpha c_s^2 / \Omega. \tag{1.10}$$

We can estimate the turbulent viscosity from Equation (1.10) by estimating the dimensionless parameter α, and α can be estimated from spatially averaged turbulent stress like $\alpha \simeq \langle W_{xy} \rangle / p$ (Equation (1.9)). By using the typical sound speed and angular velocity at 1AU that are $c_s \sim 1.5 \times 10^5 \,{\rm cm\,s^{-1}}$ and $\Omega = 2\pi {\rm yr}^{-1}$, and assuming $\alpha = 0.01$, the mass accretion rate calculated by turbulent viscosity becomes $\dot{M} \sim 1.5 \times 10^{-7}$. Therefore, the turbulent viscosity is the probable source for mass accretion instead of the molecular viscosity, and it is believed that the disk gas is in the magneto-hydrodynamic turbulent state to express the observed high mass accretion rate.

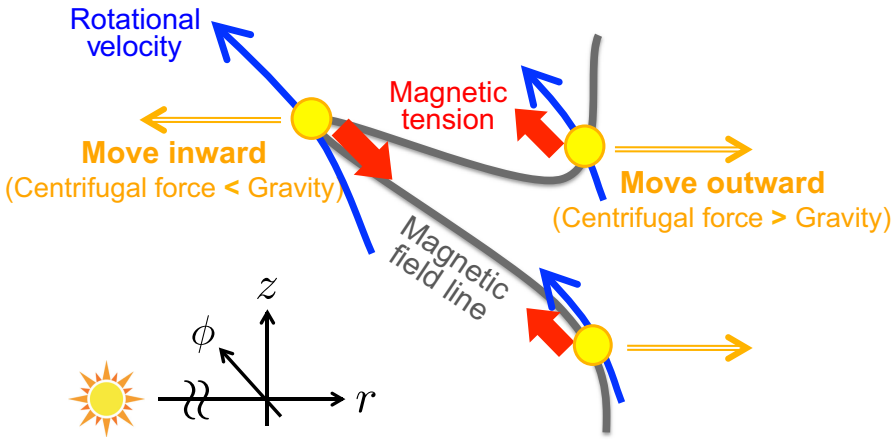

Fig. 1.2: The schematic image of the qualitative mechanism of MRI.

1.2 Magneto-rotational instability

The important point is the mechanism for increasing W_{xy}, i.e., the generation mechanism of horizontal components of the disturbed fields that are v'_x, v'_y, B'_x, and B'_y. Balbus & Hawley (1991) proposed that existence of rapidly and easily growing magneto-hydro dynamical instability called magneto-rotational instability (MRI) in accretion disks MRI is one of the most important sources of turbulence and grows in the following disk conditions; (1) the disk gas rotates with the differential rotational velocity (Ω^{-q}; $q > 0$), (2) the vertical magnetic field penetrates the disk, and (3) the disk gas is ionized and dense, i.e., MHD approximation is valid. Figure 1.2 shows the schematic image of the qualitative mechanism of MRI. When the differential rotating ionized disk gas penetrated by vertical magnetic field is disturbed radially, the rotational angular momentum is transported from the plasma disturbed to inside to the plasma disturbed to outside via the magnetic tension along the magnetic field line. This results in the violation of the balance between the centrifugal force and gravitational force, and thus the disturbance grows exponentially while stretching the magnetic field.

The reason why MRI is important in accretion disks is its large growth rate. In the Keplerian rotational disk with the ideal MHD condition, the growth rate of MRI becomes $0.75\Omega_{\rm k}$ (details will be described in Section 3.2), i.e., the small amplitude of disturbance becomes 100 times larger par one orbital period. The typical timescale of MRI, which is a few orbital periods, is basically much smaller

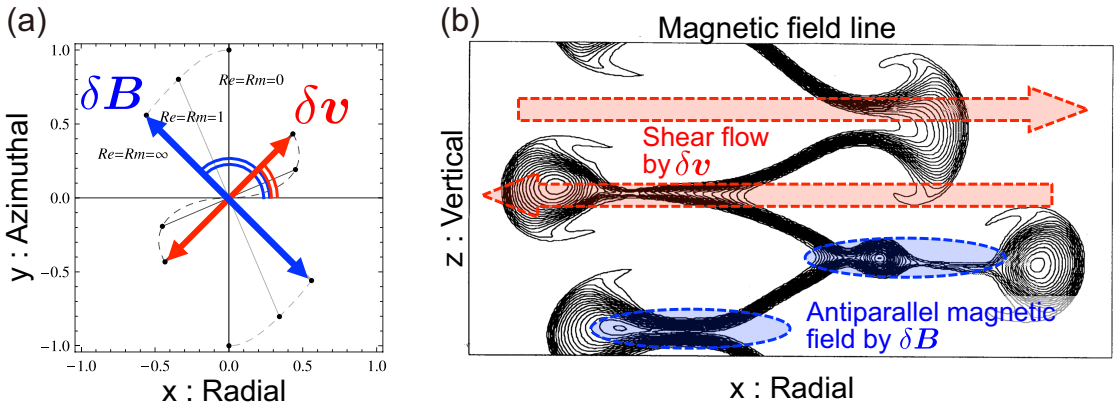

Fig. 1.3: The disturbed field vector and structure generated in and after the linear phase of MRI. Panel (a): the directions of disturbed velocity (red line) and magnetic field (blue line) in linear phase of MRI (Pessah & Chan, 2008, modified). Horizontal and vertical axes shows the radial and azimuthal direction, respectively. Panel (b): The result of 2-dimensional axisymmetric simulation of after the linear phase (Hawley & Balbus, 1992, modified). Lines show the magnetic field lines, and the horizontal and vertical axes show radial and vertical direction, respectively.

than the typical timescale of disk evolution which is about 10^6yr. Therefore, MRI is dominant phenomenon for considering the disk evolution and is considered playing an important role for driving the mass accretion by generating turbulent stress.

As described and illustrated above, MRI generates the horizontal disturbed flow and magnetic field by converting gravitational energy to those via the magnetic tension of vertical magnetic field. Previous studies showed that the accretion disk becomes eventually turbulent state as a result of MRI, and the structure generated by MRI is considered to play important roles for this transition mechanism from MRI to the turbulence. Figure 1.3 shows the disturbed field vector and structure generated in and after the linear phase of MRI. Panel (a) shows the directions of disturbed velocity $\delta\boldsymbol{v}$ (red line (ideal MHD)) and magnetic field $\delta\boldsymbol{B}$ (blue line (ideal MHD)) in the linear phase of MRI (Pessah & Chan, 2008, modified). Horizontal and vertical axes show the radial and azimuthal directions, respectively. In the ideal MHD condition, $\delta\boldsymbol{v}$ and $\delta\boldsymbol{B}$ direct toward 45 (225) degrees and 135 (315) degrees from radial direction, respectively. Note that these directions are modified by fluid viscosity and magnetic diffusivity. Details will be described in Section 3.2 and Section 4.2. Panel (b) shows the result of 2-dimensional axisymmetric simulation of MRI after the linear phase (Hawley & Balbus, 1992, modified). Lines show the magnetic field lines, and the horizontal and vertical axes show radial and vertical

directions, respectively. This is an axisymmetric simulation result, thus this plot is almost same as the projection of disturbed fields in panel (a) on the plane formed by the radial and vertical directions. MRI generates vertically sinusoidal structures of $\delta\boldsymbol{v}$ and $\delta\boldsymbol{B}$ whose phases are different by 90 degrees. The amplitude of these sinusoidal structures of $\delta\boldsymbol{v}$ and $\delta\boldsymbol{B}$ increase with time, and finally these structures can be treated as velocity shear flow and antiparallel magnetic field like panel (b). Therefore, MRI in the ideal condition generates the velocity shear and the antiparallel magnetic field created by the disturbance amount with the direction of 45 degrees and 135 degrees, respectively. The mechanism of driving magnetic turbulence from MRI is the parasitic instability (Goodman & Xu, 1994) that is strongly related to these shear flow and antiparallel magnetic field. Detailed property of MRI, such as dispersion relations and diffusivity dependence, will be described in Section 3.2 and Section 4.2.

1.3 Parasitic instability

Parasitic instabilities were firstly proposed by Goodman & Xu (1994) and are secondary instability induced by temporally increasing disturbed velocity shear and antiparallel magnetic field created by MRI. The velocity shear and antiparallel magnetic field drive the Kelvin-Helmholtz (K-H) instability and magnetic reconnection (tearing-mode instability). Parasitic instability is a generic term for these two instability and phenomena caused by the temporally increasing disturbed field created by MRI. In the case of ideal MHD condition, it is well-known that the magnetic reconnection is not driven, hence it can be expected that velocity shear drives K-H mode parasitic instability. Figure 1.4 shows thee dispersion relation of parasitic instability in Keplerian rotational disk with ideal MHD condition (Goodman & Xu, 1994, modified). Horizontal axis shows wavenumber k_h normalized by maximum growth wavenumber of MRI, where k_h is horizontal wavenumber along the direction of velocity shear, i.e., 45 degrees from radial direction. Vertical axis shows the product of growth rate of parasitic instability $\Im(\omega_{pi})$ normalized by rotational angular velocity and the inverse of amplified magnetic field of MRI B_{MRI} normalized by background magnetic field B_0. The normalized growth rate of parasitic instability is the value of the vertical axis times the normalized amplitude of magnetic field. Although there are three lines plotted depending on whether or not the parasitic mode has a large-scale vertical structure, Goodman & Xu (1994) shows that the case without vertical structure ($k_z = 0$) grows fastest. The

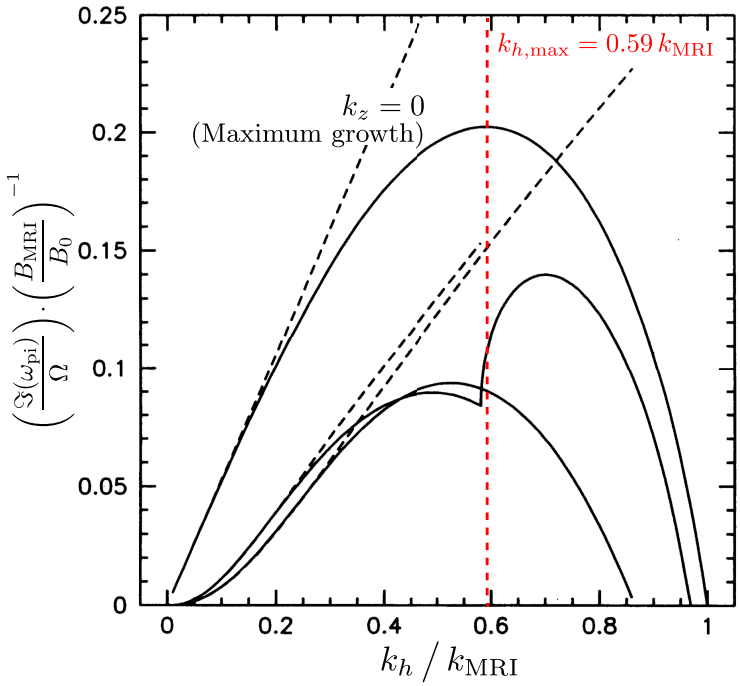

Fig. 1.4: The dispersion relation of parasitic instability in ideal MHD condition (Goodman & Xu, 1994, modified).

fastest growth wavenumber is 0.59 times the maximum wavenumber of MRI, i.e., the typical scale of parasitic instability is roughly twice as large. Figure 1.5 shows the approximate time evolution of the disturbance grown by parasitic instability (red) and MRI (blue). The horizontal axis and vertical axis represent the orbital time and normalized amplitude of magnetic field, respectively. The amplitude of disturbance grown by parasitic instability takes much lower value than that grown by MRI at first because the amplitude of MRI is still low and thus the growth rate of parasitic instability is also low. As the amplitude of disturbance grown by MRI increases with time, the growth rate of parasitic instability also increases, and the amplitude of parasitic instability grows in like a double exponential fashion, and finally both the growth rate and amplitude of disturbance of parasitic instability exceed those of MRI. It is considered that the induced K-H instability make the plasma turbulent state when the maximum growth rate of K-H mode parasitic instability exceeds the that of MRI (see also Pessah, 2010). Note that parasitic instability is non-axisymmetric instability, therefore, MHD simulation for solving MRI-driven turbulence need to be a three-dimensional calculation.

In the case that the plasma is not ideal MHD but visco-resistive MHD, the property of parasitic instability is modified because the magnetic diffusivity ex-

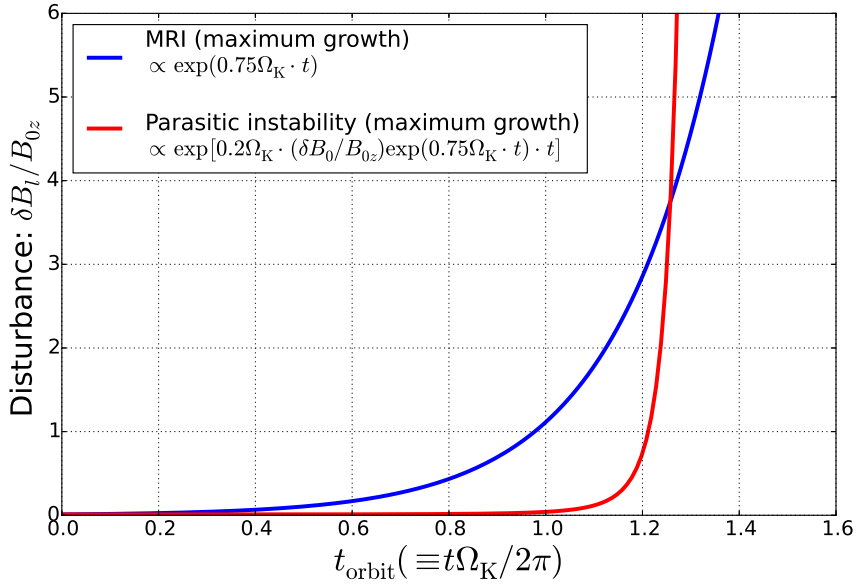

Fig. 1.5: Approximate time evolution of the disturbance grown by parasitic instability (red) and MRI (blue). The horizontal axis and vertical axis represent the time and amplitude, respectively.

cites the magnetic reconnection and the fluid viscosity quenches K-H instability. Pessah (2010) analytically shows that the direction of the wavenumber vector of the maximum growth mode of parasitic instability changes from that along the velocity shear to that along the antiparallel magnetic field as the magnetic diffusion is increased. This fact indicates the possibility that the diffusivity affects the generation process of MRI-driven turbulence.

1.4 Previous numerical studies about MRI-driven turbulence

As introduced above, MRI makes accretion disk turbulent state via K-H mode or magnetic reconnection mode parasitic instability. The nonlinear evolution of MRI-driven turbulence is studied by numerical simulation. Previous simulation studies are roughly divided into three categories; the local disk simulation, stratified disk simulation, and global disk simulation.

The global disk simulation is a simulation that solves entire region of accretion disk. This type of simulation can solve the radial, azimuthal, and vertical structures of accretion disks consistently, and also it can introduce the magnetic

field originated from central star. From these characteristics, the global simulation is used for investigating the mechanisms of protostellar core formation, star-disk interaction, jet creation, and so on (e.g., Romanova et al., 2011, 2012; Tomida et al., 2013; Machida, 2014). Much of previous global simulations were calculated with near the minimum number of grid resolution that can reproduce MRI or with the axisymmetric two-dimensional simulation domain because global simulations require the large simulation domain (and also complicated simulation method). Hence, although the global simulation can solve entire disks and works well for investigating the evolutional process of accretion disks, it is not suitable to investigate the detailed mechanism of driving turbulence via MRI and subsequent parasitic instability, and the fine structure of MRI-driven turbulence.

The stratified disk simulation is a simulation that solve the radial and azimuthal direction locally and vertical direction entirely. This type of simulation uses shearing box approximation (Hawley et al., 1995) and assumes vertically stratified density distribution, and can solve evolutional process of the vertical structure of the disk. Previous stratified simulations reported that there are phenomena caused by the vertical structure, such as the buoyancy (Parker) instability and resultant upwelling and repetitive evolution of toroidal magnetic field (so called butterfly diagram), vertical mass outflow (so called disk wind), and so on (e.g., Stone et al., 1996; Suzuki & Inutsuka, 2009; Shi et al., 2010). Stratified disk model is one of the good models for seeing the fine structure of turbulence while introducing a disk structure close to reality. There are, however, some numerical difficulties such as the high Alfven velocity at low-density region and the handling method for outgoing boundary condition at the vertical boundaries.

The local disk simulation is the most classical and fundamental model for the simulation of accretion disk. This type of simulation set the small simulation box in the local region of accretion disks by using the shearing box approximation Hawley et al. (1995), and doesn't think of the global structure in vertical direction. The local simulation enable us to set high grid resolution for typical scales of MRI because of the small simulation domain. Therefore, it is reasonable to use the local simulation for revealing the detailed mechanism of driving magnetic turbulence via the MRI and parasitic instability, and the fine structure of the MRI driven turbulence. Since the results of local three-dimensional simulation was reported by Hawley et al. (1995) first, a lot of simulations were performed under the various physical and numerical conditions. Previous numerical studies related to and focusing on the enhancement of parasitic instability and its contribution to drive the turbulence

are as follows. Hawley et al. (1995) reported that the stress creates the peaks in the nonlinear phase after the initial saturation of MRI, and Sano & Inutsuka (2001) pointed out that the shear flow whose wavelength corresponds to the vertical box size is recurrently generated in nonlinear phase and such structure creates peak. Sano & Inutsuka (2001) also suggested that the reconnection mode parasitic instability is excited at those peaks in resistive MHD condition, and the pointed out that numerical resistivity works a same role in their ideal MHD calculation. The enhancement of K-H mode parasitic instability was confirmed in two-dimensional wavenumber space by several studies. Lesur & Longaretti (2011) and Murphy & Pessah (2015) reported that wave enhancement is observed with a direction of wavenumber in which the radial wavenumber coincide with azimuthal wavenumber, i.e., 45 degrees from radial direction, in their incompressible MHD simulations. In particular, Murphy & Pessah (2015) shows that the anisotropy of wave enhancement is varied with time but it exists at both the early stage of nonlinear phase and fully turbulent phase. On the other hand, Latter et al. (2009) analytically and numerically suggested that the compressibility affected to the property of linear growth and structures at saturation. Their results of compressible simulation showed the shear flow created by MRI, so called channel flow, becomes narrower just before the saturation of linear growth because of the compressibility. Their results indicate the importance of including compressibility to the MHD simulation and also indicate the requirement of the ability for solving small-scale flow to the MHD simulation scheme. In fact, Rembiasz et al. (2016) carried out MHD simulation with the high-order compressible MHD scheme and reported that the enhancement of wave is observed with the direction in which the radial wavenumber coincide with azimuthal wavenumber at the saturation of MRI, and its fastest growth wavenumber is much smaller than the maximum growth wavenumber of parasitic instability. This result indicates that the structures smaller than the typical scales of MRI and parasitic instability play an important role in the transition process from MRI to turbulence via parasitic instability.

In addition to this, several studies focusing on the physical and numerical diffusivities also suggested that the importance of small-scale structures indirectly. Lesur & Longaretti (2007) and Fromang et al. (2007) carried out incompressible and compressible MHD simulations with small amount of physical viscosity and magnetic diffusivity, and showed that the time evolution of the spatially averaged turbulent stress is strongly affected by those diffusivities in nonlinear evolutional phase. In addition, Minoshima et al. (2015) carried out compressible ideal MHD

simulations by various simulation scheme, and showed that the difference of simulation scheme, i.e., difference of numerical diffusivities, also modify the time evolution of the spatially averaged turbulent stress. It is well known that small amount of diffusivities dissipate the small-scale waves and modify the small-scale structure of the flow and magnetic field. Therefore, these simulation results indicate the possibility that the small-scale wave and flow structures affect to the mechanism of driving turbulence and estimation of turbulent stress.

1.5 Purpose of this study

As mentioned above, recent studies suggested the importance of performing compressible MHD simulation that can solve the small-scale flow structures and waves accurately. However, it is difficult for MHD simulation to satisfy these requirements. This is because numerical diffusivity is indispensable for solving compressive phenomena such as shock waves, but on the other hand, it is necessary to reduce numerical diffusivity as much as possible in order to solve turbulent flow with high resolution. There are a lot of MHD simulation codes that employ various methods in order to cope this trade-off problem. Much of recent codes center on solving shock waves by employing Godunov-type shock capturing scheme and reduce their numerical diffusivity by employing high-order reconstruction method, and thus, these code can solve shock wave much accurately but can not reduce numerical diffusivities sufficiently.

Considering above points, our study consists of the following three parts.

1. Development of a high-order MHD simulation code:
   As describe above, existing open compressible MHD simulation codes don't have the efficiency for resolving small-scale waves and flow structures. Therefore, we newly develop a simulation code that employs the MHD simulation scheme proposed by Kawai (2013). This scheme has high accuracy for resolving waves by a few grid number and capturing shock wave by introducing physically problem-free numerical diffusivities at the vicinity of discontinuities.
2. Investigation of the enhancement of K-H mode parasitic instability and the role of small-scale flow for driving turbulence in ideal MHD condition:
   By applying newly developed MHD simulation code to the local disk simulation, we investigate the mechanism of driving magnetic turbulence via the MRI and parasitic instability, and the role of the small-scale waves and

flow structures in that process. We analyse the two-dimensional wavenumber spectra at the initial peak and the peak created in fully developed stage, and determine the dominant phenomena occurred at those peaks.

3. Investigation of the modification of small-scale flow and its contribution to the evolutional process of the turbulence by changing the viscosity and magnetic diffusivity: We investigate the modification of the time evolution of turbulent stress and contribution of the small-scale flow to it by changing the physical diffusion terms of viscosity and magnetic diffusivity. We analyze the statistical trend of the values at peaks and temporally averaged value of spatially averaged turbulent stress in the parameter space. Then, we analyze how the differences of the time evolution of turbulent stress occur by changing the small amount of diffusivity terms.

This thesis is organized as follows. In Chapter 2, we describe the overview of the newly developed MHD simulation code. In Chapter 3, we show the simulation results in ideal MHD condition calculated by the newly developed code. We describe the driving mechanism of turbulence via the MRI and parasitic instability and contributions of small-scale flow to that. In Chapter 4, we show the simulation results in visco-resistive MHD conditions with various viscosities and magnetic diffusivities. We show the trend of the turbulent stress in the parameter space, and describe how the modification of the time evolution occurs. We summarize this thesis in Chapter 5.

Chapter 2

Development of high-order MHD simulation code

2.1 Introduction

As described in chapter 1, the drive mechanism of magnetic turbulence by MRI in accretion disk is related to Kelvin-Helmholtz instability and magnetic reconnection. Kelvin-Helmholtz instability is well-known source of turbulence not only hydro-dynamics but also MHD (e.g., Matsumoto & Hoshino, 2004). Magnetic reconnection is also well-known mechanism to convert the magnetic energy to the kinetic energy. The structure of magnetic reconnection is complicated, especially Petcheck type reconnection (Zenitani & Miyoshi, 2011), but it is considered that the magnetic reconnection creates shock structure. To resolve the transition mechanism from MRI to the magnetic turbulence, it is required to resolve the turbulence and capture discontinuity structure simultaneously. However, it is difficult and challenging problem for the computational fluid dynamics. To resolve the turbulence accurately, MHD simulation schemes are required to be high-order, efficient for resolve waves by using lower grid number, i.e., a high wavenumber resolution, and less numerical diffusivity at the smoothed flow region. On the other hand, to capture the discontinuities and shocks robustly, MHD schemes also need to include numerical diffusivities because the numerical oscillation is occurred at the discontinuous surface in the calculation of derivatives without numerical diffusivities. These requirements are trade-off relation. Therefore, which methods are chosen for achieving high-order and high wavenumber resolution and for becoming robust at discontinuities are crucial points for carrying out the MHD simulation of MRI

driven turbulence.

Many of recent simulation studies use MHD schemes employing the shock capturing type scheme incorporated with the high-order reconstruction technique, for example CANS+(Matsumoto et al., 2016), ATHENA (Stone et al., 2008), PLUTO (Mignone et al., 2007), and so on. These schemes focus on accurately and robustly capturing shocks and discontinuities first, and become higher order by applying reconstruction technique. While these schemes can capture shocks and discontinuities very accurately because the enough numerical diffusivity is automatically embedded, the high order reconstruction techniques are complicated and cannot sufficiently suppress the numerical diffusivity to accurately resolve waves by using lower grid number. In this study, we use high-order MHD simulation scheme proposed by Kawai (2013). This scheme strongly focuses on resolving turbulence accurately by employing the high-order compact difference scheme (Lele, 1992) combined with the compact-type filtering scheme (Lele, 1992; Gaitonde & Visbal, 2000) and the localized artificial diffusivity method (Kawai, 2013). This scheme is categorized as the type of the non-diffusive differencing scheme combined with explicit artificial diffusivities. The characteristics of this scheme are that the numerical diffusivities are firstly calculated and introduced at the governing equation level, not the discretization level, and the high-order and high-wavenumber resolution differencing scheme is combined with that.

In this chapter, we introduce the newly developed code and its characteristics. In Section 2.2, we show the governing equations our code solves. In Section 2.3, we describe the compact differencing scheme which is the finite differencing scheme our code employs. In Section 2.4, we describe the localized artificial diffusivity (LAD) method for MHD proposed by Kawai (2013). In Section 2.5, we describe the parallelization method for the compact differencing scheme without diminishing the accuracy called pipeline algorithm. In Section 2.6, we show some numerical test problems for MHD and the application to some physical problems.

2.2 Governing equations

We consider the phenomena in accretion disks whose timescale is much larger than ion gyro-period and length scale is much larger than ion gyro radius. In addition to this, we consider that the mass of electron can be neglected and the disk gas is dense enough. Under these situations, we can assume that ions and electrons satisfy quasi-neutrality and the velocity distribution of plasma particles

keeps isotropic Maxwellian. Therefore, we can treat disk gas as MHD plasma with neglecting the particle effect of plasma, the hall effect, and the pressure anisotropy.

We factor in diffusive effects such as the magnetic diffusivity and the viscosity. As mentioned in Section 1.1, it is reported that magnetic diffusivity and viscosity become effective in the protoplanetaly disks (Sano et al., 2000) and collapser disk (Masada et al., 2007), and these terms change the property of linear growth of MRI (see Section 4.2). In addition, as described in Chapter 4, previous numerical studies reported that a small amount of magnetic diffusivity and viscosity changes non-linear evolution process of MRI-driven turbulence. These analytical and numerical previous studies indicate necessity of MHD simulation to include diffusive effects.

Following above facts, the equations that our simulation solves are following normalized visco-resistive MHD equations.

$$\frac{\partial \rho}{\partial t} + \boldsymbol{\nabla} \cdot (\rho \boldsymbol{v}) = \boldsymbol{\nabla} \cdot \boldsymbol{\mathcal{A}}_\rho, \tag{2.1}$$

$$\frac{\partial (\rho \boldsymbol{v})}{\partial t} + \boldsymbol{\nabla} \cdot \left[\rho \boldsymbol{v}\boldsymbol{v} - M_{\rm norm}^2 \boldsymbol{B}\boldsymbol{B} + \left(p + M_{\rm norm}^2 \frac{B^2}{2} \right) \boldsymbol{I} \right] = \frac{M_{\rm norm}}{Re_{\rm norm}} \boldsymbol{\nabla} \cdot \mathbf{R} + \boldsymbol{\nabla} \cdot [\boldsymbol{\mathcal{A}}_\rho \boldsymbol{v}] + \boldsymbol{S}_{\rm Momentum}, \tag{2.2}$$

$$\frac{\partial \boldsymbol{B}}{\partial t} + \boldsymbol{\nabla} \cdot (\boldsymbol{v}\boldsymbol{B} - \boldsymbol{B}\boldsymbol{v}) = \frac{M_{\rm norm}}{Rm_{\rm norm}} \boldsymbol{\nabla} \times (-\eta \boldsymbol{j}), \tag{2.3}$$

$$\frac{\partial E}{\partial t} + \boldsymbol{\nabla} \cdot \left[\left(E + p + M_{\rm norm}^2 \frac{B^2}{2} \right) \boldsymbol{v} - (\boldsymbol{v} \cdot M_{\rm norm}^2 \boldsymbol{B}) \boldsymbol{B} \right] = \frac{M_{\rm norm}}{Re_{\rm norm}} \boldsymbol{\nabla} \cdot [\mathbf{R} \cdot \boldsymbol{v}] + \frac{M_{\rm norm}}{Re_{\rm norm}} \boldsymbol{\nabla} \cdot [\boldsymbol{B} \times \eta \boldsymbol{j}] + \boldsymbol{\nabla} \cdot \left[\frac{1}{2} v^2 \boldsymbol{\mathcal{A}}_\rho \right] + S_{\rm Energy}, \tag{2.4}$$

where ρ, p, $\boldsymbol{v}$, $\boldsymbol{B}$, and η are the gas density, the pressure, the velocity field, the magnetic field, and the magnetic diffusivity, respectively. E is the total energy density defined as

$$E = \frac{p}{\gamma - 1} + \frac{\rho v^2}{2} + \frac{B^2}{2}, \tag{2.5}$$

where γ is specific heat. $\boldsymbol{j}$ is the current density written as

$$\boldsymbol{j} = \nabla \times \boldsymbol{B}, \tag{2.6}$$

and $\mathbf{R}$ is the viscous stress tensor defined as

$$\mathrm{R}_{ij} \equiv \mu \left(\frac{\partial v_j}{\partial x_i} + \frac{\partial v_i}{\partial x_j} \right) + \left(\beta - \frac{2}{3}\mu \right) \frac{\partial v_k}{\partial x_k} \delta_{ij}, \tag{2.7}$$

where μ and β are the shear viscosity and the bulk viscosity. $\boldsymbol{\mathcal{A}}_\rho$ is the artificial mass diffusive flux. This flux vector is completely artificial one originated by localized artificial diffusivity method to resolve contact discontinuities. We describe details of this flux vecter in Section 2.4. $\boldsymbol{S}_{\mathrm{Momentum}}$ and S_{Energy} in right-hand side of Equation (2.2) and Equation (2.4) are source terms. In this study, these source terms are used for introduce the shearing box coordinate system described in Section 3.3. Note that actual simulation of MRI uses one more equation and source terms of induction equation originated by the hyperbolic divergence cleaning method described in Section 3.3.

All physical values in above equations are normalized by respective normalization coefficient. Time, length, density, pressure, velocity, magnetic field, magnetic diffusivity, and shear viscosity are normalized by T, L, ρ_{norm}, p_{norm}, v_{norm}, B_{norm}, η_{norm}, and μ_{norm}, respectively, where the subscript "norm" represents that variables are normalization coefficients. We assume that bulk viscosity is normalized by same quantities as that for shear viscosity, i.e., μ_{norm}. M_{norm}, Re_{norm}, and Rm_{norm} are Alfven Mach number, Reynolds number, and magnetic Reynolds number, respectively, and defined as

$$M_{\mathrm{norm}} = \frac{v_{A\,\mathrm{norm}}}{c_{s\,\mathrm{norm}}}, \tag{2.8}$$

$$Re_{\mathrm{norm}} = \frac{\rho v_{A\,\mathrm{norm}} L}{\mu_{\mathrm{norm}}}, \tag{2.9}$$

$$Rm_{\mathrm{norm}} = \frac{v_{A\,\mathrm{norm}} L}{\eta_{\mathrm{norm}}}, \tag{2.10}$$

respectively, where $v_{A\,\mathrm{norm}}$ and $c_{s\,\mathrm{norm}}$ are the Alfven speed and sound speed calculated by normalization coefficient written as

$$v^2_{A,\,\mathrm{norm}} = B^2_{\mathrm{norm}}/4\pi\rho_{\mathrm{norm}}, \quad c_{s,\,\mathrm{norm}} = p_{\mathrm{norm}}/\rho_{\mathrm{norm}}, \tag{2.11}$$

respectively. In this study, we assume that the normalization coefficients follows

relations those are

$$L = v_{\rm norm} T, \tag{2.12}$$

$$p_{\rm norm} = \rho_{\rm norm} v_{\rm norm}^2 = B_{\rm norm}^2 / 4\pi = E_{\rm norm}, \tag{2.13}$$

$$\mu_{\rm norm} = \rho_{\rm norm} v_{A\,\rm norm} L, \tag{2.14}$$

$$\eta_{\rm norm} = v_{A\,\rm norm} L, \tag{2.15}$$

where $E_{\rm norm}$ denotes the normalization coefficient of total energy. By using these relations, $M_{\rm norm}$, $Re_{\rm norm}$, and $Rm_{\rm norm}$ all becomes unity, i.e., $M_{\rm norm} = Re_{\rm norm} = Rm_{\rm norm} = 1$. By determining the quantities of normalization coefficients satisfying these relations, we can translate a dimensionless simulation value to a dimensional actual value.

The coordinate system we use is Cartesian coordinate system (x, y, z). In this coordinate system, the vector fields $\boldsymbol{v}$, $\boldsymbol{B}$ can be written as

$$\boldsymbol{v} = (v_x, v_y, v_z), \quad \boldsymbol{B} = (B_x, B_y, B_z), \tag{2.16}$$

and the vector difference operator $\boldsymbol{\nabla}$ can be written as

$$\boldsymbol{\nabla} = (\partial/\partial x, \partial/\partial y, \partial/\partial z). \tag{2.17}$$

2.3 Compact difference and compact filtering scheme

In this section, we describe the compact difference scheme and compact-type filtering scheme. Compact difference scheme proposed by Lele (1992) is one of the central-type difference scheme and genuine expansion of the central difference scheme. The 6-th order tridiagonal family of compact difference scheme can be written as

$$\alpha \frac{\partial f_{i-1}}{\partial \xi_l} + \frac{\partial f_i}{\partial \xi_l} + \alpha \frac{\partial f_{i+1}}{\partial \xi_l} = a \frac{f_{i+1} - f_{i-1}}{2\Delta \xi_l} + b \frac{f_{i+2} - f_{i-2}}{4\Delta \xi_l} + c \frac{f_{i+3} - f_{i-3}}{6\Delta \xi_l}, \tag{2.18}$$

where i is the grid number, and ξ_l denotes the directions of 3-dimensional coordinate system, i.e., ξ_1, ξ_2, and ξ_3 represent x, y, and z in the simulation box

respectively. The coefficients a, b, and c are calculated as

$$a = \frac{\alpha + 9}{6},\ b = \frac{32\alpha - 9}{15},\ \text{and}\ c = \frac{-3\alpha + 1}{10}. \tag{2.19}$$

In the case choosing $\alpha = 0$, the differential equation becomes central difference. The truncation error of this scheme can be written as

$$\mathcal{O}(\Delta\xi_l^6) = \frac{12}{7}(-8\alpha + 3)f^{(7)}\Delta\xi_l^6 + \mathcal{O}(\Delta\xi_l^8). \tag{2.20}$$

Although the order of differential equation is normally 6-th order, Δx^6 order error can be eliminated when $\alpha = 3/8$ and the differential equation becomes 8-th order. Therefore, we can achieve 8-th order by using only 6 point stencils.

One of the most significant characteristics of compact difference scheme is its high efficiency of wavenumber precision. To show this efficiency, we do the stability analysis of compact difference. We consider the 1-dimensional wave advection in according with the advection equation. The advection equation can be written as

$$\frac{\partial f}{\partial t} + c\frac{\partial f}{\partial x} = 0, \tag{2.21}$$

where c is advection velocity, and the wave can be written as

$$f = \exp i(kx - \omega t), \tag{2.22}$$

where k is wavenumber, and ω is the complex angular frequency. We assume the periodic domain $[0, L]$ with the number of grid N. Under this assumption, we can transform coordinate x and wavenumber k with the equation that

$$x = n\Delta x, \quad k = \frac{2\pi}{L}\kappa, \tag{2.23}$$

where n is the grid number whose range is $[0, N-1]$, and κ is the wavenumber number whose range is $[0, N/2]$. By using these relations, Equation (2.22) can be rewritten as

$$f = \exp i\left(\frac{2\pi\Delta x\kappa}{L}n - \omega t\right) = \exp i(wn - \omega t), \tag{2.24}$$

where w is wavenumber par grid length defined as $w \equiv 2\pi\Delta x\kappa/L$ and its range is

$[0, \pi]$. The advection equation Equation (2.21) of this wave can be calculated to

$$-i\omega f + \frac{c}{\Delta x}\frac{\partial f}{\partial n} = 0. \tag{2.25}$$

Although the spatial derivation can be written as $\partial f/\partial n = iwf$ normally, this relation is not valid when we use the finite difference as the spatial derivation. We set modified w as w' which satisfies the relation that $(\partial f/\partial n)_{fd} = iw'f$, where the footnote fd means that the derivation is calculated by the finite difference scheme. By using this relation, the complex angular frequency ω can be written from Equation (2.25) as

$$\omega = \frac{c}{\Delta x}w'. \tag{2.26}$$

The modified wavenumber par grid length w' generally becomes complex value though w is real value. Therefore, the difference between $\Re(w')$ and w reflects the influence on the modification of the phase speed from analytical solution, and $\Im(w')$ reflects the numerical growth rate induced by introducing the finite difference. Lele (1992) showed the modified wavenumber par 1 grid w' of the equation of the tridiagonal compact difference Equation (2.18) as the function of w, that is

$$w'(w) = \frac{a\sin(w) + (a/2)\sin(2w) + (c/3)\sin(3w)}{1 + 2\alpha\cos(w)}. \tag{2.27}$$

Figure 2.1 shows the relation between w' and w. There are plots of some central difference properties and some compact difference properties. The 'j' line is the exact differentiation, and thus a scheme that is on the 'j' line in a wide range shows high wavenumber resolution. To show the high efficiency of wavenumber precision of compact difference, we compare the lines of c: 6-th order central difference, e: 6-th order tridiagonal compact difference, and f: 8-th order tridiagonal compact difference. Comparing 6-th order tridiagonal compact difference with 6-th order central difference, it is obviously shown that compact difference scheme can solve wider range of wavenumber accurately though those two scheme have same order of accuracy. In addition to this, we compare 6-th order and 8-th order tridiagonal compact difference schemes. These two schemes have similar efficiency of wavenumber precision. In this study, we use 8-th order one because we want to solve 4-grid wave properly, i.e., we want to use the scheme whose $w' = w$ at $w = \pi/2$. Although 6-th order scheme almost satisfies this condition, it seems that the 8-th order one is safer to solve it.

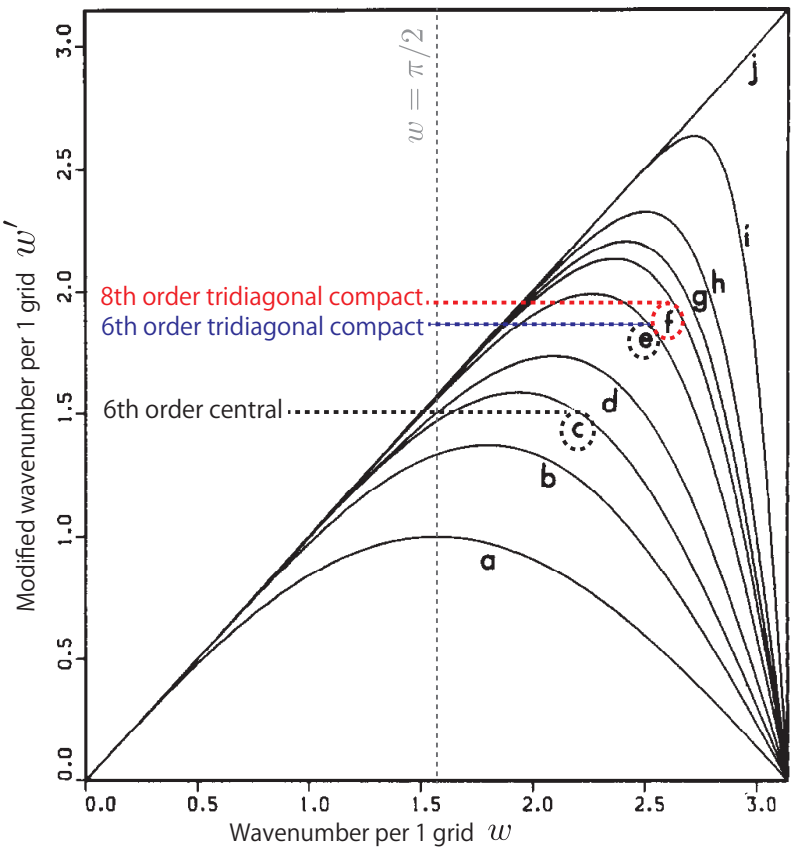

Fig. 2.1: Relation between the modified wavenumber per 1grid w' and original w. (Lele (1992) modified)

As described above, the compact difference scheme has a high efficiency for resolving waves. However, central type difference schemes cannot remove the high frequency numerical noise that is 2-grid wavelength wave because of the odd-even decoupling. Central type schemes use left and right side data symmetrically. Therefore, they cannot grasp the variation of the 2-grid wavelength wave, and thus these high frequency noisy waves can not be eliminated. To eliminate these noisy waves, the MHD scheme proposed by Kawai (2013) employs the 10-th order compact type low-pass filtering scheme proposed by Lele (1992) and Gaitonde & Visbal (2000). The 10-th order compact type low-pass filtering scheme can be written as

$$\alpha_f \tilde{f}_{i-1} + \tilde{f}_i + \alpha_f \tilde{f}_{i+1} = \sum_{n=0}^{5} \frac{a_n}{2}(f_{i+n} + f_{i-n}), \tag{2.28}$$

where $\tilde{f}$ represents the filterd value, and i is the grid number, and coefficients a_n

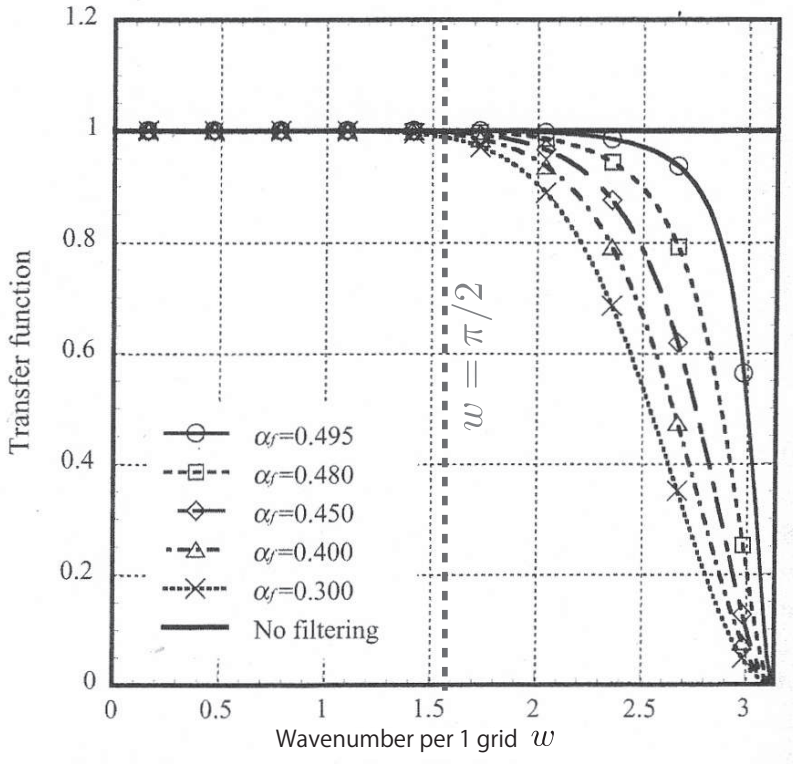

Fig. 2.2: The transfer function of the compact type low-pass filtering for w and its variation by changing the α_f. (Kawai & Lele (2008) modified)

is calculated as

$$a_0 = \frac{193 + 256\alpha_f}{256}, \quad a_1 = \frac{105 + 302\alpha_f}{256}, \quad a_2 = \frac{15(-1 + 2\alpha_f)}{64},$$
$$a_3 = \frac{45(1 - 2\alpha_f)}{512}, \quad a_4 = \frac{5(-1 + 2\alpha_f)}{256}, \text{ and } \quad a_4 = \frac{1 - 2\alpha_f}{512}. \tag{2.29}$$

The α_f is a free parameter whose range is $[-0.5, 0.5]$. Figure 2.2 shows the transfer function of the compact type low-pass filtering for the w and its variation by changing the α_f from 0.3 to 0.495 (Kawai & Lele, 2008). As shown in Figure 2.2, filtered range becomes narrow when the α_f increases. Similarly to above discussion, we choose $\alpha_f = 0.495$ to solve 4-grid wave properly, i.e., we use the scheme whose transfer function is unity at $w = \pi/2$. We apply this filter to the density, components of momentum, and total energy after the time integration by the Strong Stability Preserving Runge-Kutta method. Note that our code does not apply this low-pass filter to components of magnetic field. This is because the filtering to the magnetic field upsets the solenoidal condition of the magnetic field as mentioned by

Kawai (2013). Therefore, we admit the numerical oscillation only in the magnetic field.

The left hand sides of Equation (2.18) and Equation (2.28) contains the values which we want to know at the neighbor grids, i.e., the derivative values and filtered values at neighbor grids respectively. Therefore, solving the matrix equation is required to solve these equations. We rewrite Equation (2.18) as the matrix equation that is

$$\boldsymbol{A}\boldsymbol{f}' = \boldsymbol{b}, \tag{2.30}$$

where $\boldsymbol{f}'$ and $\boldsymbol{b}$ is the N-dimension vector of derivative values and right hand side of Equation (2.18) respectively. These vectors are composed by each grid in N-grids, i.e., $f'_i = (\partial f/\partial \xi_l)_i$ and $b_i = (\text{R.H.S. of Equation (2.18)})_i$ where $i = 1$ to N. $\boldsymbol{A}$ is a nearly tridiagonal matrix written as

$$\boldsymbol{A} = \begin{bmatrix} 1 & \alpha & & & & \alpha \\ \alpha & 1 & \alpha & & 0 & \\ & \ddots & \ddots & \ddots & & \\ & & \ddots & \ddots & \ddots & \\ & 0 & & \alpha & 1 & \alpha \\ \alpha & & & & \alpha & 1 \end{bmatrix}. \tag{2.31}$$

To solve this matrix equation for $\boldsymbol{f}'$, we apply LU decomposition to matrix $\boldsymbol{A}$. LU decomposition is the algorithm which convert a matrix to the product of the lower triangle $\boldsymbol{L}$ and upper triangle $\boldsymbol{U}$ matrices. Applying LU decomposition to $\boldsymbol{A}$, $\boldsymbol{A}$

can be transformed as

$$
\begin{aligned}
\boldsymbol{A} &= \boldsymbol{LU} \\
&= \begin{bmatrix}
1 & & & & \\
\ell_{2,1} & 1 & & & 0 \\
 & \ell_{3,2} & \ddots & & \\
0 & & \ddots & \ddots & \\
 & & & \ddots & 1 \\
\ell_{N,1} & \ell_{N,2} & \cdots & \cdots & \ell_{N,N-1}\ 1
\end{bmatrix}
\begin{bmatrix}
u_{1,1} & \alpha & & & & u_{1,N} \\
 & u_{2,2} & \alpha & & 0 & u_{2,N} \\
 & & u_{3,3} & \ddots & & \vdots \\
 & & & \ddots & \alpha & u_{N-2,N} \\
 & 0 & & & u_{N-1,N-1} & u_{N-1,N} \\
 & & & & & u_{N,N}
\end{bmatrix},
\end{aligned}
\tag{2.32}
$$

where $\ell_{i,j}$ and $u_{i,j}$ are components of the lower triangle and upper triangle matrix respectively, and those are calculated as

$$
u_{i,i} = \begin{cases} 1 & (i = 1) \\ 1 - \alpha\ell_{i,i-1} & (i = 2 \sim N-1), \end{cases}
$$

and

$$
\ell_{i,i-1} = \alpha / u_{i-1,i-1} \quad (i = 2 \sim N-1),
$$

and

$$
\ell_{N,i} = \begin{cases} \alpha & (i = 1) \\ -\alpha\ell_{N,i-1}/u_{i,i} & (i = 2 \sim N-2) \\ \alpha(1 - \ell_{N,i-1})/u_{i,i} & (i = N-1), \end{cases}
$$

and

$$u_{i,N} = \begin{cases} \alpha & (i = 1) \\ -\ell_{i,i-1} u_{i-1,N} & (i = 2 \sim N-2) \\ \alpha - \ell_{i,i-1} u_{i-1,N} & (i = N-1) \\ 1 - \sum_{k=1}^{N-1} \ell_{N,k} u_{k,N} & (i = N). \end{cases}$$

The rewritten matrix equation, that is

$$\boldsymbol{LU}\boldsymbol{f}' = \boldsymbol{b}, \tag{2.33}$$

can be calculated by 2-step sequential calculatoin. First, we put vector $\boldsymbol{a}$ as

$$\boldsymbol{a} = \boldsymbol{U}\boldsymbol{f}', \tag{2.34}$$

and thus Equation (2.33) becomes

$$\boldsymbol{L}\boldsymbol{a} = \boldsymbol{b}. \tag{2.35}$$

This matrix equation can be solved for $\boldsymbol{a}$ by sequentially solving and substituting from a_1 to a_N because $\boldsymbol{L}$ is the lower triangle matrix. This operation is called forward substitution. Then, we solve the Equation (2.34) for $\boldsymbol{f}'$ by sequentially solving and substituting from f'_N to f'_1 by using the property of the upper triangle matrix $\boldsymbol{U}$. This operation is called backward substitution. The good point to use LU decomposition for solving Equation (2.30) is its priory calculation for matrix. The number of the kind of matrices that our simulation uses is only two, the matrix for compact difference and the matrix for compact filtering. And we repeatedly use these two matrices for obtaining derivative and filtered values of various physical quantities. The amount of calculation for solving Equation (2.30) by LU decomposition, forward substitution, and backward substitution is correspond to the one by using Gauss's elimination method. In our simulation, a lot of physical quantities are differentiated by compact difference by same calculation. By solving Equation (2.30) with LU decomposition in that case, the calculation of lower triangle $\boldsymbol{L}$ and upper triangle $\boldsymbol{U}$ by LU decomposition can be carried out before entering the time integration loop only once and we can use same $\boldsymbol{L}$ and $\boldsymbol{U}$ again and again in the time integration loop. Therefore, we can reduce the amount of calculation in the time integration loop.

2.4 Localized artificial diffusivity method

The compact scheme is one of the central-type differencing scheme and thus this scheme does not contains numerical diffusivity. As mentioned at the head of this chapter, the numerical oscillation is occurred at the discontinuity on the calculation of derivation by using this scheme without the artificial diffusivities. Kawai (2013) proposed the Localized Artificial Diffusivity (LAD) method as a artificial diffusivity for any linear finite difference scheme in MHD simulation. The LAD method for MHD is extended method from the one for the hydro dynamics (Kawai & Lele, 2008; Kawai et al., 2010; Terashima et al., 2013). The characteristic of this method is that the numerical diffusivities are firstly calculated and introduced to the governing equations as the bulk viscosity, the magnetic diffusivity, and the mass diffusivity. The LAD method adds artificial diffusivities to the bulk viscosity for capturing hydrodynamic shocks, the magnetic diffusivity for capturing magneto-hydrodynamic discontinuities, and mass diffusive flux for capturing contact discontinuities in governing equations Equation (2.1) to Equation (2.7), so that

$$\beta = \beta_{\mathrm{phys}} + \beta_{\mathrm{art}}, \quad \eta = \eta_{\mathrm{phys}} + \eta_{\mathrm{art}}, \text{ and } \boldsymbol{\mathcal{A}}_\rho = \chi_{\mathrm{art}} \boldsymbol{\nabla} \rho, \tag{2.36}$$

where the quantities with subscript 'phys' denote the physical quantities, and the ones with 'art' denote the artificial quantities. Mani et al. (2009) shows the efficiency of using artificial bulk viscosity for capturing shock structure. The vorticity equation and dilatation equation in compressible flow with artificial bulk viscosity can be written as

$$\frac{\partial(\boldsymbol{\nabla} \times \boldsymbol{v})}{\partial t} = RHS_{\mathrm{phys}} - \frac{\boldsymbol{\nabla}\rho}{\rho^2} \times \boldsymbol{\nabla} \left[\beta_{\mathrm{art}} (\boldsymbol{\nabla} \cdot \boldsymbol{v})\right], \tag{2.37}$$

$$\frac{\partial(\boldsymbol{\nabla} \cdot \boldsymbol{v})}{\partial t} = RHS_{\mathrm{phys}} - \boldsymbol{\nabla} \cdot \left[\frac{1}{\rho} \boldsymbol{\nabla} \left[\beta_{\mathrm{art}} (\boldsymbol{\nabla} \cdot \boldsymbol{v})\right]\right], \tag{2.38}$$

where the RHS_{phys} denotes the physical right-hand side of each equation. The second term of right-hand side of Equation (2.37) works the diffusion effect of vorticity, hence this term should be small so as to prevent damping of turbulence. When the β_{art} is designed to appear only at the vicinity of the shock, this term becomes small at both the shock structure and the turbulent structure because $\boldsymbol{\nabla}\rho$ and $\boldsymbol{\nabla} \left[\beta_{\mathrm{art}} (\boldsymbol{\nabla} \cdot \boldsymbol{v})\right]$ are parallel near the shock and β_{art} and $\boldsymbol{\nabla} \cdot \boldsymbol{v}$ are small in

turbulent region. The second term of right-hand side of Equation (2.38) works the diffusion effect of dilatation of the flow, hence this term should be effective only at the vicinity of shock for diffusing the steep structure. When the $\beta_{\rm art}$ is designed to be effective only at the vicinity of the shock, this term becomes large only near the shock because both the $\beta_{\rm art}$ and $\boldsymbol{\nabla}\cdot\boldsymbol{v}$ are arose there, and thus the steep shock structure is diffused. Kawai (2013) also shows the efficiency of using artificial magnetic diffusivity for capturing magneto-hydrodynamic shock and discontinuity structure. The current equation and divergence equation of magnetic field with artificial magnetic diffusivity can be written as

$$\frac{\partial \boldsymbol{j}}{\partial t} = RHS_{\rm phys} - \left[\nabla^2(\eta_{\rm art}\boldsymbol{j}) - \boldsymbol{\nabla}(\boldsymbol{\nabla}\eta_{\rm art}\cdot\boldsymbol{j})\right], \tag{2.39}$$

$$\frac{\partial(\boldsymbol{\nabla}\cdot\boldsymbol{B})}{\partial t} = 0. \tag{2.40}$$

The second and third terms of right-hand side of Equation (2.39) works as the diffusion effect of the current structure, hence this term is desired to be effective only at the vicinity of magneto-hydro dynamical shock for diffusing the steep structure. When the $\eta_{\rm art}$ is designed to be effective only at the vicinity of the MHD discontinuities, these terms becomes large because both the $\eta_{\rm art}$ and $\boldsymbol{j}$ are arose near the MHD discontinuities, and thus the steep structures of discontinuity are diffused. The Equation (2.40) obviously shows that the artificial magnetic diffusivity $\eta_{\rm art}$ does not derange the solenoidal condition of magnetic field in the partial differential equation level. Kawai (2013) probed that this relation can be preserved as long as the linear differential scheme is used for the calculation of the spatial derivation of induction equation. In addition to $\beta_{\rm art}$ and $\eta_{\rm art}$, the artificial mass diffusive flux $\boldsymbol{\mathcal{A}}_\rho$ is introduced for handling contact discontinuities. The first term of right-hand side of Equation (2.1) works as the diffusion effect of density structure, hence this term is desired to be effective only at the vicinity of discontinuity of density for diffusing steep structure. When the $\chi_{\rm art}$ is designed to be effective only at the vicinity of steep structure of density, this term becomes large only near the discontinuity of density, and thus the steep structure is diffused. Therefore, by introducing the artificial diffusivities into the governing equation at the vicinity of shocks and discontinuities as we defined in Equation (2.36) and combing the linear differential scheme such as the compact difference scheme, we can capture shocks and discontinuities without damping smooth structures of the vortices, the current, and the density and with satisfying the solenoidal condition.

The important point for introducing this type of numerical diffusivity is capturing shocks and discontinuities sharply, i.e., β_{art}, η_{art}, and χ_{art} is required to be arisen only at stuctures of discontinuities and shocks. The LAD method determines η_{art}, β_{art}, and χ_{art} by fourth-spatial derivation of the current density, divergence of velocity, and density respectively. η_{art}, β_{art} and χ_{art} are written as

$$\eta_{\mathrm{art}} = Rm_{\mathrm{norm}}\, C_\eta\, \overline{\frac{1}{\rho c_s}\left|\sum_{l=1}^{3}\frac{\partial^4|\boldsymbol{j}|^2}{\partial\xi_l^4}\Delta\xi_l^4\Delta_{l,\eta}^3\right|}, \tag{2.41}$$

$$\beta_{\mathrm{art}} = Re_{\mathrm{norm}}\, C_\beta\, \rho f_{sw}\, \overline{\left|\sum_{l=1}^{3}\frac{\partial^4(\nabla\cdot\boldsymbol{v})}{\partial\xi_l^4}\Delta\xi_l^4\Delta_{l,\beta}^2\right|}, \tag{2.42}$$

$$\chi_{\mathrm{art}} = C_\chi\, \overline{\frac{c_s}{\rho}\left|\sum_{l=1}^{3}\frac{\partial^4\rho}{\partial\xi_l^4}\Delta\xi_l^4\Delta_{l,\chi}\right|}, \tag{2.43}$$

where c_s is sound speed, and $\Delta_{l,\eta}$, $\Delta_{l,\beta}$, and $\Delta_{l,\chi}$ are amounts of projection of grid vectors $\boldsymbol{\Delta\xi_l}$ to the normal of magnetic discontinuities and density discontinuities and defined as

$$\Delta_{l,\eta} = \left|\boldsymbol{\Delta\xi}_l\cdot\frac{\boldsymbol{\nabla}p_m}{|\boldsymbol{\nabla}p_m|}\right|, \quad \Delta_{l,\beta} = \Delta_{l,\chi} = \left|\boldsymbol{\Delta\xi}_l\cdot\frac{\boldsymbol{\nabla}\rho}{|\boldsymbol{\nabla}\rho|}\right|, \tag{2.44}$$

where p_m is the magnetic pressure. The overline of Equation (2.41)(2.42)(2.43) denote the approximate trancated Gussian filter (see Cook & Cabot, 2004) calculated as

$$\begin{aligned}\overline{f}_i = \frac{3565}{10368}f_i + \frac{3091}{12960}(f_{i+1}+f_{i-1}) + \frac{1997}{25920}(f_{i+2}+f_{i-2}) \\ + \frac{149}{12960}(f_{i+3}+f_{i-3}) + \frac{107}{103680}(f_{i+4}+f_{i-4}).\end{aligned} \tag{2.45}$$

f_{sw} in equation (2.42) is a switching function defined as

$$f_{sw} = \frac{H(\nabla\cdot\boldsymbol{v})(\nabla\cdot\boldsymbol{v})^2}{(\nabla\cdot\boldsymbol{v})^2 + |\nabla\times\boldsymbol{u}| + \epsilon}, \tag{2.46}$$

where H is Heviside function and ϵ is a small positive constant.

C_η, C_β and C_χ are the user specified constants. The artificial diffusion values can be controlled by changing these constants, and thus, the strength of LAD method is adjustable to the arbitrary differential scheme, for example the compact difference scheme. To confirm whether the developed code captures the discontinuity properly

and clarify the effects of changing this constants, we carry out an 1-dimensional test simulations those are propagation of the contact discontinuity, the hydrodynamic shock, and the magnetic slow shock in accordance with Kawai (2013). Here, we show the result of the propagation test of slow-shock. The simulation domain is set as $[0., 1.]$ and we set 512 grid points in this range. The initial condition is set as

$$(\rho, v_x, v_y, v_z, p, B_x, B_y, B_z) = \begin{cases} (1.0, 2.0, 0, 0, 1.0, -1.0, 1.0, 0) & (x \leq 0.25) \\ (1.368, 1.731, 1.0, -1.0, 1.769, 1, 0, 0) & (x > 0), \end{cases}$$

with the specific heat $\gamma = 5/3$. The user specified constants are set as $C_\beta = 1.75$, and $C_\chi = 0.2$, and we vary the C_η and check the efficiency for capturing the shock. Figure 2.3 shows the structure of B_y near the slow-shock at $t = 0.2$. Red, green, blue, and magenta lines show the results with $C_\eta = 0, 1, 10,$ and 100 respectively. It is obviously shown that the more C_η is increased, a wiggle amplitude of numerical oscillation becomes smaller and the shock structure becomes more diffusive and thicker. This trade-off relationship represents the efficiency for the shock capturing of LAD method. We should adjust the user specified constants by using results of these test simulations to the suitable values which suppress numerical oscillation enough and does not diffuse structure beyond the necessity.

Kawai (2013) suggests the set of user specified constants as $C_\eta = 10$, $C_\beta = 1.75$, and $C_\chi = 0.2$ with the 6-th order compact difference schem. We carried out the test simulations of the propagation of the contact discontinuity, hydrodynamic shock, and magnetic slow-shock, and found that this set of user specified constants also can be suitable for our code even though we choose the 8-th order compact difference scheme. Therefore, the simulation in this study is basically carried out by using this set of user coefficients.

2.5 Pipeline algorithm

As described in Section 1.3, the parasitic instability has the wavenumber vector which direction corresponds to the disturbed velocity field or disturbed magnetic field. Therefore, the parasitic instability grows non-axisymmetrically. This fact demands to carry out 3-dimensional simulation to reveal the transition process from MRI to the turbulence. To carry out the 3-dimensional simulation, MHD simulation code is strongly required to be parallelized by using the domain decom-

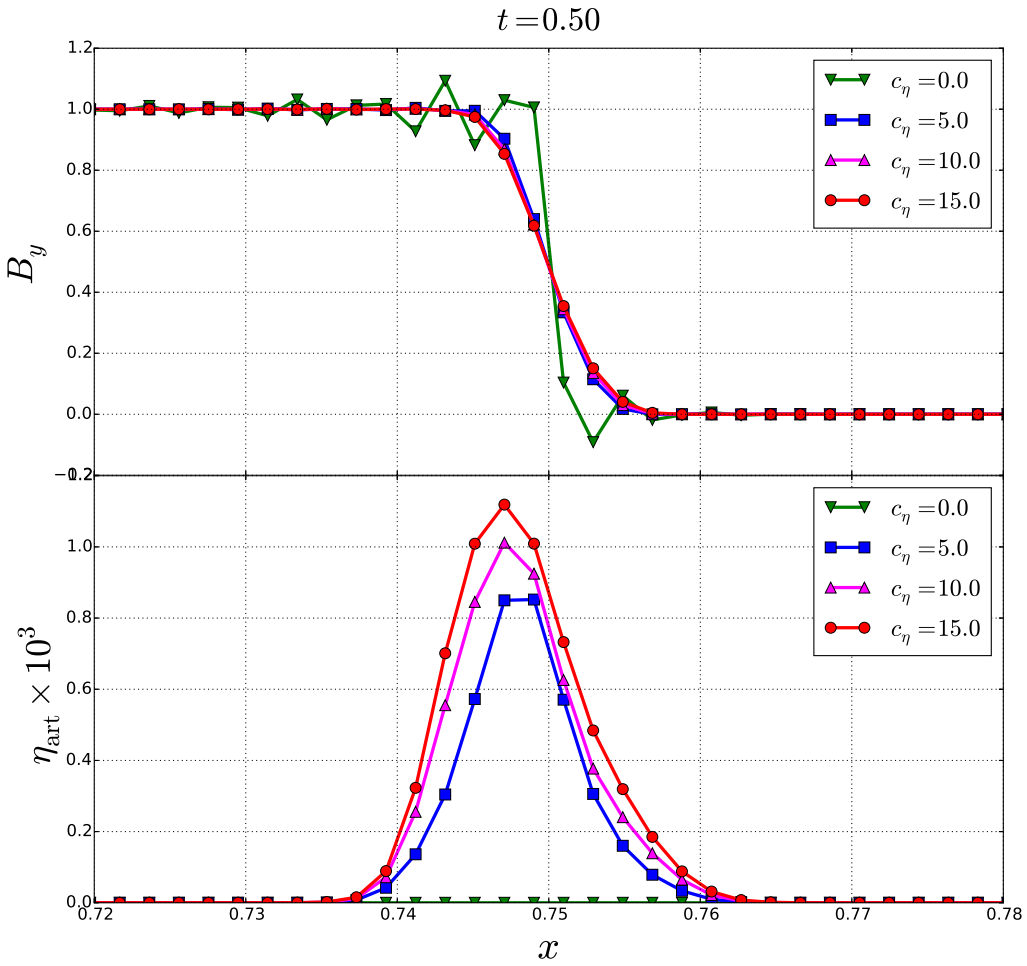

Fig. 2.3: The structures of B_y (top panel) and $\eta_{\rm art}$ (bottom panel) near the slow-shock at $t = 0.5$ of propagation test of slow-shock. Green, blue, magenta, and red lines show the results with $C_\eta = 0, 5, 10,$ and 15 respectively.

position. The domain decomposition is a method of dividing a simulation domain and parallelly calculating each domain in each process. To realize the parallelization by using domain decomposition, the data of grid points in marginal region of each calculation domain need to be exchanged with process of neighbour region by using Message Passing Interface (MPI). In addition to this, the compact difference scheme requires to exchange the data in the middle of the forward substitution and the backward substitution described in Section 2.3 because those substitution require the sequential calculations. Figure 2.4 shows the schematic image of the forward substitution in 2-dimensional simulation space with domain decomposition in x-direction. Horizontal axis is x-direction to which we divide the simulation domain by the number of processes $N_{\rm proc}$, and vertical axis is y-direction to which we

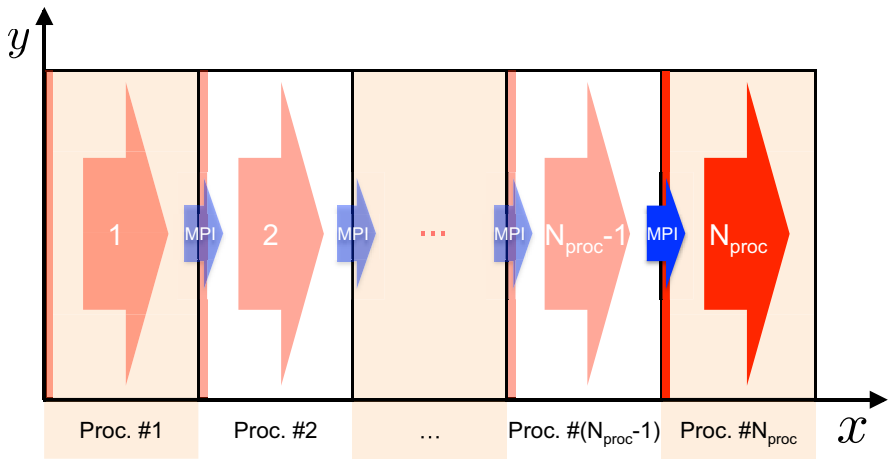

Fig. 2.4: A schematic image of the forward substitution in 2-dimensional simulation space with domain decomposition in x-direction without using pipeline algorithm.

assume the domain decomposition is not applied. If we doesn't use any technique, the forward substitution starts from the leftmost side of process number 1, and the halfway calculated data is passed to neighbour process after completing halfway calculation in the y direction, and continue this process toward the right end of process number N_{proc}. It is obvious that when the calculation is proceeding in a process, the other processes have to wait without calculation. Therefore reduction of the calculation time by parallelization cannot be realised in this case. To solve this problem, the developed code employs pipeline algorithm (Matsuura & Kato, 2007). Figure 2.5 shows schematic image of calculation of forward substitution of compact difference scheme by using the pipeline algorithm. We divide the simulation domain of each process into N_{block} blocks in y direction. Note that this division is not the thread or process parallelization but merely divides one process into N_{block} regions. First, the halfway calculation in x-direction proceeds for one block in y-direction. After the one-block calculation, the calculation resulted up there is passed to neighbour process in front. Finally, calculation can proceed in first and next process simultaneously. By repeating this process, the calculation can be completely parallelized as shown in Figure 2.5. The more we increase N_{Block}, the vain waiting time is decrease and the efficiency of parallelization itself becomes better. However, this algorithm also increases the amount of MPI-communications whose start-up and shut-down waste the time by increasing N_{block}. Therefore, the balance of N_{proc} and N_{block} is important for speed-up of the calculation, and this can be obtained by the way of numerical experiment. We

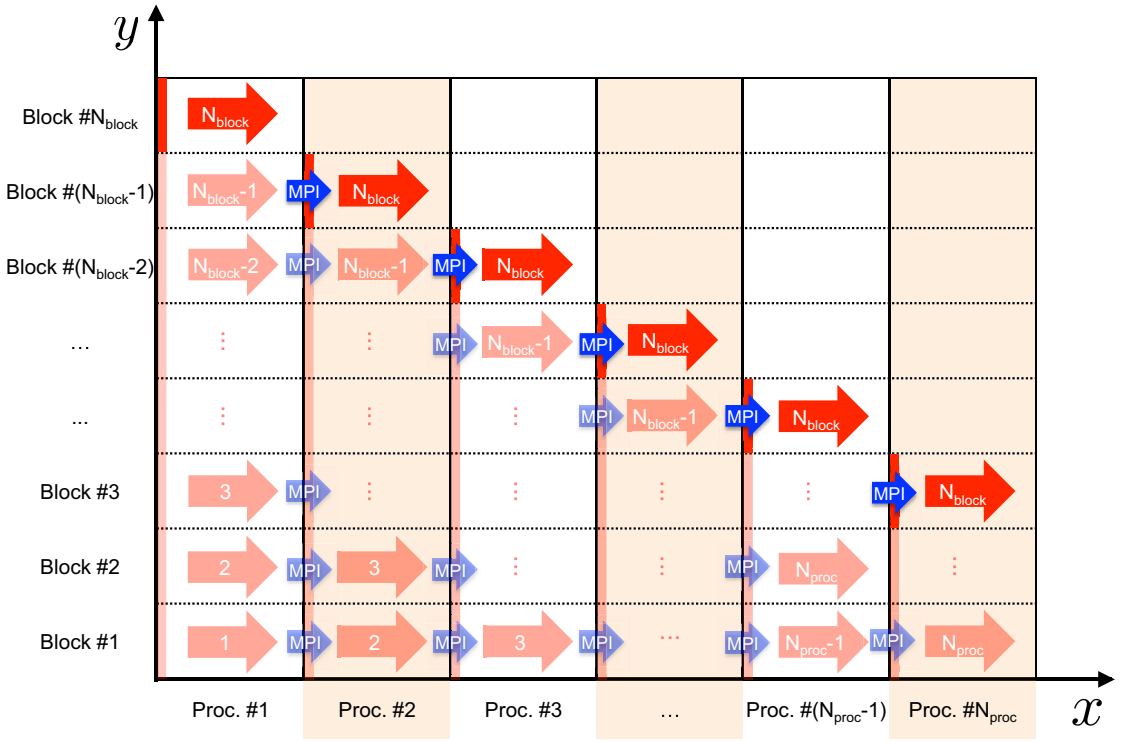

Fig. 2.5: A schematic image of the forward substitution in 2-dimensional simulation space with domain decomposition in x-direction with using pipeline algorithm.

carried out two-dimensional test simulation for finding the best relation of N_{proc} and N_{block}. We set the adequate sized two-dimensional simulation domain with meshes that are $N_x \times N_y = 512 \times 512$, where N and M denote the number of grid in x and y direction, respectively. All physical variables are uniformly set as unity and all boundaries are set as periodic; thus, all physical variables do not change with time. The simulation domain is divided in x-direction into 64 regions, i.e., the calculation is parallelized by $N_{\mathrm{proc}} = 64$. We divide the simulation domain of each process in y-direction into N_{block} blocks, and investigate the changes in calculation time for calculating 100 steps. Figure 2.6 shows variation of the calculation time by changing the N_{block}. Vertical axis represents calculation time T normalized by that of $N_{\mathrm{block}} = 1$, i.e., no-pipeline calculation, and horizontal axis represents N_{block} normalized by $N_{\mathrm{proc}} = 64$. In the case that $N_{\mathrm{block}} < 4N_{\mathrm{proc}}$, the calculation time becomes longer by decreasing N_{block} because the calculation is not sufficiently parallelized. And in the case that $N_{\mathrm{block}} > 4N_{\mathrm{proc}}$, the calculation time similarly becomes longer by increasing N_{block} because the communication time of MPI wastes much longer time. Since the calculation time takes the minimum value

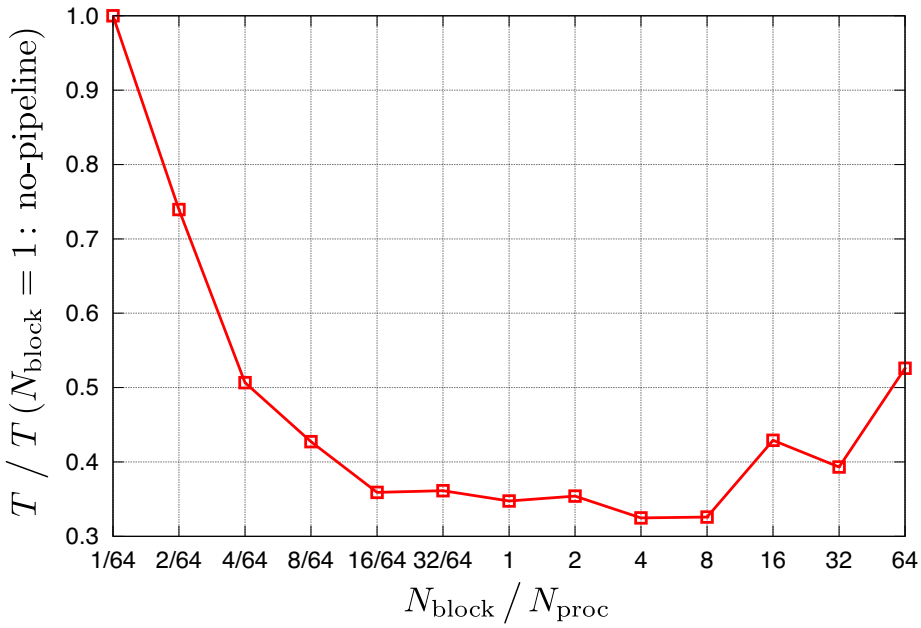

Fig. 2.6: Variation of the calculation time by changing the $N_{\rm block}$. Vertical axis represents calculation time T normalized by that of $N_{\rm block} = 1$, i.e., no-pipeline calculation, and horizontal axis represents $N_{\rm block}$ normalized by $N_{\rm proc} = 64$.

when the condition that $N_{\rm block} = 4N_{\rm proc}$, we employ this relation in our code. Note that $N_{\rm block}$ and $N_{\rm proc}$ can be converted to the number of blocks in two directions perpendicular to calculation and the number of processes in a direction parallel to calculation, respectively in the case of three-dimensional simulation; i.e., when we calculate forward and backward substitution in x-direction in the simulation box divided into $N_{{\rm proc},x} \times N_{{\rm proc},y} \times N_{{\rm proc},z}$ processes, the simulation domain of each process need to be divided in y and z direction into $N_{{\rm block},y}$ and $N_{{\rm block},z}$ blocks with the relation that $N_{{\rm block},y} \times N_{{\rm block},z} = 4N_{{\rm proc},x}$.

Finally, we check the parallelization efficiency of developed code employing pipeline algorithm by the strong-scaling. We measure the calculation time of three-dimensional simulation for 100 steps under the setting for the simulation of MRI-driven turbulence described in following Section 3.3 with 256^3 meshes, and investigate the variation of calculation time by changing the number of total processes $N_{\rm proc}$. In this calculation, the simulation domain is divided only in x and z directions because of difficulty of parallelize in y-direction; thus, $N_{\rm proc} = N_{{\rm proc},x} \times N_{{\rm proc},z}$. Figure 2.7 shows variation of calculation time by changing the $N_{\rm proc}$. Vertical axis represents acceleration ratio to that of $N_{\rm proc} = 64$, i.e., $T(N_{\rm proc} = 64)/T$, where T is calculation time, and horizontal axis represents the

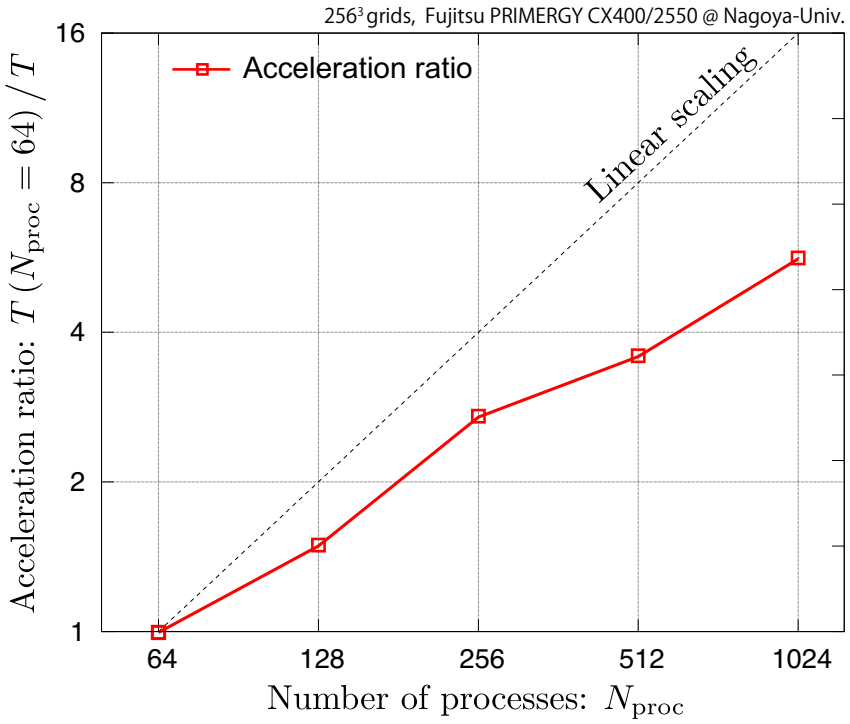

Fig. 2.7: Variation of calculation time by changing the $N_{\rm proc}$. Vertical axis represents acceleration ratio to that of $N_{\rm proc} = 64$, i.e., $T(N_{\rm proc} = 64)/T$, where T is calculation time, and horizontal axis represents the number of total processes $N_{\rm proc}$.

number of total processes $N_{\rm proc}$. The black dashed line denotes the linear-scaling, i.e., the result is on this dashed line if $1/T$ was perfectly proportional to $N_{\rm proc}$. Therefore, the closer the result is to the dashed line, the higher parallelization efficiency the code has. Figure 2.7 shows that our code has only about half parallelization efficiency compared to linear scaling. This is natural result because the simulation scheme which our code employs requires data exchange by MPI not only for the boundary condition but also for the calculation of derivatives. The important point is that the acceleration ratio is not damped but increase with augmenting $N_{\rm proc}$ in the range of the number of processes in this test. This fact indicates that increasing the number of processes effectively decrease the calculation time until at least 1024 processes. Therefore, the developed code is suitable for the carrying out large-scale three-dimensional MHD simulation.

2.6 Numerical tests

In this section, we show the some numerical and physical test problems to demonstrate the performance of developed code.

2.6.1 Propagation of Alfven wave

To confirm the efficiency for resolving wave of the developed code, we carry out the Alfven wave propagation test according to Tóth (2000). We set the two-dimensional simulation box of x and y direction and initial conditions are set as

$$\begin{aligned}
&\rho = 1.0,\ p = 0.1,\\
&v_x = -v_\perp \sin\theta,\ v_y = v_\perp \cos\theta,\ v_z = 0.1\cos(2\pi(x\cos\theta + y\sin\theta)),\\
&B_x = B_\parallel \cos\theta - B_\perp \sin\theta,\ B_y = B_\parallel \sin\theta + B_\perp \cos\theta,\ \text{and } B_z = v_z,
\end{aligned}$$

where

$$\begin{aligned}
&v_\perp = B_\perp = 0.1\sin(2\pi(x\cos\theta + y\sin\theta)),\\
&B_\parallel = 1.
\end{aligned}$$

This setting corresponds to the circular polarized Alfven wave in x and y surface propagating along the direction of θ from x-direction. We set $\theta = \pi/4$, i.e., the Alfven wave propagate 45° direction. Under this initial settings, the waveform becomes same at $t = 1, 2, 3, \cdots$ analytically. The simulation domain is set as $0 \le x < \sqrt{2}$ and $0 \le y < \sqrt{2}$, and all boundaries are set as the periodic boundary. The number of grids of each direction is set as $N_x \times N_y = 2N \times 2N$, and we vary the number of grid per 1 wavelength N from 4 to 16. Figure 2.8 shows the distribution of $B_\perp$ along the wave propagation direction from $(0, 0)$ to $(1/\sqrt{2}, 1/\sqrt{2})$ at $t = 5$. Black solid line represents the analytical solution, and red dashed line, green dash-dotted line, and blue dotted line show results with $N = 4, 8,$ and 10, respectively. This result indicates that our code can accurately resolve Alfven wave by more than 4 grid points per wavelength. The efficiency for resolving wave by 4 and 8 grid points per wavelength is especially high performance compared to other compressible MHD schemes (see figure (8) in Tóth, 2000). This fact indicates that developed code has ability to accurately resolve turbulent flow even with a small

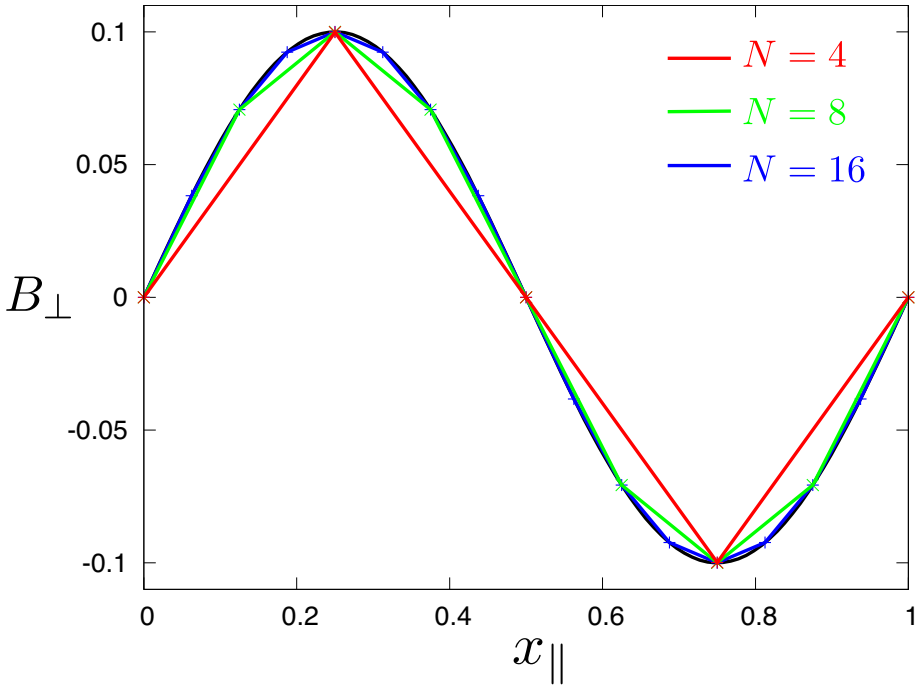

Fig. 2.8: The distribution of $B_\perp$ along the wave propagation direction from $(0, 0)$ to $(1/\sqrt{2}, 1/\sqrt{2})$ at $t = 5$.

number of grid.

2.6.2 Brio-Wu shock-tube problem

Next, we confirm the efficiency for capturing shocks and discontinuities by carrying out Brio-Wu shock-tube problem according to Brio & Wu (1988) and Ryu & Jones (1995). We set the one-dimensional simulation space in x-direction with the range that is $-1 \leq x < 1$, and initial conditions are set as

$$(\rho, v_x, v_y, v_z, p, B_x, B_y, B_z) = \begin{cases} (1.0, 0, 0, 0, 1.0, 0.75, 1.0, 0) & (-0.5 \leq x < 0.5) \\ (0.125, 0, 0, 0, 0.1, 0.75, -1.0, 0) & (-1 \leq x - 0.5,\ 0.5 \leq x < 1). \end{cases}$$

The boundaries are set as periodic boundary condition. The top, middle, and bottom panels of Figure 2.9 show the distribution of the density ρ, parallel velocity v_x, and perpendicular magnetic field B_y as red lines with left vertical axis, respectively, and also show the artificial mass diffusivity $\chi_{\rm art}$, artificial bulk viscosity $\beta_{\rm art}$, and artificial magnetic diffusivity $\eta_{\rm art}$ as blue lines with right vertical axis, respectively at $t = 0.12$. The gray dashed line shows the initial conditions. Although there are

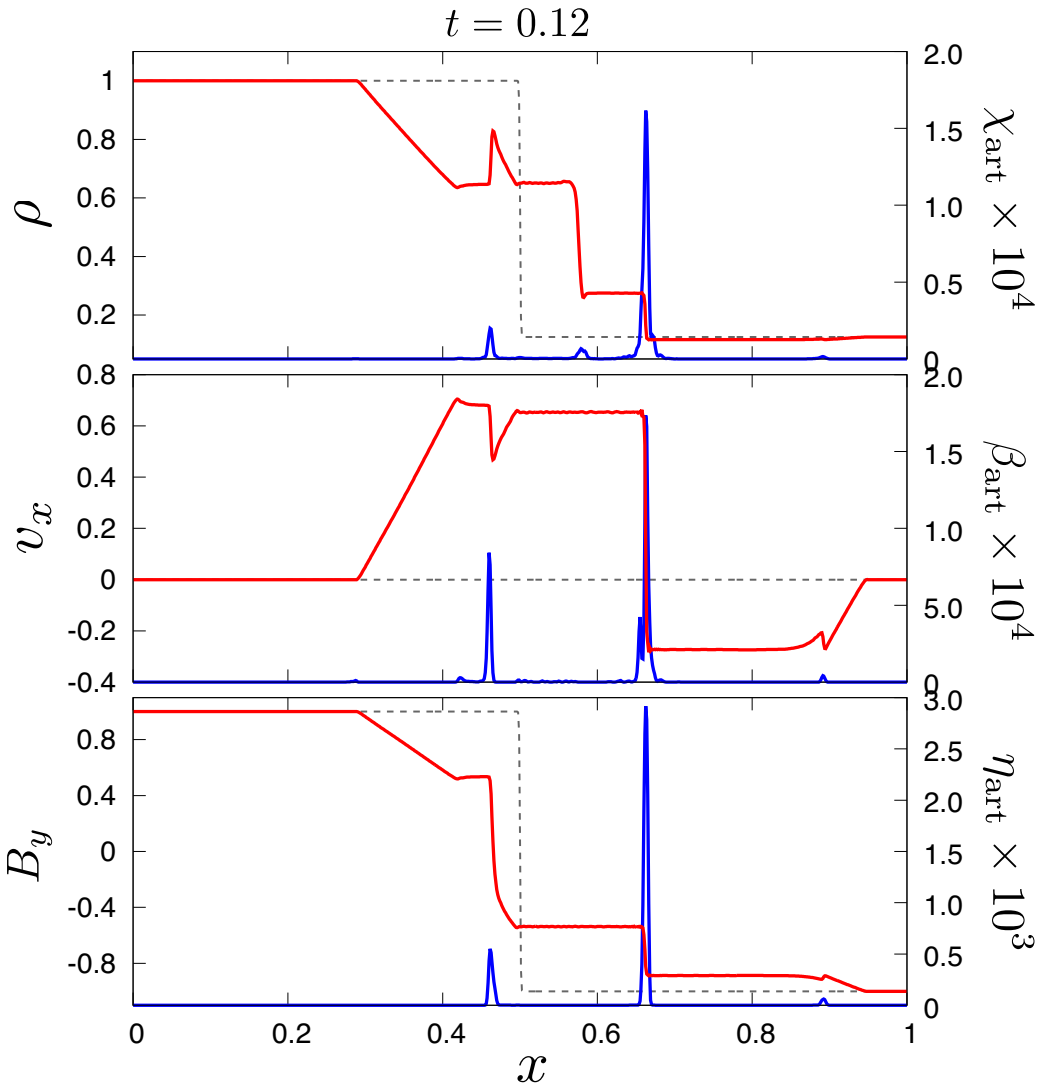

Fig. 2.9: The top, middle, and bottom panels show the distribution of the density ρ, parallel velocity v_x, and perpendicular magnetic field B_y as red lines with left vertical axis, respectively, and also show the artificial mass diffusivity $\chi_{\rm art}$, artificial bulk viscosity $\beta_{\rm art}$, and artificial magnetic diffusivity $\eta_{\rm art}$ as blue lines with right vertical axis, respectively at $t = 0.12$.

undershoots and overshoots with slight amplitude, the structures of discontinuity and shock are well captured by slightly diffusing steep structures by the artificial diffusivities calculated by the LAD method. From the test results of Figure 2.8 and Figure 2.9, developed code can resolve waves precisely as well as capturing discontinuities and shocks.

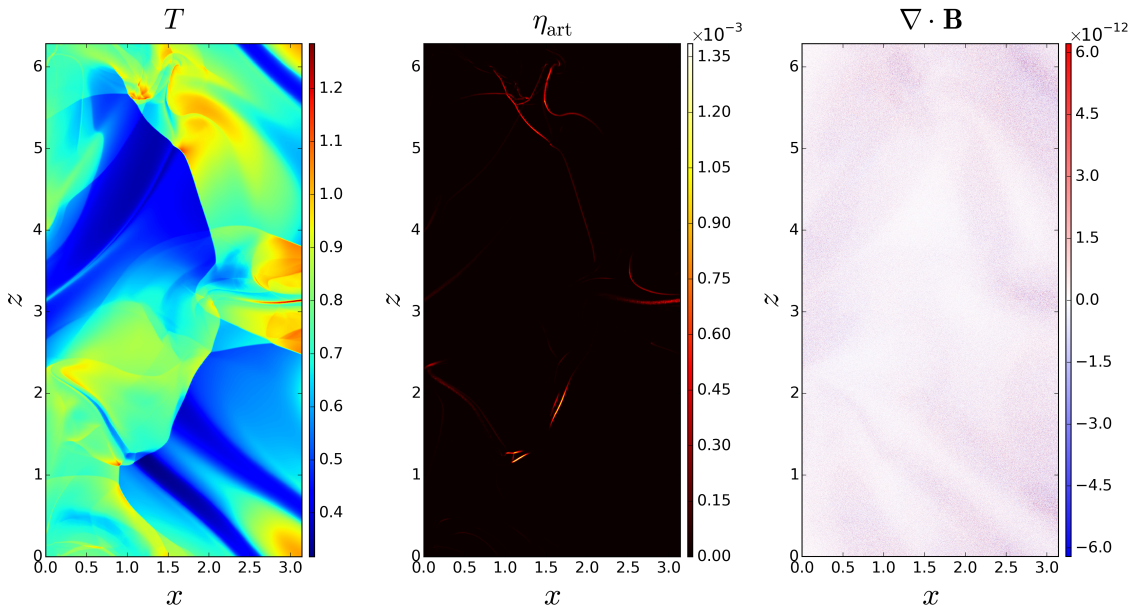

Fig. 2.10: Simulation results of Orszag-tang vortex problem. Left, middle, and right panel shows the temperature T, artificial magnetic diffusivity η_{art}, and divergence of magnetic field $\nabla \cdot \boldsymbol{B}$, respectively at $t = 3.1$.

2.6.3 Orszag-tang vortex problem

The final numerical test is the Orszag-Tang vortex problem that is a standard two-dimensional numerical test problem for MHD simulation. The initial condition of this problem leads smooth flow at first, and gradually develops the MHD turbulence and the MHD shock, and finally both of them complexly interact. Therefore, this problem is used as a touchstone-problem for measuring the efficiency of resolving turbulence and capturing discontinuity simultaneously. The initial conditions are set as $\rho = 2.778$, $v_x = -\sin y$, $v_y = \sin x$, $v_z = 0$, $p = 5/3$, $B_x = \sin y$, $B_y = \sin 2x$, $B_z = 0$ with $\gamma = 5/3$. The computational domain is $0 \leq x, y < 2\pi$ with the $N = 1024$ grid points for each direction ($N \times N$), and the boundaries are the periodic boundary. Left, middle, and right panel of Figure 2.10 shows the temperature T, artificial magnetic diffusivity η_{art}, and divergence of magnetic field $\nabla \cdot \boldsymbol{B}$, respectively at $t = 3.1$. According to the temperature distribution, the temperature profile that is uniform in the initial condition develops to the shock and the turbulence structure. As shown in middle panel of Figure 2.10, the artificial diffusivity is applied only at the vicinity of these shock structures and not effective at smooth structures. Meanwhile, as shown in the right panel of Figure 2.10, the

solenoidal condition of magnetic field is not broken and $\nabla \cdot \boldsymbol{B}$ is suppressed in the range of machine error. This feature is the efficiency of using compact difference scheme and LAD method. The developed code can preserve solenoidal condition of magnetic field as long as we use the periodic boundary condition. Note that this feature can not be maintained in the case of using the boundary condition that breaks the solenoidal condition of magnetic field, e.g., shearing box boundary condition. This is because the scheme satisfies the relation of $\partial(\nabla \cdot \boldsymbol{B})/\partial t = 0$, but not ensures $\nabla \cdot \boldsymbol{B} = 0$. Therefore, we have to employ the additional method for dealing with the $\nabla \cdot \boldsymbol{B}$ error arose at the shearing box boundary condition to apply the code for the calculation of MRI-driven turbulence.

2.7 Concluding remarks

In this chapter, we described the newly developed parallelized three-dimensional high-order MHD simulation code. Since we focused on resolving MRI-driven magnetic turbulence accurately, we developed the MHD simulation code by employing the MHD scheme proposed by Kawai (2013). This scheme is based on the high-order compact difference scheme (Lele, 1992) and high-order compact-type filtering scheme (Lele, 1992; Gaitonde & Visbal, 2000), and localized artificial diffusivity (LAD) method. Since the compact difference and compact-type filtering schemes required to do sequential calculation and thus they can not be simply parallelized by domain decomposition using MPI, we also employed the pipeline algorithm to parallelize without diminishing the accuracy. Developed code is successfully parallelized by using this algorithm and the acceleration ratio is increased by increasing the number of processes. We carried out some numerical tests and confirmed that developed code has following efficiency; high wavenumber accuracy, i.e., the code can solve the wave propagation with a few grids per wavelength, capturing discontinuities accurately, i.e., the calculation is not broken by numerical noise, and conserves the solenoidal condition, i.e., $\boldsymbol{\nabla} \cdot \boldsymbol{B} \sim 0$ as long as we use the periodic boundary condition. From these numerical tests, we could confirm that developed code works properly and has the efficiency for resolving MRI-driven turbulence.

Chapter 3

MHD simulation of MRI-driven turbulence in ideal MHD condition

3.1 Introduction to MRI-driven turbulence in ideal MHD condition

As introduced in Section 1.2, MRI is one of the most important phenomena in accretion disks and believed to make accretion disks turbulent state. In the fully ionized and Keplerian accretion disk, the maximum growth rate of MRI reaches $0.75\Omega_{\rm K}$ ($\Omega_{\rm K}$:Keplerian angular velocity), and thus the growth timescale of MRI is generally much shorter than the timescale of disk evolution. Several numerical simulations suggest that MRI results in the turbulent state of the accretion disk in the nonlinear evolutional stage (e.g., Hawley et al., 1995; Sano & Inutsuka, 2001; Sai et al., 2013). The existence of MRI-driven turbulence is supported by the observational studies that reported the higher accretion rate than that estimated by molecular viscosity. As shown in Section 1.1, the turbulent stress, increased by MRI and maintained in MRI-driven turbulence, acts as turbulent viscosity that causes mass accretion toward the central star (Shakura & Sunyaev, 1973). Therefore, MRI-driven turbulence is believed to be an appropriate explanation for the observed high mass accretion rate.

As mentioned in Section 1.3, Goodman & Xu (1994) analytically suggested that the linear growth of MRI is saturated and that the transition to the turbulent state is caused by subsequent instability called parasitic instability. Parasitic instability is incidental instability to MRI; it is related to the Kelvin-Helmholtz (K-H)

instability and the magnetic reconnection caused by both shear flow and antiparallel magnetic field resulting from the growth of MRI. The properties of parasitic instability, including the maximum growth wavenumber, growth rate, and wave direction, are controlled by the magnetic diffusivity and the fluid viscosity (Pessah, 2010). This is because those diffusivity terms change the eigenvector of MRI (Pessah & Chan, 2008), and also the magnetic diffusivity controls which of the modes, the K-H instability mode or the magnetic reconnection mode, grows faster. In the case of ideal MHD, the K-H instability mode is a dominant factor of parasitic instability, and thus the shear flow created by the linear growth of MRI plays an important role for saturating the MRI growth and resulting in turbulent state of the accretion disk.

Previous numerical studies reported on the wave spectrum of the enhancement of parasitic instability in an ideal MHD. Lesur & Longaretti (2011) and Murphy & Pessah (2015) carried out an incompressible MHD simulation in a local shearing box (Hawley et al., 1995) using a spectral method capable of high-resolution turbulence computations. These studies show that the structure of MRI-driven turbulence in the wavenumber space has anisotropy that is considered to be due to parasitic instability.

Rembiasz et al. (2016) carried out a compressible MHD simulation using the shock capturing and high-order reconstruction scheme and showed property of the termination of linear growth of MRI via parasitic instability. While they focused on core-collapse supernovae and did not assume the Keplarian disk parameter, they reported that the anisotropic wave enhancement via parasitic instability whose wavenumber is higher than analytical value. This fact suggests the possibility that the enhancement of waves whose spatial scale is smaller than the theoretical expectation plays an important role for the termination of MRI. In addition, numerical studies reported that the nonlinear evolution of MRI-driven turbulence changes when the resolution (e.g., Fromang & Papaloizou, 2007; Rembiasz et al., 2016) and numerical and small physical diffusivities (e.g., Fromang et al., 2007; Minoshima et al., 2015) are modified. Since these modifications change the small-scale flow structure, these studies indicate the importance of the small-scale waves for the generation of MRI-driven turbulence. It is, however, still unclear that how the small-scale structures and waves affect to mechanisms of termination of MRI and driving of magnetic turbulence. One of the reasons is that there are difficulties for the compressible MHD simulation to resolve small-scale structures and waves. Resolving small-scale and compressible flow requires an MHD simulation scheme

that resolves wave fine structures with capturing discontinuities. An MHD simulation code which can accurately resolve small-scale waves in compressible plasma is required to reveal the saturation process of MRI and the driving mechanism of magnetic turbulence.

In this study, we carry out MHD simulation in a local shearing box with the newly developed MHD code using the high-order and compressible scheme proposed by Kawai (2013). This scheme has the high wavenumber accuracy, which is suitable for investigating MRI-driven turbulence. By using this code, we investigate the enhancement of parasitic instability and how the enhanced small-scale structures and waves affect to the mechanisms of termination of MRI and driving of magnetic turbulence, i.e., the creation process of turbulent stress, in both the linear and nonlinear phase. This chapter is organized as follows. In Section 3.3, we describe governing equations, simulation models, numerical method, and simulation setup. In Section 3.4, we present simulation results and discussion. We show the enhancement of K-H mode parasitic instability and discuss its role for saturation and relaxation of turbulent stress at the first peak in Section 3.4.2, and we discuss difference between a nonlinear peak and the first peak in Section 3.4.3. We summarize this chapter in Section 3.5.

3.2 Linear analysis of MRI in ideal MHD condition

In this section, we revisit the property of MRI in the ideal MHD condition that was firstly shown by Balbus & Hawley (1991). To simplify the discussion, we employ the assumptions that (1) the plasma is homogeneous and incompressible, i.e. $\boldsymbol{\nabla}\cdot\boldsymbol{v}=0$, (2) the coordinate center is rotating around the central star with revolution angular velocity Ω, (3) the coordinate center is far enough away from the central star. Under these assumptions, the ideal MHD equations can be written in Cartesian coordinate with the centrifugal force and Coriolis force, and the continuous equation and energy equation are vanished. We set the radial, azimuthal, and vertical coordinates from the center of such a rotating coordinate system as x, y, and z coordinates, respectively. The momentum equation and induction equation are written as

$$\frac{\partial(\rho\boldsymbol{v})}{\partial t}+\boldsymbol{\nabla}\cdot\left[\rho\boldsymbol{v}\boldsymbol{v}-\frac{\boldsymbol{B}\boldsymbol{B}}{4\pi}+\left(p+\frac{B^2}{8\pi}\right)\boldsymbol{I}\right]=2q\Omega^2\rho x\hat{\boldsymbol{e}}_x-2\rho\boldsymbol{\Omega}\times\boldsymbol{v}, \tag{3.1}$$

$$\frac{\partial\boldsymbol{B}}{\partial t}+\boldsymbol{\nabla}\cdot[\boldsymbol{v}\boldsymbol{B}-\boldsymbol{B}\boldsymbol{v}]=\boldsymbol{0}, \tag{3.2}$$

where ρ, p, $\boldsymbol{v}$ and $\boldsymbol{B}$ denote density, gas pressure, velocity, and magnetic field, respectively, and q is the rotational parameter denoted as $\Omega \propto r^{-q}$ where r is distance from central star. We consider one of the simplest equilibrium condition of Equations (3.1) and (3.2) that are

$$\boldsymbol{v}_0 = -q\Omega x \hat{\boldsymbol{e}}_y, \quad \boldsymbol{B}_0 = B_0 \hat{\boldsymbol{e}}_z. \tag{3.3}$$

To obtain the dispersion relation of MRI, we linearise these equations by adding Fourier modes perturbation to velocity and magnetic field. We assume that the wavenumber vector of Fourier modes only have the z-direction component to simplify the calculation, i.e.,

$$f_1 = \delta f \exp i(k_z z - i\omega t), \tag{3.4}$$

where f is each physical quantity, k_z is the vertical wavenumber, t denotes the time, and ω is the complex angular frequency whose imaginary part represents the growth rate. Note that v_{z1} and B_{z1} become zero because of the solenoidal conditions of velocity and magnetic field that are $\nabla \cdot \boldsymbol{v} = \nabla \cdot \boldsymbol{B} = 0$. By employing above conditions and assumptions, Equations (3.1) and (3.2) can be linearised as following matrix equations.

$$\begin{pmatrix} 0 & 2i\Omega & -\frac{v_A^2 k_z}{B_0} & 0 \\ -i(2-q)\Omega & 0 & 0 & -\frac{v_A^2 k_z}{B_0} \\ -B_0 k_z & 0 & 0 & 0 \\ 0 & -B_0 k_z & iq\Omega & 0 \end{pmatrix} \begin{pmatrix} v_{1x} \\ v_{1y} \\ B_{1x} \\ B_{1y} \end{pmatrix} = \omega \begin{pmatrix} v_{1x} \\ v_{1y} \\ B_{1x} \\ B_{1y} \end{pmatrix}, \tag{3.5}$$

where v_A is the Alfven velocity defined as $v_A^2 = \frac{B_0^2}{4\pi\rho}$. Equation (3.5) shows that ω and $(v_{1x}, v_{1y}, B_{1x}, B_{1y})^{\mathrm{T}}$ correspond to the eigenvalue and eigenvector of the matrix in left hand side of Equation (3.5). The dispersion relation correspods to the eigenfunction of Equation (3.5), and can be written as

$$(\omega^2 - v_A^2 k_z^2)^2 - 2(2-q)\Omega^2\omega^2 - 2q\Omega^2 v_A^2 k_z^2 = 0. \tag{3.6}$$

Figure 3.1 shows the solution of this dispersion relation in the case of $q = 3/2$, i.e., the Keplerian disks. Horizontal axis of both panel (a) and (b) represents the normalized wavenumber defined as $v_A k_z/\Omega$, and vertical axis represents (a) real part and (b) imaginary part of normalized angular frequency defined as ω/Ω. The

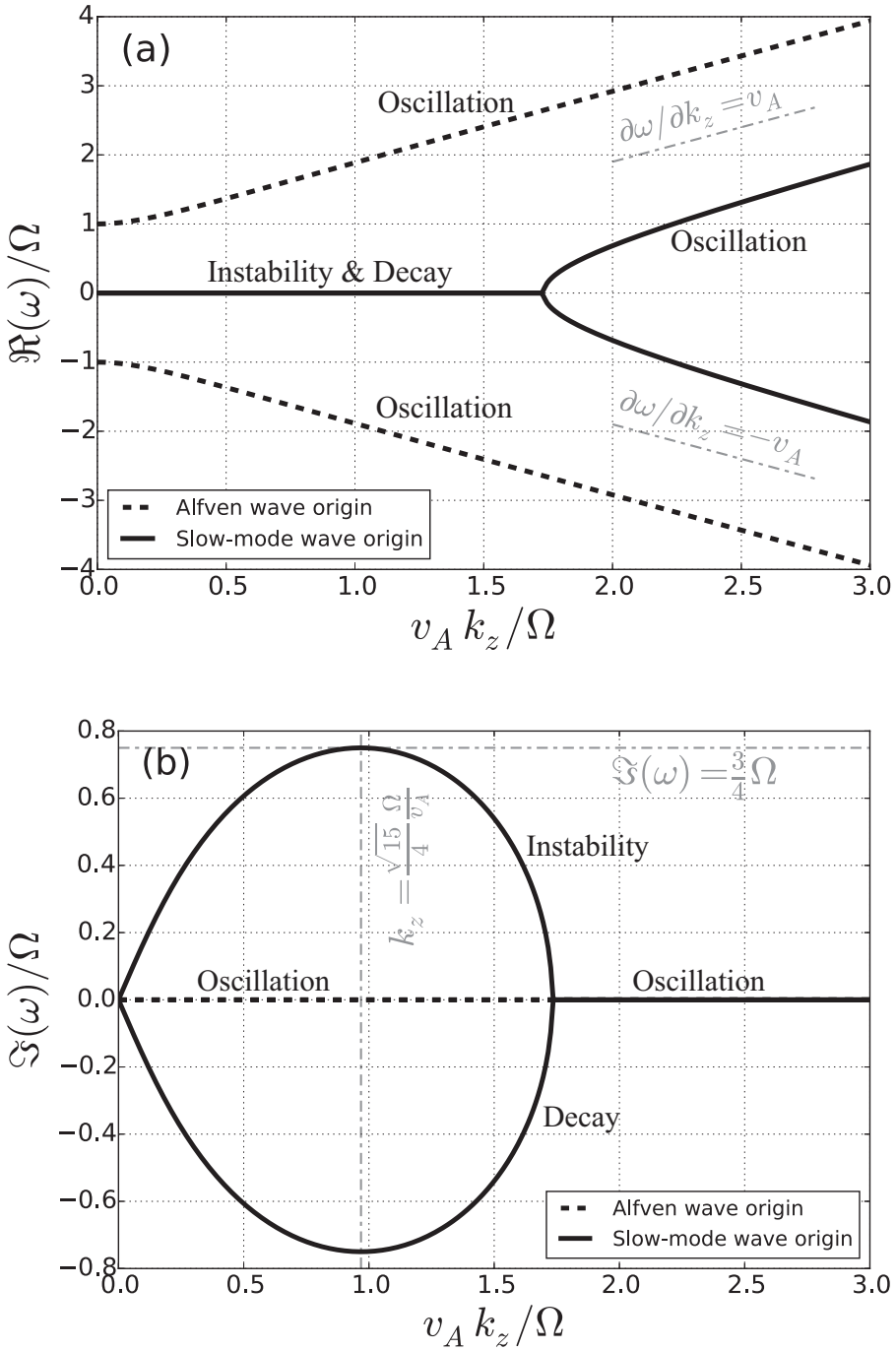

Fig. 3.1: The solution of dispersion relation of MRI in the ideal MHD condition, Equation (3.6). Solid line and dotted line in both panel (a) and (b) show the mode which has unstable solution and the other mode which has purely oscillation solution, respectively. Panel (a): Real part of angular frequency ω. Gray dash-dotted lines represent the group velocity of Alfven wave. Panel (b): imaginary part of angular frequency ω, i.e., the growth rate. Vertical and horizontal dash-dotted gray lines denote the wavenumber and growth rate of the maximum growth mode in ideal MHD condition.

panel (a) shows there are four branches; the two branches depicted by dotted lines that are purely oscillatory and whose phase velocity are higher than others, and the other two branches depicted by solid lines that have non-oscillatory and oscillatory ranges and whose phase velocity in oscillatory range is slower than purely oscillatory branches. The former are originated by Alfven wave and its cut-off corresponds to the epicyclic frequency that is $\kappa^2 = 2(2-q)\Omega^2$. The latter are originated by slow-mode wave and have the instability and decay wavenumber range. The panel (b) shows growth rate of such four branches. The purely oscillatory branches depicted by dotted line don't have finite value in all range, thus these oscillations do not grow or decay. The other two branches have non-zero values, i.e., the one branch is instability mode ($\Im(\omega) > 0$) and the other is decay mode ($\Im(\omega) < 0$). This instability mode is so called 'magneto-rotational instability (MRI)'. The important points of MRI are above two points. The first point is its high maximum growth rate. As shown in panel (b), MRI has the maximum growth wavenumber that is $k_{z,\mathrm{mas}} = (\sqrt{15}/4)(\Omega/v_A)$, and the maximum growth rate is $\Im(\omega)_{\max} = 0.75\Omega$ in Keplerian disks. This indicates that the perturbation amplifies to more than 100 times larger with an rotational time. Therefore, the timescale of MRI growth is much shorter than that of typical timescale of disk evolution that is $\sim 10^6$yr for protoplanetary disks for example, and thus, MRI is believed as the most dominant phenomenon for the evolutional process of accretion disks. The second point is that MRI is driven by weak magnetic field. As shown in panel (b), the MRI branch has the wavenumber range that is $k_z = [0, \sqrt{3}\Omega/v_A]$. v_A is proportional to the magnetic field, thus the range becomes wider when magnetic field decreases. Therefore, MRI can be driven with a weak magnetic field, or rather the wavenumber range that MRI can drive becomes narrowed in the case that the magnetic field is too strong.

In addition to these two points, there is one more important point for discussing the detailed mechanism of driving turbulence; that is the angles of perturbed velocity and magnetic field. We define the angles formed by perturbation components of velocity that are δv_x and δv_y, and magnetic field that are δB_x and δB_y as $\theta_v = \arctan(\delta v_y/\delta v_x)$ and $\theta_B = \arctan(\delta B_y/\delta B_x)$, respectively. The perturbation fields satisfy Equation (3.5), i.e., they are correspond to the eigenvector of the matrix equation. Figure 3.2 shows the angles of perturbed velocity θ_v (solid line) and magnetic field θ_B (dotted line) of the instability mode in the wavenumber range of MRI, i.e., $v_A k_z/\Omega = [0, \sqrt{3}]$. It is obvious that θ_v and θ_B strictly become $\pi/4$ and $-\pi/4$ from the radial direction at the maximum growth wavenumber. Therefore, the perturbed velocity and magnetic field that have the maximum growth

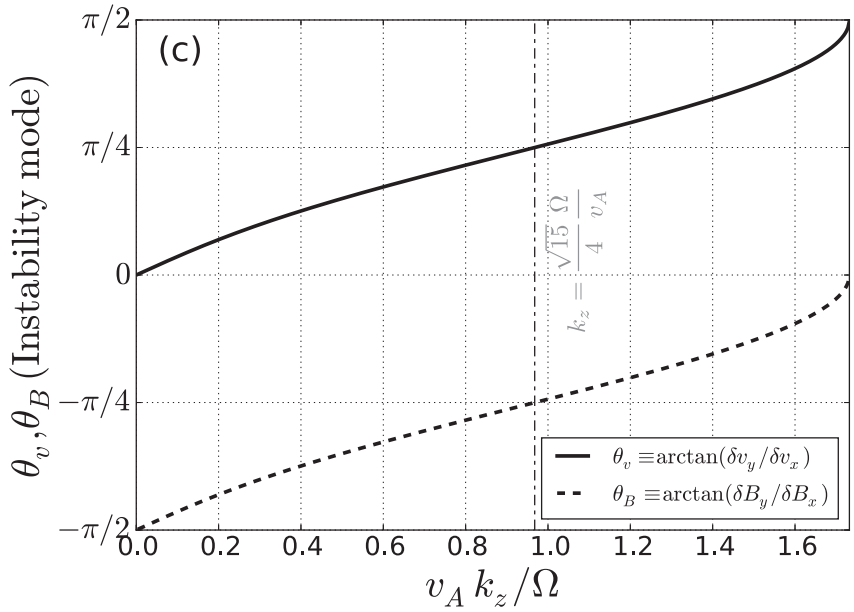

Fig. 3.2: The angles formed by perturbation components of velocity and magnetic field satisfying Equation (3.5), i.e., $\theta_v = \arctan(v_{1y}/v_{1x})$ (solid line) and $\theta_B = \arctan(B_{1y}/B_{1x})$ (dotted line), respectively. Vertical gray dash-dotted line represents the maximum growth wavenumber of MRI in ideal MHD condition.

wavenumber grow exponentially in these specific directions. These specific directions of the perturbed velocity and magnetic field play important roles for determining the enhancement of K-H mode parasitic instability in Section 3.4.2 and Section 3.4.3.

3.3 Simulation setup

3.3.1 Governing equations

We carry out the adiabatic, compressible, and ideal MHD simulation with the simulation box locally located on the disk and corotating with Keplerian angular velocity around the central star. The governing equations are normalized ideal

MHD equations written in conservative form as follows.

$$\frac{\partial \rho}{\partial t} + \boldsymbol{\nabla} \cdot (\rho \boldsymbol{v}) = 0, \tag{3.7}$$

$$\frac{\partial (\rho \boldsymbol{v})}{\partial t} + \boldsymbol{\nabla} \cdot \left[\rho \boldsymbol{v}\boldsymbol{v} - \mathcal{M}_{\mathrm{norm}}^2 \boldsymbol{B}\boldsymbol{B} + \left(p + \mathcal{M}_{\mathrm{norm}}^2 \frac{B^2}{2} \right) \boldsymbol{I} \right] = \boldsymbol{S}_{\mathrm{Momentum}}, \tag{3.8}$$

$$\frac{\partial \boldsymbol{B}}{\partial t} + \boldsymbol{\nabla} \cdot (\boldsymbol{v}\boldsymbol{B} - \boldsymbol{B}\boldsymbol{v}) = \boldsymbol{0}, \tag{3.9}$$

$$\frac{\partial E}{\partial t} + \boldsymbol{\nabla} \cdot \left[\left(E + p + \mathcal{M}_{\mathrm{norm}}^2 \frac{B^2}{2} \right) \boldsymbol{v} - \mathcal{M}_{\mathrm{norm}}^2 (\boldsymbol{v} \cdot \boldsymbol{B}) \boldsymbol{B} \right] = S_{\mathrm{Energy}}, \tag{3.10}$$

where ρ,p,$\boldsymbol{v}$, $\boldsymbol{B}$ denote the gas density, pressure, velocity field, and magnetic field, respectively, and $\mathcal{M}_{\mathrm{norm}}$ is Alfven Mach number defined as $\mathcal{M}_{\mathrm{norm}} = v_{A\,\mathrm{norm}}/c_{s\,\mathrm{norm}}$. E is the total energy defined as

$$E = \frac{p}{\gamma - 1} + \frac{\rho v^2}{2} + \mathcal{M}_{\mathrm{norm}}^2 \frac{B^2}{2}, \tag{3.11}$$

where γ is the specific heat set as $\gamma = 5/3$. Note that the actual simulation uses one more equation and source terms of induction equation that are obtained from the hyperbolic divergence cleaning method described later.

To calculate the local area of the accretion disk with a Cartesian grid, we set up a small simulation box whose center rotates with Keplerian angular velocity around the central star; this is so called the shearing box (Hawley et al., 1995). We set the radial, azimuthal, and vertical directions of the disk as x, y, z, respectively in a rotating coordinate system. By using a rotating coordinate system, the source terms are obtained from Equation (3.8) and Equation (3.10) as $\boldsymbol{S}_{\mathrm{Momentum}}$ and S_{Energy}, respectively. These terms originate from the centrifugal force and the Coriolis force, and they are defined as

$$\boldsymbol{S}_{\mathrm{Momentum}} = 2q\Omega^2 \rho x \hat{\boldsymbol{e}_x} - 2\rho \boldsymbol{\Omega} \times \boldsymbol{v}, \tag{3.12}$$

$$S_{\mathrm{Energy}} = 2q\Omega^2 \rho x v_x, \tag{3.13}$$

where Ω is the normalized angular velocity of the rotating simulation box, q is the rotational parameter of the disk defined as $\Omega \propto r^{-q}$, and x is the radial distance from the center of the simulation box where the rotating angular velocity corresponds to the Keplerian angular velocity.

All physical values in the above equations are normalized by the physical properties of an arbitrary disk model. The normalization constants in our simulation are

density $\rho_{\rm norm}$, sound speed $c_{s\,\rm norm}$, and time required for orbiting 1 radian T to an arbitrary distance from the central star for normalizing the density, velocity, and time, respectively. Under this normalization coefficient setting, the length, pressure, magnetic field, and angular velocity are normalized by $L = c_{s\,\rm norm}T = H/\sqrt{2}$, $p_{\rm norm} = \rho_{\rm norm}c^2_{s\,\rm norm}$, $B_{\rm norm} = \sqrt{4\pi\rho_{\rm norm}c^2_{s\,\rm norm}}$, and $\Omega_{\rm norm} = 1/T$, respectively, where H is the scale length of disk thickness. Under these normalization settings, $\mathcal{M}_{\rm norm} = 1$.

3.3.2 Shearing box approximation and its boundary condition

The developed code uses the shearing box boundary condition (Hawley et al., 1995) to apply the simulation box to the corotating coordinate system in differential rotational disks. The shearing box boundary condition requires the calculation of the physical value between the grids, and thus it is necessary to interpolate grid values in the ghost grids at the x-direction boundaries. Interpolation is performed by Taylor expansion at the nearest grid calculated by repeating compact differencing in the y-direction. This interpolation process breaks the solenoidal condition of the magnetic field only at the x-direction boundaries. To deal with this problem, the developed code also employs the hyperbolic divergence cleaning method (Dedner et al., 2002). By using this method, the divergence errors occurring at the shearing boundary are diffused by attenuation. The divergence error of the simulation in this study is suppressed in $|\nabla \cdot \boldsymbol{B}| < 0.5$.

3.3.3 Simulation settings

The computational domain is considered to be $(L_x, L_y, L_z) = (2\sqrt{2}, 2\sqrt{2}, \sqrt{2}) = (2H, 2H, H)$ where x, y, and z represent the radial, azimuthal, and vertical directions of the disk, respectively, and number of grid points in each direction is set as $N_x \times N_y \times N_z = 256 \times 256 \times 128$. The angular velocity of the rotating simulation box is set as $\Omega = 1.0$, and Initial gas density is set as $\rho_0 = 1.0$. We assume that the disk is a Keplerian disk; therefore the disk parameter is $q = 1.5$ and the initial gas velocity is set as $\boldsymbol{v}_0 = 1.5\Omega x\,\hat{\boldsymbol{e}}_y$, where $\hat{\boldsymbol{e}}_l$ denotes the unit vector of l-direction. The initial magnetic field is the net vertical magnetic field $\boldsymbol{B}_0 = B_0\,\hat{\boldsymbol{e}}_z$. In this simulation, we set the strength of the initial magnetic field such that the maximum growth wavelength of MRI corresponds to the third part of the vertical box length, i.e., $\lambda_{\rm MRI,max} = 8\pi v_A/\sqrt{15}\Omega = L_z/3$. The value of the magnetic field strength is therefore set as $B_0 \sim 7.26 \times 10^{-2}$ in this scenario. The initial plasma beta is set

as $\beta_{\rm plasma,0} = 400$, and thus the initial pressure is set as $p_0 = 2\beta_{\rm plasma,0}B_0^2 \sim 1.06$. A small random noise, whose amplitude corresponds to 0.5% of the sound speed, is initially added to all components of the velocity as seed for instability.

3.4 Simulation results and discussion

3.4.1 Time evolution of turbulent stress

We carried out calculation for 50 orbital period with the settings described in Section 3.3. Panel (a) of Figure 3.3 shows time evolution of some wave modes of the z-directional wavenumber spectra of a sum of the radial and the azimuthal velocity averaged over the radial and the azimuthal wavenuber space, i.e., $\left\langle v_h(k_z)^2 \right\rangle_{k_x,k_y} = \left\langle v_x^2(k_z) + v_y^2(k_z) \right\rangle_{k_x,k_y}$. The horizontal axis represents the orbital period $t_{\rm orbit}$. Red, yellow, green, blue, and purple lines represent the modes with the wavelength $\lambda_z = L_z, L_z/2, L_z/3, L_z, 4, L_z/5$, respectively, and the gray dash-dotted line represents analytically obtained maximum growth rate. Since the initial magnetic field is set to drive the MRI whose maximum growth wavelength corresponds to $L_z/3$, the mode $\lambda = L_z/3$ has the fastest growth rate that approximately corresponds to the analytically obtained fastest growth rate of MRI, i.e., 0.75Ω. The linear growth phase ends at around $t_{\rm orbit} = 2.8$, and the evolution enters a nonlinear phase. At nonlinear peak, the mode $\lambda = L_z$ becomes dominant because the magnetic field is amplified by MRI and the growth condition of MRI is changed. This feature is consistent with those described in previous studies such as Sano & Inutsuka (2001). Panel (b) of Figure 3.3 shows the time evolution of spatially averaged turbulent stress $\langle W_{xy} \rangle$ normalized by initial pressure p_0. Turbulent stress W_{xy} is defined as

$$W_{xy} \equiv W_{{\rm R}xy} + W_{{\rm M}xy} \equiv \rho \delta v_x \delta v_y - \delta B_x \delta B_y, \tag{3.14}$$

where $W_{{\rm R}xy} = \rho \delta v_x \delta v_y = \rho v_x (v_y - q\Omega x)$ is the Reynolds stress, and $W_{{\rm M}xy} = -\delta B_x \delta B_y = -B_x B_y$ is the Maxwell stress. Red, blue, and black lines in panel (b) of Figure 3.3 represent the Maxwell, Reynolds, and total stress, respectively. The total turbulent stress repeatedly increases and decreases every few orbital periods, and the Maxwell stress $W_{{\rm M}xy}$ is basically larger than the Reynolds stress $W_{{\rm R}xy} = \rho \delta v_x \delta v_y$. These features are similar to the previous three-dimensional simulation studies on MRI-driven turbulence (e.g., Hawley et al., 1995; Sano & Inutsuka, 2001). In this paper, we will focus on the first peak at around $t_{\rm orbit} = 2.8$ (left

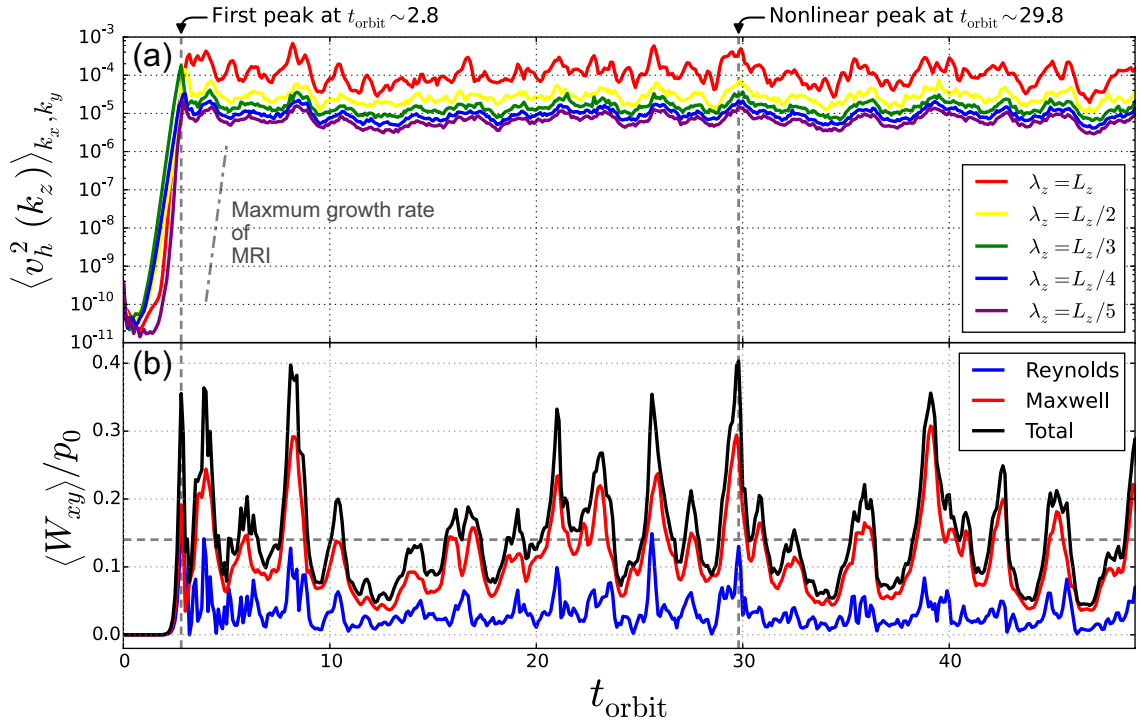

Fig. 3.3: (a) Time evolution of some wave modes of the z-directional wavenumber spectra of a sum of the radial and the azimuthal velocity averaged over the radial and the azimuthal wavenumber space. Red, yellow, green, blue, and purple lines represent the modes with wavelength $\lambda_z = L_z, L_z/2, L_z/3, L_z, 4, L_z/5$, respectively, and the gray dash-dotted line represents the analytically obtained maximum growth rate. (b) Time evolution of spatially averaged turbulent stress $\langle W_{xy}\rangle$ normalized by initial pressure p_0. Red, blue, and black lines represent the Maxwell, Reynolds, and total stress, respectively.

gray dashed line) and an arbitrarily chosen nonlinear peak at around $t_{\rm orbit} = 29.8$ (right gray dashed line) to reveal the saturation mechanism of turbulent stress in the linear and nonlinear phase, and the differences of these peaks.

3.4.2 Termination mechanism of linear growth of MRI at the first peak

Linear growth of MRI and its structure

The turbulent stress induced by MRI linearly first grows until a few orbital periods, then saturates at around $t_{\rm orbit} = 2.8$, and finally decreases after saturation. In order to see the cascade structure of the injection energy due to MRI, we check the wavenumber spectra of the horizontal velocity along the vertical direction around the first peak. Figure 3.4 shows the time evolution of the z-direction wavenumber

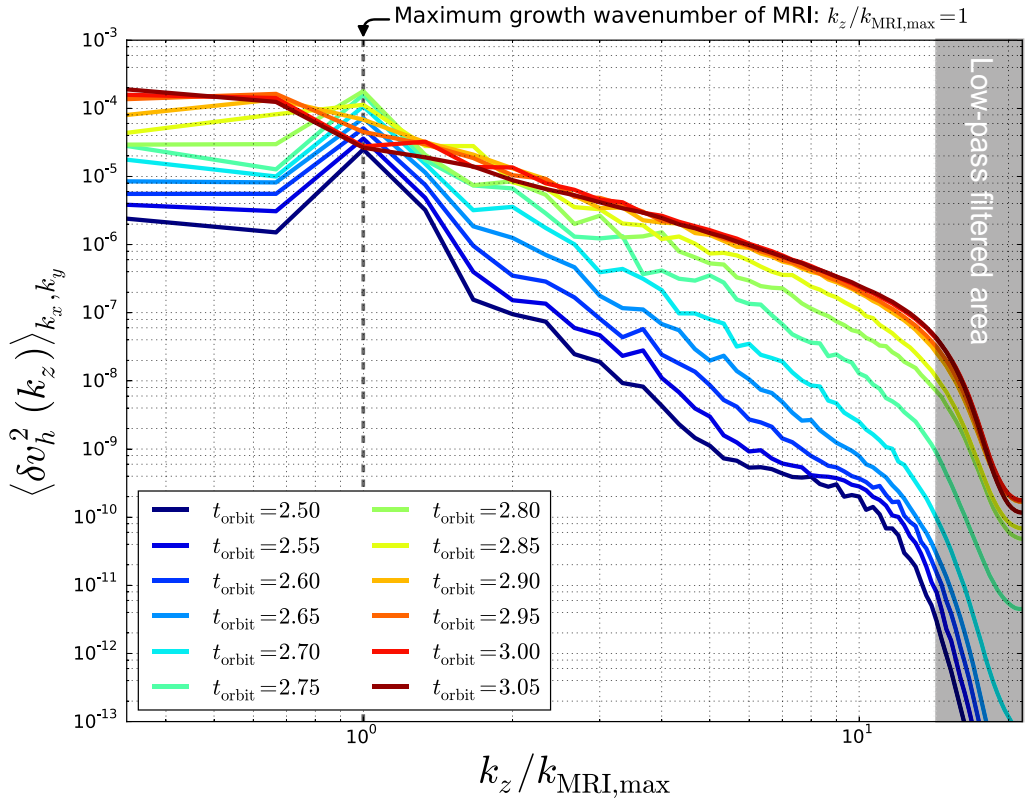

Fig. 3.4: Z-direction wavenumber spectra for the horizontal component of horizontally averaged disturbed fluid speed $\langle \delta v_h \rangle_{x,y}$ around the saturation. The colors of lines correspond to the time, and so the time elapsed is shown from cold color to warm color.

spectra for the horizontally averaged horizontal disturbed fluid speed $\left\langle {\delta v_h}^2 \right\rangle_{x,y}$ around saturation. δv_h is defined as

$$\delta v_h \equiv \sqrt{v_x^2 + (v_y - q\Omega x)^2}. \tag{3.15}$$

In the linear growth phase, MRI transforms the gravitational potential to horizontal velocity (and horizontal magnetic energy) with the initially set maximum growth wavenumber $k_z = 3 \times 2\pi/L_z = k_{\mathrm{MRI,\ max}}$. This growth is terminated at around $t_{\mathrm{orbit}} = 2.8$, and the injected energy is widely diffused in wavenumber space after that. Note that the high wavenumber area ($k_z L_z/2\pi \gtrsim 40$) is dumped due to the 10-th order compact-type low pass filtering. From this figure, it is expected that the injected energy cascades toward the high wavenumber structure due to the enhancement of parasitic instability at $t_{\mathrm{orbit}} = 2.8$.

In order to determine the phenomena that occurs at time of the first saturation,

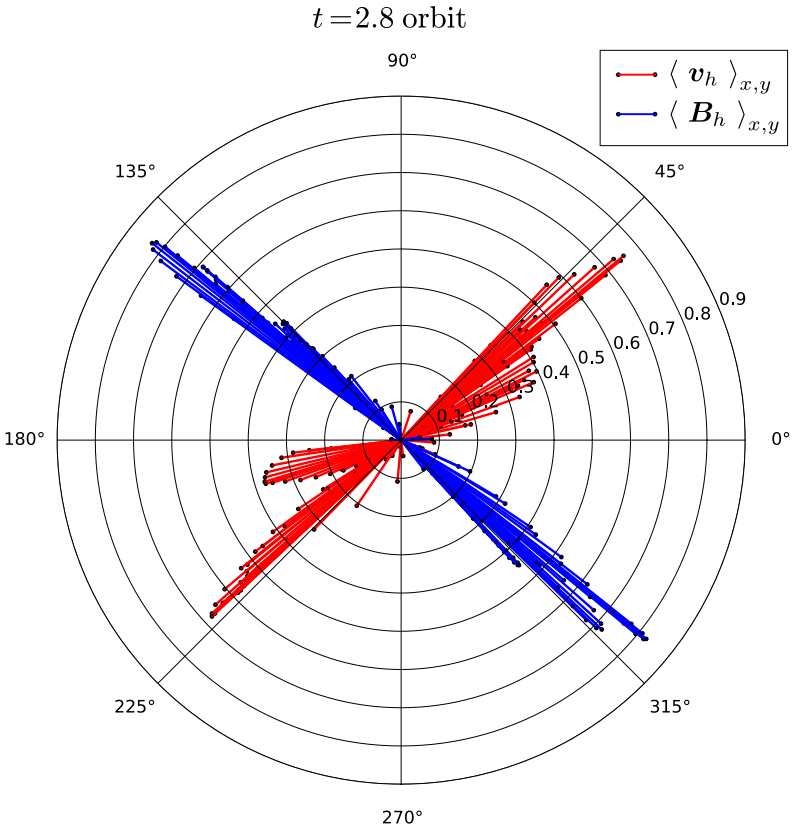

Fig. 3.5: The horizontally averaged horizontal disturbed velocity $\langle \delta \boldsymbol{v}_h \rangle_{x,y}$ (red lines) and disturbed magnetic field $\langle \delta \boldsymbol{B}_h \rangle_{x,y}$ (blue lines) at saturation timing $t_{\rm orbit} = 2.8$. Horizontal and vertical axis represent radial and azimuthal components respectively.

we check disturbed field structures of the horizontal velocity and the horizontal magnetic field. Figure 3.5 shows the horizontally averaged horizontal disturbed velocity $\langle \delta \boldsymbol{v}_h \rangle_{x,y}$ (red lines) and disturbed magnetic field $\langle \delta \boldsymbol{B}_h \rangle_{x,y}$ (blue lines) at the first peak. The disturbed horizontal field vectors $\delta \boldsymbol{v}_h$ and $\delta \boldsymbol{B}_h$ are defined as

$$\delta \boldsymbol{v_h} \equiv v_x \hat{\boldsymbol{e}}_x + (v_y - q\Omega x)\hat{\boldsymbol{e}}_y, \tag{3.16}$$

$$\delta \boldsymbol{B_h} \equiv B_x \hat{\boldsymbol{e}}_x + B_y \hat{\boldsymbol{e}}_y. \tag{3.17}$$

These vectors are plotted for each z grid, so that each horizontal vectors has 128 lines. Although there are slight variabilities, the fluctuation velocity and magnetic field have antiparallel vectors in specific directions, which are $\pi/4, 5\pi/4$ radian and $3\pi/4, 7\pi/4$ radian from the radial direction, respectively. These features show that the angle of eigenvectors of MRI in an ideal MHD obtained by the dispersion

relation (e.g., Goodman & Xu, 1994; Pessah & Chan, 2008), i.e., the relations of components,

$$\tan(\delta v_y/\delta v_x) = 1,\ \tan(\delta B_y/\delta B_x) = -1, \tag{3.18}$$

is conserved until just before the saturation of turbulent stress. In particular, this MRI-driven antiparallel velocity, i.e., shear flow velocity, is called MRI channel flow. The amplitude of these antiparallel fluctuation vectors becomes larger with time in the linear growth phase while maintaining the specific angles, and just after saturation, the amplitude growth stops and the angle of these vectors spreads widely. The temporally increasing shear velocity and antiparallel magnetic field can drive the K-H instability and the magnetic reconnection in the direction of the respective antiparallel vectors. Since this calculation is in an ideal MHD simulation, it can be expected that the K-H instability is dominantly induced and rolls up the flow toward the vertical direction.

Enhancement of parasitic instability and its contribution to the termination of MRI linear growth

To determine the enhancement of the wave induced by parasitic instability and its direction at the first peak, we apply two-dimensional Fourier transform to the vertical component of fluctuation velocity v_z and magnetic field B_z in the horizontal plane. The perturbation of the K-H instability and the magnetic reconnection induced by MRI dominantly create a vertical component of the velocity and magnetic field, respectively because the velocity and magnetic field that the MRI creates have the horizontal components. Therefore, we can confirm the enhancement of parasitic instability by comparing the direction of the horizontal two-dimensional wavenumber spectra of v_z and B_z with the vectors of the horizontal disturbed velocity $\boldsymbol{v}_h$ and $\boldsymbol{B}_h$. Fourier transform cannot be normally applied in the x-direction because the boundary of x-direction is not periodic but a shearing boundary. Therefore, we apply the Hamming window function along the x-direction before Fourier transform. Figure 3.6 shows two-dimensional wavenumber spectra of (a) δv_z and (b) δB_z in the horizontal wavenumber plane averaged over vertical wavenumber direction at $t_{\rm orbit} = 2.8$. The horizontal and vertical axes represent radial and azimuthal wavenumber, respectively, and these values are normalized by the maximum growth wavenumber of MRI such that $k_{\rm MRI} = 3 \times 2\pi/L_z$. It can be seen that there are wave enhancements with strong directivity both in δv_z and δB_z. The directivity of the enhanced wave has the $k_x \sim k_y$ direction, i.e., $\pi/4, 5\pi/4$ radian from the

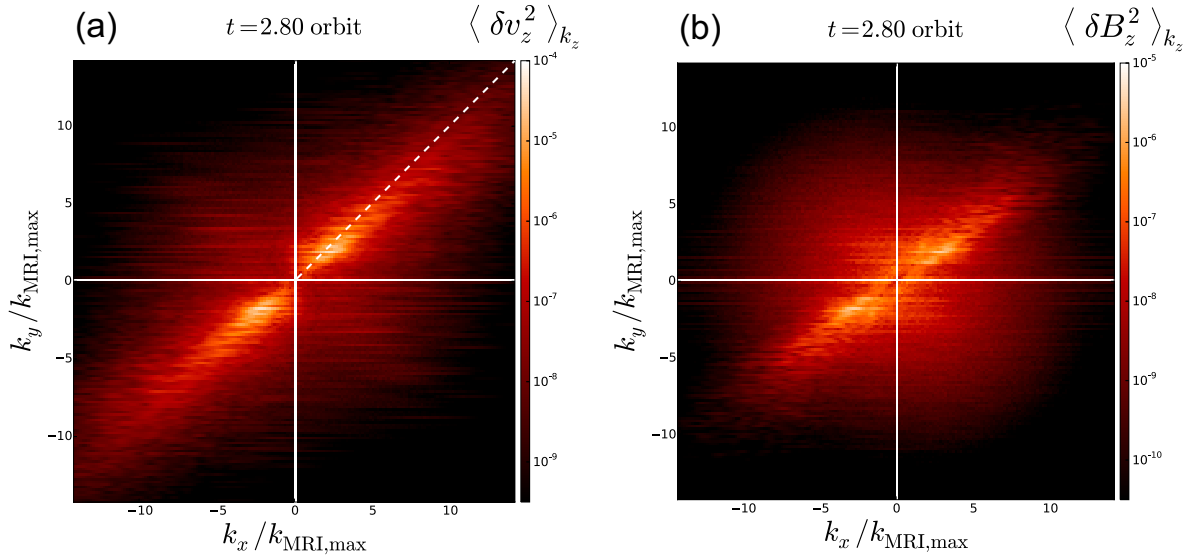

Fig. 3.6: Two-dimensional wavenumber spectra of (a) δv_z and (b) δB_z in the horizontal wavenumber plane averaged over vertical wavenumber direction at $t_{\mathrm{orbit}} = 2.8$.

radial direction both in v_z and B_z fields. This anisotropic wave enhancement is similar to that obtained from previous numerical studies (Lesur & Longaretti, 2011; Murphy & Pessah, 2015; Rembiasz et al., 2016). As Goodman & Xu (1994) and Pessah (2010) analytically pointed out, parasitic instability in an ideal MHD is a purely K-H mode; thus, it has the fastest growth rate with wavenumber vector $\boldsymbol{k}_{\mathrm{PI}}$ directing $\pi/4, 5\pi/4$ radian from the radial direction. In our calculation, the $\pi/4, 5\pi/4$ radian direction waves are enhanced both in v_z and B_z fields although there exists an antiparallel magnetic field in $3\pi/4, 7\pi/4$ radian direction as describe above. Therefore, we confirm that K-H mode parasitic instability is dominantly induced by MRI-driven shear flow in our calculation, as analytically described in previous studies. The existence of the enhancement of δv_z wave both in small and large wavenumber of $k_x = k_y$ region shows that the injected energy cascades while maintaining the anisotropic turbulent structure. This anisotropy is broken at the peak and the spectra becomes isotropic after that. This indicates that the laminated structure which induces the anisotropic energy cascade is broken at the peak, and the turbulent flow changes from anisotropic to isotropic.

Next, we check the detailed mechanism of transition from MRI to the state of magnetic turbulence via K-H mode parasitic instability. Figure 3.7 shows the time evolution of the vertically averaged wavenumber spectra of v_z in horizontal

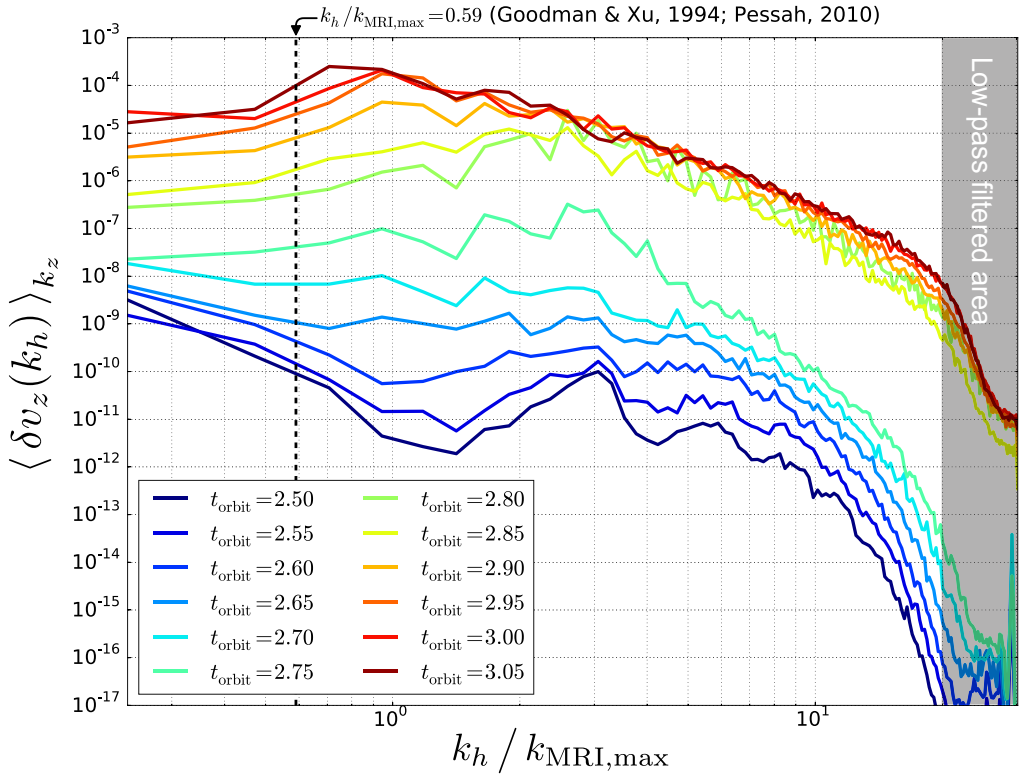

Fig. 3.7: Time evolution of vertically averaged wavenumber spectra of v_z in $k_h \equiv \sqrt{k_x^2 + k_y^2}$ along the $k_x = k_y$ direction.

wavenumber $k_h \equiv \sqrt{k_x^2 + k_y^2}$ along the $k_x = k_y$ direction, i.e., time evolution of the spectra along the white dashed line in panel (a) of Figure 3.6. The horizontal axis is the horizontal wavenumber $k_h \equiv \sqrt{k_x^2 + k_y^2} = \sqrt{2}k_x$ normalized by the MRI maximum growth wave number. Line colors, from cold color to hot colors, represent the time elapsed. The dotted line at $k_h/k_{\mathrm{MRI,max}} = 0.59$ represents analytically obtained maximum growth wavenumber of K-H mode parasitic instability. We can see the enhancement of energy of v_z at around $t_{\mathrm{orbit}} = 2.75$, which is considered to be because the roll up due to K-H mode parasitic instability increases the vertical component of the velocity. However, the fastest growth wavenumber in our simulation is around $k_h/k_{\mathrm{MRI}} = 2 \sim 3$, which is greater than analytically obtained fastest growth wavenumber $k_h/k_{\mathrm{MRI}} = 0.59$. This feature is a similar result to the result of Rembiasz et al. (2016) that is also obtained by the compressible MHD simulation using the high-order scheme although their simulation settings are different from ours; in particular, they didn't use Kepletrian rotational parameter. What is the difference between the simulation result and analytical studies? Analytical studies

usually assume that the simple shear flow and antiparallel magnetic field due to MRI grow with purely sinusoidal structure with maximum growth wavenumber of MRI and retain that structure until the saturation of MRI. For our simulation, Figure 2 shows that there exist multiple modes other than the maximum growth mode, though the maximum mode has the power one order of magnitude larger than those of other modes. The enhancement of a larger wavenumber wave of v_z (Figure 3.7) indicates that the shear flow is no longer purely sinusoidal and shows the importance of the existence of a smaller scale flow around the peak. To determine the phenomena that occur at the first peak, we examine the shear flow structure in the simulation result in detail. Figure 3.8 shows the structure of the parallel component of disturbed horizontal velocity $\delta v_{h,\parallel}$ in a surface with horizontal direction $h_{x=y}$ along the direction of $\hat{\boldsymbol{e}}_{x=y} \equiv (\hat{\boldsymbol{e}}_x + \hat{\boldsymbol{e}}_y)/\sqrt{2}$ and vertical direction z at $t_{\rm orbit}$ = (a) 2.75, (b) 2.80, (c) 2.85, and (d) 2.90. The parallel component of disturbed horizontal velocity is defined as

$$\delta v_{h,\parallel} \equiv \delta v_x \cos(\pi/4) + \delta v_y \sin(\pi/4). \tag{3.19}$$

Gray lines in all panels of Figure 3.8 represent the projection of streamlines depicted by disturbed velocity toward the $x = y$ direction surface, i.e., the lines are streamlines of the field defined as

$$\delta \boldsymbol{v}_{\parallel} = \delta v_{h,\parallel} \hat{\boldsymbol{e}}_{x=y} + \delta v_z \hat{\boldsymbol{e}}_z. \tag{3.20}$$

Although streamlines have both background flow $-q\Omega x \hat{\boldsymbol{e}}_y$ and perpendicular component of disturbed horizontal velocity $\delta v_{h,\perp}$, we can estimate the rough trend of the structure of the disturbed component of flow that induces K-H mode parasitic instability. At $t_{\rm orbit} = 2.75$, just before the peak, though the structure that has $k_z = k_{\rm MRI,max} = 3 \cdot 2\pi/L_z$ is mainly dominant, the shear flow structures induced by MRI at around $(h, z) = (-0.75H, 0.1H)$ and $(0.5H, 0.3H)$ become narrower and the flow speed of those region become faster, i.e., the flow structure become a jet-like structure and no longer purely sinusoidal. At $t_{\rm orbit} = 2.80$, these jet-like flow structures become unstable and winding, and then, the shear flow is torn up in those region after $t_{\rm orbit} = 2.85$. This process of creating narrower and faster flow and tearing shear flow with winding also can also be seen at $t_{\rm orbit} = 2.85$ and 2.90 at around $(h, z) = (-0.25H, 0.25H)$ and $(1.25H, -0.1H)$.

It is considered that the termination of growth and relaxation of turbulent stress is related to this collapse mechanism of shear flow. Since the relations of compo-

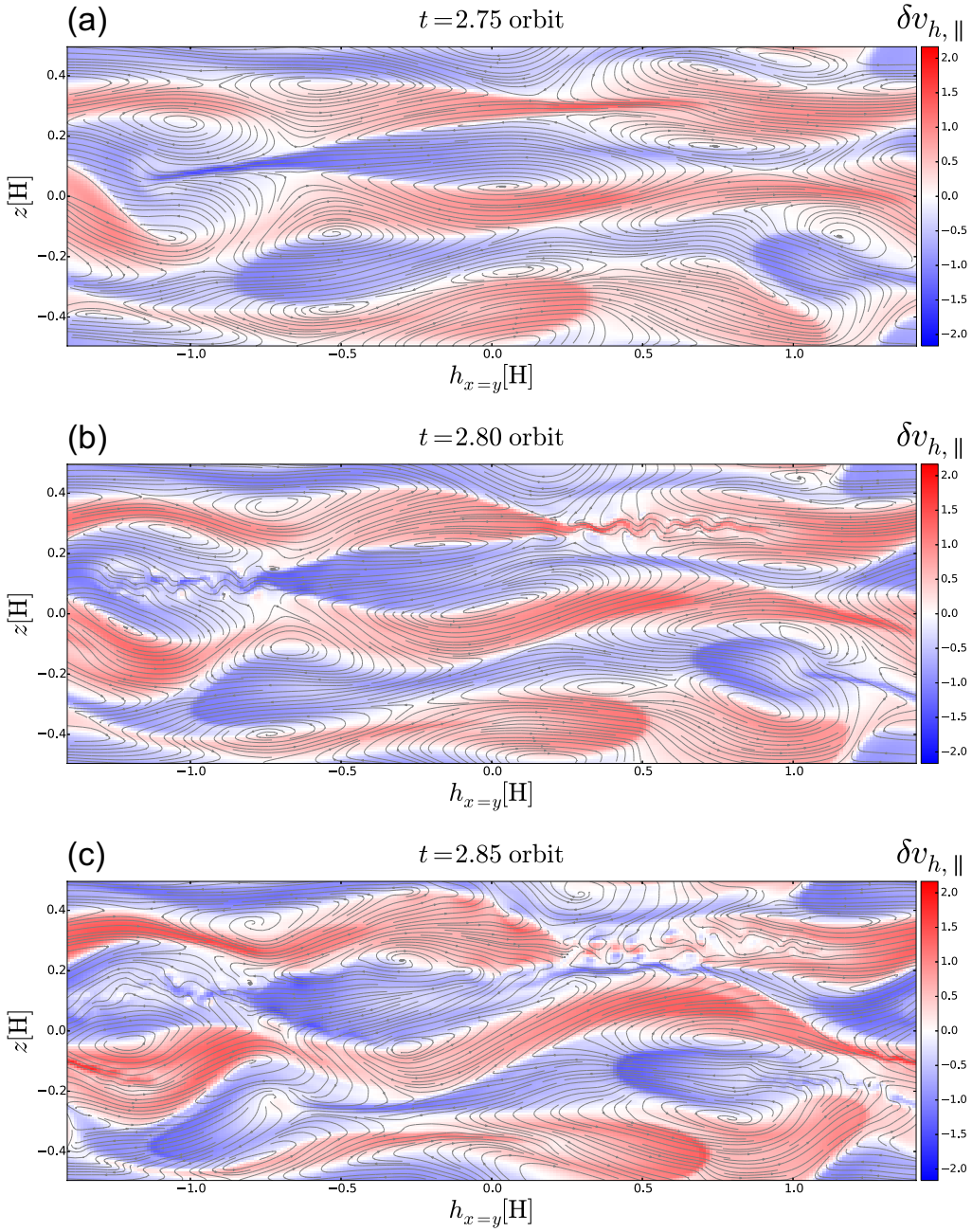

Fig. 3.8: Structure of the parallel component of disturbed horizontal velocity $\delta v_{h,\parallel}$ in a surface with horizontal direction $h_{x=y}$ along the direction of $\hat{\boldsymbol{e}}_{x=y} \equiv (\hat{\boldsymbol{e}}_x + \hat{\boldsymbol{e}}_y)/\sqrt{2}$ and vertical direction z at $t_{\rm orbit}$ = (a) 2.75, (b) 2.80, (c) 2.85, and (d) 2.90. Gray lines in all panels represent the projection of streamlines depicted by disturbed velocity toward the $x = y$ direction surface, i.e., streamlines of $\delta \boldsymbol{v}_{\parallel}$.

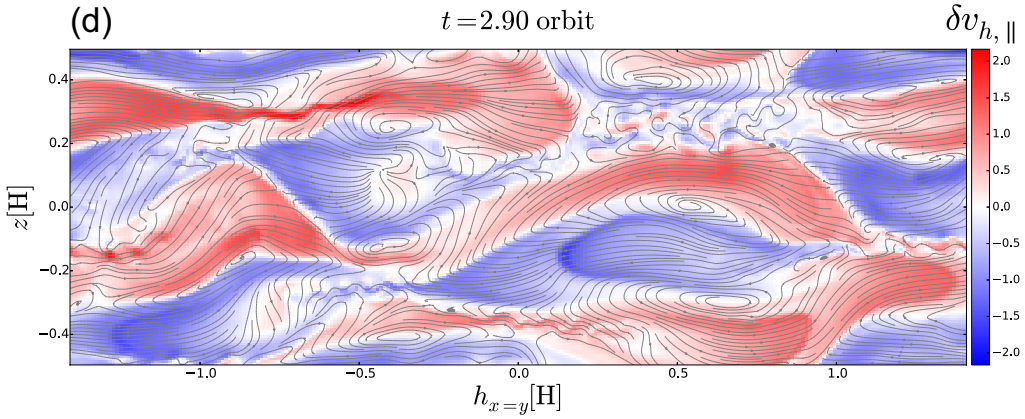

Fig. 3.8: (Continued)

nents of velocity and magnetic field in linear growth phase of MRI are as shown equation (3.18), the turbulent stress defined in equation (3.14) becomes positive and its growth increment is proportional to the amplitude of shear flow and antiparallel magnetic field structure. The termination of linear growth and relaxation of turbulent stress therefore indicate the collapse of the antiparallel disturbed field structures. The analytical study by Pessah (2010) assumes that the termination of MRI linear growth occurs at the time when the growth rate in the maximum growth mode of parasitic instability reaches the growth rate of MRI. The collapse of antiparallel disturbed field structure under this assumption is caused by roll up by vortices with the scale of maximum growth mode of parasitic instability. However, the collapse mechanism in our simulation is not so simple as described above. In our simulation, formation of narrow disturbed flow plays an important role for the termination of linear growth. It can be seen from Figure 3.8 that narrow flows are created by the interaction between vortices induced by the linear growth of K-H mode parasitic instability. The antiparallel vortices located at similar horizontal position, such as those at $(h_{x=y}, z) = (-1.1H, 0.25H)$ and $(-1.1H, -0.15H)$, create positive and negative vertical flow at similar horizontal position in the neighbouring laminar flow. This flow makes the horizontal laminar flow narrower and faster such as the structure at $(h_{x=y}, z) = (-0.75H, 0.1H)$ and $(0.25H, 0.3H)$. This narrow flow induces the small-scale K-H instability whose wavelength is much shorter than the preliminary induced K-H mode parasitic instability, and the vortices induced by this small-scale K-H tear up the narrow laminar flow itself. From the above discussion, the termination of laminar structure of the linear growth of MRI is not related to parasitic instability directly but the subsequent small-scale K-H

instability due to the interaction between the vortices induced by the K-H mode parasitic instability. This fact also indicates the importance of high-accuracy and high-resolution MHD calculation for resolving the termination of the linear growth of MRI. The vertical scale of jet-like flow structure becomes about one fifth to one eighth of the scale of the maximum growth wavelength of MRI just before the collapse of laminar flow in our calculation. In addition, the horizontal scale of winding of jet-like flow is about one third to one forth of the maximum growth wavelength of MRI (Figure 3.7), and this structure collapse into further smaller scale. These facts indicate that important scale for driving magnetic turbulence at the first peak is much smaller than the typical size of MRI, and our calculation resolves these flow structures by using about 5 to 10 grid points. Our calculation resolves these small-scale structures correctly because of the ability of our simulation code to resolve the wave by more than 4 grid points. It can be expected that MHD simulation, for revealing the mechanism of the termination of the MRI linear growth accurately, should have the ability to resolve much more smaller scale than the MRI maximum growth wavelength.

3.4.3 Termination mechanism comparison of the first peak and the peak in the nonlinear stage

In Section 3.4.2, we discussed the termination mechanism of MRI linear growth at the first peak. As described in Section 3.4.1, the growth and damping of turbulent stress is repeated every few orbits, and thus there exist some peaks after the first peak. Simply speaking, it can be expected that the peaks in the nonlinear phase are also generated in a way that is similar to the generation of the first peak. However, nonlinear peaks occur in much more turbulent state than the first peak. As Latter et al. (2009) pointed out, the mixing effect of that turbulent flow is not negligible for breaking a recurrently created channel flow. Therefore, it can be expected that 'clean' laminar flow such as MRI linear growth cannot exist due to turbulent mixing and thus the peak creation mechanism is not the same as the first peak. In this section, we analyze the nonlinear peak in a similar way as in Section 3.4.2 and discuss the difference in terms of the termination mechanism between the first peak and the nonlinear peaks.

To investigate the mechanism of occurrence of peaks in the nonlinear phase, we choose a peak at $t_{\rm orbit} = 29.8$ as the typical peak in the nonlinear phase and analyze the property in a similar way as in Section 3.4.2. The nonlinear peak at $t_{\rm orbit} = 29.8$

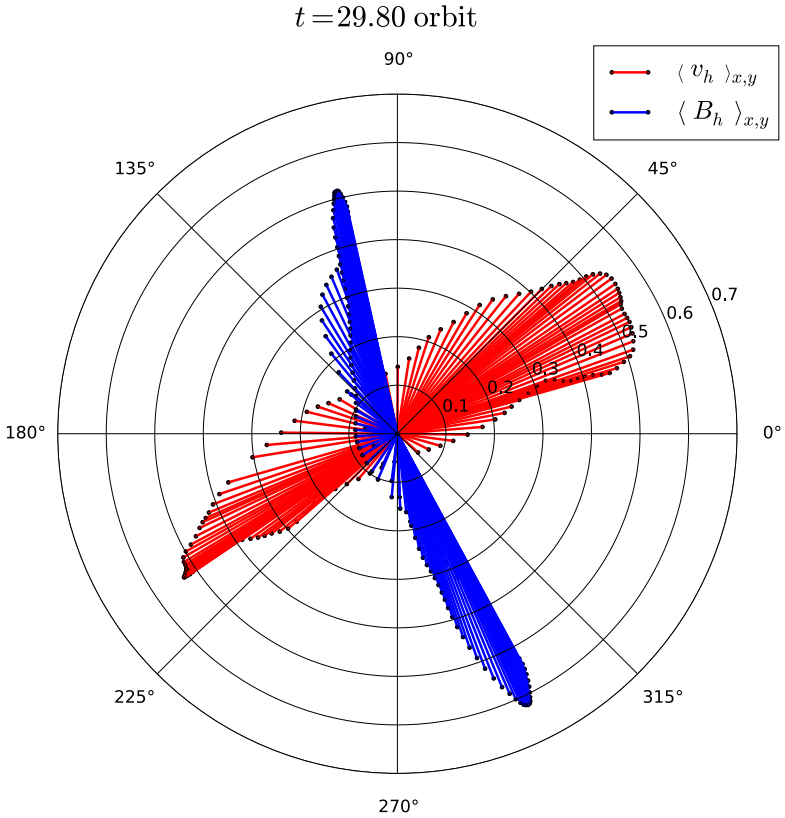

Fig. 3.9: Same as Figure 3.5, but for the nonlinear peak at $t_{\rm orbit} = 29.8$.

is the peak whose turbulent stress has one of the largest values in our simulation (Figure 3.3), and we assume this peak to be the typical one in the nonlinear phase. Figure 3.9 is plotted in the same way as Figure 3.5 but at $t_{\rm orbit} = 29.8$. Although there are much more variabilities in this case than the first peak, the horizontal vector of velocity field and magnetic field have directional characteristics. This direction angle is not exactly $\pi/4, 5\pi/4$ for the velocity field and $3\pi/4, 7\pi/4$ for the magnetic field like the one at the first peak, but the feature is similar. Therefore, it can be expected that there exist velocity shear flow and antiparallel magnetic field like the first peak and thus K-H mode parasitic instability is induced that tears up that field structure directly or indirectly. To confirm the enhancement of parasitic instability, we check the two-dimensional wavenumber spectra of the vertical velocity at $t_{\rm orbit} = 29.8$ as shown in Figure 3.6. Figure 3.10 is plotted in the same way as Figure 3.6 but at $t_{\rm orbit} = 29.8$. In the small wavenumber region, wave enhancement is observed at around $k_x = k_y$ region. This feature is similar to that shown in Figure 3.6. Therefore, parasitic instability seems to be induced and the

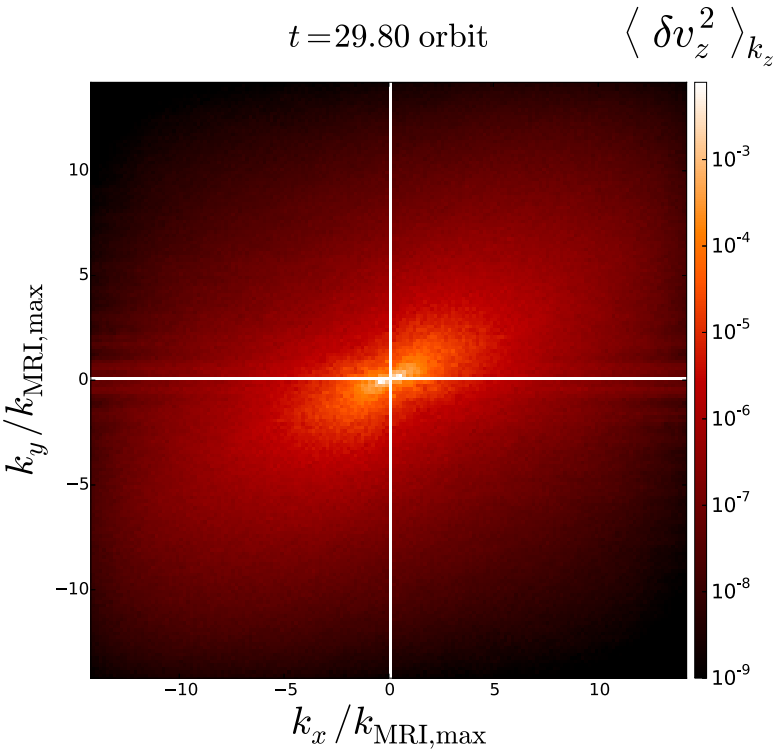

Fig. 3.10: Same as panel (a) of Figure 3.6, but for the nonlinear peak at $t_{\mathrm{orbit}} = 29.8$.

injected energy cascade, maintaining anisotropy. However, in the large wavenumber region, there is no wave enhancement of v_z in $k_x = k_y$. This feature indicates that the wave enhanced by parasitic instability in the small wavenumber region cascades without maintaining anisotropy unlike the one at the first peak (Figure 3.6). The reason for the difference of the horizontal two-dimensional wavenumber spectra between first and nonlinear peak is that the already existing large wavenumber and isotropic waves mix the anisotropic energy cascade and make it isotropic at the nonlinear peak.

Figure 3.11 is plotted in the same way as Figure 3.6 but at $t_{\mathrm{orbit}} =$ (a) 29.5, (b) 29.8, (c) 30.0, and (d) 30.1. At $t_{\mathrm{orbit}} = 29.5$, we can observe that there is dominant shear flow that has z-direction structure with wavenumber $k_z = 2\pi/L_z$ The amplitude of this restructured shear flow becomes larger at the peak timing around $t_{\mathrm{orbit}} = 29.8$; however, the structure of amplified channel flow is not homogeneous as can be seen in the snapshot for $t_{\mathrm{orbit}} = 29.8$. This locally existing channel flow structure seems to collapse after the peak and is broken into the small-scale

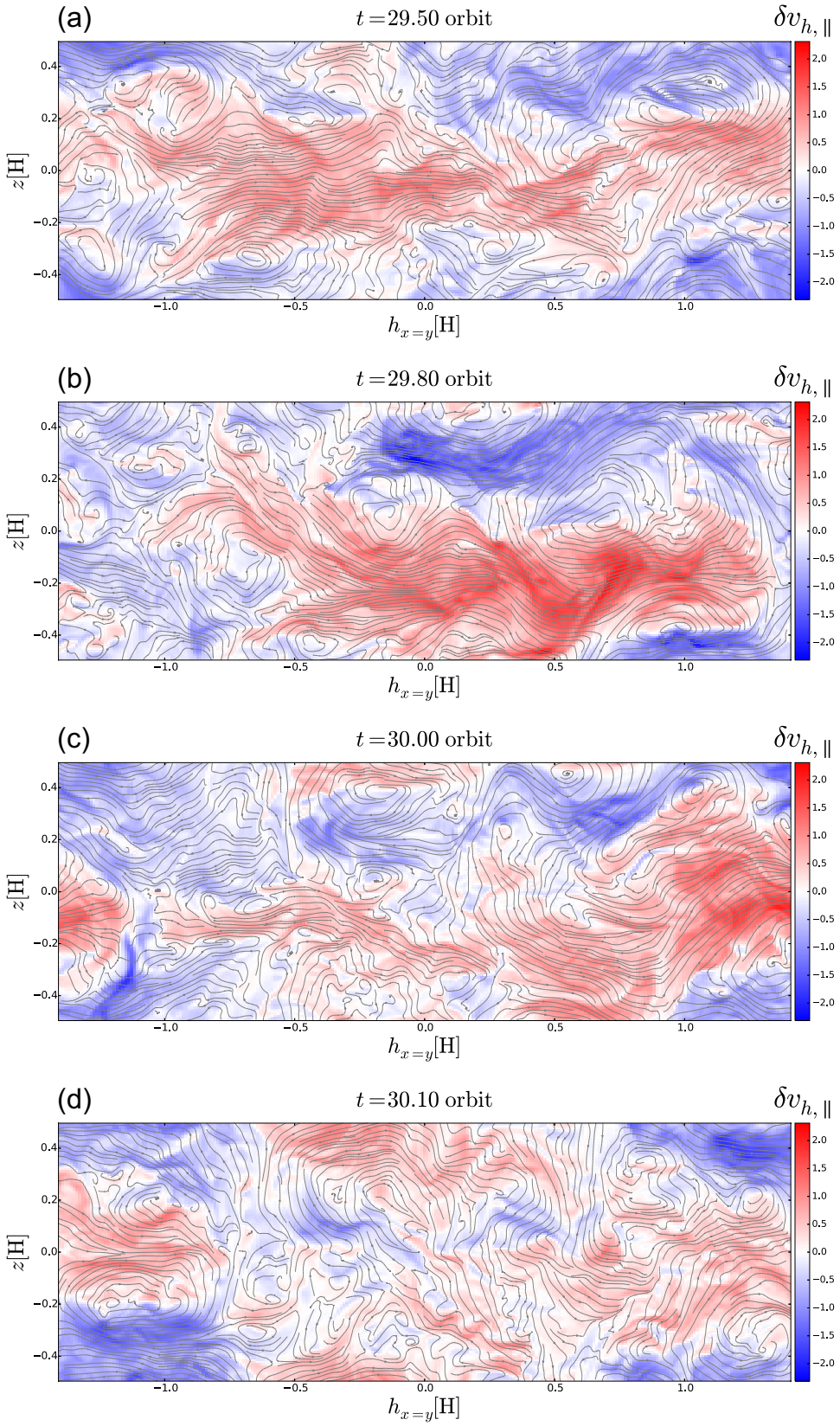

Fig. 3.11: Same as Figure 3.8, but at t_{orbit} = (a) 29.5, (b) 29.8, (c) 30.0, and (d) 30.1.

structures as can be seen as $t_{\rm orbit} = 30.0$ and 30.10.

The rough process of creating a peak of the stress, i.e., growth of the channel shear flow and its collapse into small-scale flow, is similar to that of the first peak. However, the collapse mechanism itself seems is not the same as first peak because of the existence of small-scale turbulent flow that is more isotropic than the large scale one (Figure 3.10). Although the restructured shear flow induces large scale wave in v_z by K-H mode parasitic instability as described above (Figure 3.10), the channel seems to be torn up not by the interaction of large scale vortices like the first peak but by the mixing of the small-scale turbulent flow. The small-scale flows already exist before the growth of restructured channel, and are not dissipated but sustained throughout the growth and relaxation of turbulent stress. Around the peak, the restructured shear flow induces vertical flow as large-scale vortices of K-H mode parasitic instability exist around the shear region. The small-scale flow structures, with small-scale shear flow, are vertically advected toward the flow region by the vertical flow. After that, they seem to mix with the restructured channel flow and break its structure.

As described above, the collapse of the restructured channel flow reproduced in our simulation is due to coexistence of the large-scale vortices induced by parasitic instability and the small-scale turbulent flow structure which continues to exist throughout the collapse process. This indicates that the small-scale flow structure plays an important role for collapsing not only linear MRI-channel but also the restructured channel structure. Although the collapse process becomes more complicated as we solve turbulent flow more preciously, this fact also indicate the necessity for ability of resolving waves whose wavenumber is significantly larger than the typical wavenumber of MRI and parasitic instability.

3.5 Concluding remarks

We carried out the three-dimensional ideal MHD simulation of MRI-driven turbulence in a shearing box by using a newly developed high-order MHD simulation code. We discussed the enhancement of parasitic instability and importance of small-scale flow to have the peak of turbulent stress at the first and nonlinear peaks. The magnetic turbulence in accretion disks under ideal MHD is expected to be driven by K-H mode parasitic instability which is a secondary instability induced by MRI (Goodman & Xu, 1994). Although previous numerical simulations identified the enhancement of parasitic instability (Lesur & Longaretti, 2011; Murphy

& Pessah, 2015) and reported that the maximum growth wavenumber of parasitic instability at the first peak is larger value than analytical estimation (Rembiasz et al., 2016), the detailed process of driving magnetic turbulence and the role of small-scale flow on it are not fully revealed. To investigate these by MHD simulation, we applied the shearing box boundary condition to the newly developed high-order MHD code. Whereas many of previous MHD simulations uses a shock capturing-type scheme that is not suitable for resolving wave fine structures, our code can accurately resolve turbulent flow using lesser number of grid, and thus enable us to investigate the role of small-scale flow at the generation of parasitic instability and the creation of the peak of stress.

At the first peak of the turbulent stress, i.e., at $t_{\rm orbit} \sim 2.8$, we showed the anisotropic wave enhancement in two-dimensional wavenumber spectrum of vertical velocity due to the excitation of parasitic instability. The fastest enhancement wavenumber of this wave is much larger than that obtained analytically, and this feature is similar result to Rembiasz et al. (2016) though they assumed different setting from ours. We found that this feature is because the interaction of vertically located growing vortices induced by parasitic instability makes the layered structure of disturbed flow narrower and faster, and then the jet-like structure induces much smaller and faster growing K-H-like instability just before the peak. This newly induced instability makes MRI-created layered flow structure to tear off and thus the turbulent stress decreases. The first peak creation process in our simulation is summarised as follows. First, MRI is linearly grows and results in layered structures of disturbed field. Meanwhile, K-H mode parasitic instability grows and results in a few vortices. Then, the vertically located vortices make the layered flow structure narrower and faster. Finally, the created jet-like structure becomes unstable and the layered structure tears off, and thus the turbulent stress decreases.

We also showed the analysis results of the arbitrarily chosen nonlinear peak at $t_{\rm orbit} \sim 29.8$ to discuss the creation mechanism of the peak and the difference from the first peak. The anisotropic wave enhancement of parasitic instability is observed in two-dimensional wavenumber spectrum of vertical velocity. The anisotropic spectrum is, however, found only in the small wavenumber region, while large wavenumber waves are more isotropic than those at the first peak. This indicates that a nonlinear peak is created in an environment where large-scale and anisotropic parasitic mode waves and isotropic turbulent waves coexist. The restructured channel flow starts to collapse at the nonlinear peak, but the mechanism is not obvious because of the existence of the small-scale turbulent structure.

We showed that large-scale vortices induced by restructured flow effectively advect small-scale shear structures from the shear region toward the flow region of the restructured channel, and the advected structure seems to mix and break the restructured channel structure.

The peak creation and driving magnetic turbulence mechanism, i.e., the collapse mechanism of channel flow structure, is related to the destruction of large-scale structure by small-scale flow both in linear phase and nonlinear phase. This fact indicates the possibility that factors that change the small-scale structure of flow, such as the magnetic diffusivity and viscosity, can change the peak values and evolution processes in the linear and nonlinear stages. Some numerical studies already reported that slight amount of diffusivity originated from physical (Fromang et al., 2007) and numerical effects (Minoshima et al., 2015) changes the value of turbulent stress. It can be considered that these features are due to the variation of small-scale structure by changing the diffusivities. Detailed mechanism of generating these variations should be investigated by the high-order and high-resolution MHD simulation.

Chapter 4

MHD simulation of MRI-driven turbulence in visco-resistive MHD conditions

4.1 Introduction to MRI-driven turbulence in visco-resistive MHD conditions

In chapter 3, we showed the importance of the small-scale flow for creation of the peaks of turbulent stress. At the first peak, Kelvin-Helmholtz mode parasitic instability is enhanced with anisotropic wavenumber spectra by a layered shear flow induced by MRI (Figure 3.6). An interaction of vortices induced by K-H mode parasitic instability makes shear flow structure narrower and faster, i.e., the flow becomes jet-like structure (Figure 3.8). This small-scale structure induces subsequent small-scale K-H instability and becomes unstable rapidly. And thus, the laminar structure is collapsed from this region and this results in the relaxation of the turbulent stress. On the other hand, the restructured shear flow enhanced by MRI seems to be collapsed by a mixing due to coexistence of the large-scale anisotropic vortices and small-scale isotropic flow structure at a peak in nonlinear phase. The large-scale vortices vertically advect small-scale shear structures from the shear region to flow region of the large-scale shear flow. The creation mechanisms of first peak and peaks in nonlinear phase are different, nonetheless, small-scale flow structure works important roles for both peaks. From this result, it can be expected that the driving mechanism of turbulence and value of peaks

can be controlled by factors that change the small structure of flow, such as small amount of the magnetic diffusivity and fluid viscosity.

The effects of diffusivities such as the magnetic diffusivity and fluid viscosity to linear growth of MRI, linear growth of parasitic instability, and MRI-driven turbulence ware discussed analytically and numerically by previous studies. The effect of magnetic diffusivity to the linear growth of MRI was particularly well discussed focusing on the protoplanetary disks. In the protoplanetary disks, the disk gas is partially ionized plasma because the gas is dense and central body is not so energetic to ionize thermally (Umebayashi & Nakano, 1988). In this condition, the behaviour of plasma can be taken as the resistive MHD condition where the magnetic diffusivity η is proportional to the ratio of the number density of neutral and electron (e.g. Blaes & Balbus, 1994). Jin (1996) and Sano & Miyama (1999) reported the dispersion relation and growth rate of MRI in such resistive MHD condition. They showed that the maximum growth rate, maximum growth wavenumber, and critical wavenumber of MRI significantly decreases when the magnetic Reynolds number $Rm \equiv v_{\rm A}^2/\eta\Omega$ becomes less than unity. In addition, they showed that the property of linear growth of MRI is hardly changed at all when Rm is much larger than unity. On the other hand, the viscosity ware usually neglected because the molecular viscosity is so small in space fluid, and thus the viscous effect to linear growth of MRI had not been discussed for a long time. Lesur & Longaretti (2007) and Fromang et al. (2007) reported that the turbulent stress obtained by numerical simulation is affected by the magnetic Prandtl number defined as the ratio of the fluid viscosity and magnetic diffusivity though these value set as very low value. In addition, Masada et al. (2007) suggested that the accretion disks created in the proto-neutron stars called collapsar disk have large viscosity because the disk is so hot and dense and the neutrino works as the viscosity in such condition. Furthermore, MRI was recently reproduced in laboratory plasma where the viscosity is a little larger than that in astrophysical plasma (Nornberg et al., 2010). Pessah & Chan (2008) reported the dispersion relation and growth rate of MRI in viscous and visco-resistive MHD condition They showed that the maximum growth rate and maximum growth wavenumber also significantly decrease when the Reynolds number $Re \equiv v_{\rm A}^2/\nu\Omega$ becomes less than unity, and the fluid viscosity does not change the critical wavenumber of MRI, i.e., the wavenumber range where MRI occurs does not change. In addition, they showed that the property of linear growth of MRI is hardly changed at all when Re is much larger than unity. These linear analyses indicate that whether the property of linear growth of MRI is similar to

that in ideal MHD condition and that the property changes depending on whether Re or Rm is greater than unity.

The property of linear growth of parasitic instability is also changed by the variation of magnetic diffusivity and viscosity. The reasons of this are explained by the following three points. The first point is that the eigenvector of the linear mode of MRI is varied by changing diffusion parameters. Pessah & Chan (2008) showed that the direction and amplitude of shear flow and antiparallel magnetic field created by linear growth of MRI is modified by changing Re and Rm. This fact results in that the wavenumber vector of maximum growth mode of parasitic instability is also modified by changing Re and Rm (Pessah & Goodman, 2009; Pessah, 2010). The second point is that the magnetic diffusivity controls the fastest growth mode of parasitic instability, i.e., Kelvin-Helmholtz (K-H) mode or magnetic reconnection mode as mentioned in Section 1.3. When the magnetic diffusivity increases, i.e., Rm decreases, the dominant mode is changed from K-H mode to magnetic reconnection mode, and thus, the direction of wavenumber vector of parasitic instability is also changed from the direction of shear flow to that of antiparallel magnetic field created by the growth of MRI. Pessah & Goodman (2009) and Pessah (2010) analytically showed that the threshold of this change is $Rm = 1$, and the linear growth rate of K-H mode and reconnection mode become comparable when $Rm = 1$. The third point is that the fluid viscosity controls the amplitudes of the shear flow and antiparallel magnetic field when the saturation of growth of MRI. As described in Section 1.3, the amplitude of shear flow and antiparallel magnetic field increase exponentially with time, and thus the growth rate of parasitic instability also grows with time. Pessah & Goodman (2009); Pessah (2010) analytically showed that the amplitude of antiparallel magnetic field at the time that growth rate of parasitic instability reaches that of MRI takes larger value in the case that $Rm \gg 1$ and $Re \sim 1$. They pointed out that this is because of quench of K-H instability due to the fluid viscosity. According to these three points, the property of parasitic instability, such as the fastest growth mode, the fastest growth wavenumber vector and growth rate, and amplitude of MRI at the saturation, are affected in the discussion of linear analysis by changing the diffusion parameters. We would like to note that these variations converge to the values in ideal MHD condition in the case both Re and Rm are much larger than unity, such that $Re, Rm > 100$.

The studies introduced above are all in the discussion of linear phase. The diffusion effects to nonlinear phase are studied numerically. Sano & Inutsuka (2001)

carried out three-dimensional simulation with the strong magnetic diffusivity those are $Rm = 1$. They showed that the magnetic reconnection, induced by physical diffusivity, plays an important role at the recurrent peaks in nonlinear phase. They pointed out that the magnetic reconnection effectively convert magnetic energy increased by recurrently occurred MRI to the thermal energy in resistive MHD condition. Masada & Sano (2008) carried out two-dimensional axisymmetric simulations with varying the magnetic diffusivity and viscosity in wide range. They showed that the temporally averaged turbulent stress becomes small when Rm becomes less than unity, and becomes large when Re becomes less than unity, and not modified by Re and Rm when they are much larger than unity. Lesur & Longaretti (2007) and Fromang et al. (2007) carried out three-dimensional simulations with relatively large Re and Rm ($Re, Rm \gg 10$), and reported the relations between turbulent stress and magnetic Prandtl number defined as $Pm = Rm/Re$. Lesur & Longaretti (2007) carried out simulation with the net vertical initial magnetic field, and they showed that there is positive correlation between the temporal and spatial averaged turbulent stress and the magnetic Prandtl number in that kind of initial magnetic field. Fromang et al. (2007) carried out simulation with the zero-net vertical initial magnetic field, and they showed that the similar correlation between the turbulent stress and Pm as reported by Lesur & Longaretti (2007), and also reported that the turbulence become damped when $Pm \lesssim 1$ in that kind of initial magnetic field. In addition to these studies, Minoshima et al. (2015) carried out three-dimensional simulations in ideal MHD condition by several types of simulation schemes, such as various Riemann solvers and reconstruction methods, and showed that the saturation level and temporally averaged value of turbulent stress are strongly affected by changing simulation scheme. They pointed out this feature is caused because the small amount of numerical magnetic diffusivity and viscosity are modified by changing schemes, and thus the numerical magnetic Prandtl number is changed, then the stress value varies as with the studies by Lesur & Longaretti (2007) and Fromang et al. (2007). These previous studies suggested that the evolutional process of MRI-driven turbulence is also affected by small amount of diffusivity, though the property of the linear growth of MRI and parasitic instability is hardly changed in that condition of diffusivity. Because the small amount of diffusion effects attenuate the large wavenumber component of magnetic turbulence by blunting the small-scale structure of the flow and magnetic field, this fact pointed out by previous studies indicates the possibility that the modifying small-scale structure plays an important role for determining saturation level and

temporally averaged value of turbulent stress, though turbulent stress is spatially averaged comprehensive value. However, the details such as how the structures created by MRI and parasitic instability are modified and how the saturation values are changed by small amount of diffusivity are still unclear.

As described in Chapter 3, we found that the creation of small-scale and jet-like structure and coexistence of small-scale shear flow structures and large-scale vortices collapse the channel structure created by MRI at the first peak and nonlinear peak, respectively. Considering this result, it is predicted that the small amount of diffusion effects modify these small-scale flow structures, and thus the collapse process and timing of MRI-induced shear structure also should be modified. Since our developed code particularly can solve the small-scale flow structure wavenumber spectra accurately, it can be expected that our code can capture what phenomena are modified at the peak by changing the diffusion effects.

In this chapter, we show the simulation results of MRI-driven turbulence in visco-resistive MHD conditions and discuss the detailed phenomena. In Section 4.2, we first revisit the linear property of MRI in visco-resistive MHD condition according to previous works (e.g. Pessah & Chan, 2008). In Section 4.3, we describe the simulation settings for visco-resistive MHD simulation. In Section 4.4, we show the simulation results and discuss the difference in several diffusivity models. We firstly show the time evolution of turbulent stress in Section 4.4.2, and discuss the difference and its cause of the stress value at the first peak and nonlinear peak, and the temporally averaged value in diffusion parameter space in Section 4.4.3. We discuss the detailed phenomena occurring at the first and nonlinear peaks in Section 4.4.4 and 4.4.5 by using the similar way to chapter 3. In Section 4.5, we summarize the results of visco-resistive simulations.

4.2 Linear analysis of MRI in visco-resistive MHD conditions

In this section, we revisit the property of MRI in visco-resistive MHD condition shown by Sano & Miyama (1999), Pessah & Chan (2008), Latter et al. (2009), and so on. We use the same simplification and same coordinate system as we used in Section 3.2. In addition to this, we introduce the viscosity and magnetic diffusivity into Equations (3.1) and (3.2) The visco-resistive case of Equations (3.1) and (3.2)

can be written as follows

$$\frac{\partial(\rho \boldsymbol{v})}{\partial t} + \boldsymbol{\nabla} \cdot \left[\rho \boldsymbol{v}\boldsymbol{v} - \frac{\boldsymbol{B}\boldsymbol{B}}{4\pi} + \left(p + \frac{B^2}{8\pi} \right) \boldsymbol{I} \right] = \mu \nabla^2 \boldsymbol{v} + 2q\Omega^2 \rho x \hat{\boldsymbol{e}}_x - 2\rho \boldsymbol{\Omega} \times \boldsymbol{v}, \tag{4.1}$$

$$\frac{\partial \boldsymbol{B}}{\partial t} + \boldsymbol{\nabla} \cdot [\boldsymbol{v}\boldsymbol{B} - \boldsymbol{B}\boldsymbol{v}] = \eta \nabla^2 \boldsymbol{B}, \tag{4.2}$$

where μ and η are the dynamic shear viscosity and magnetic diffusivity. We use the same equilibrium condition of velocity and magnetic field as Equation (3.3), and similarly apply the Fourier mode perturbations that is Equation (3.4). By calculating with same operation as Section 3.2, we can obtain the visco-resistive version of Equation (3.5) as follows.

$$\begin{pmatrix} -\nu k_z^2 & 2i\Omega & -\frac{v_A^2 k_z}{B_0} & 0 \\ -i(2-q)\Omega & -\nu k_z^2 & 0 & -\frac{v_A^2 k_z}{B_0} \\ -B_0 k_z & 0 & -\eta k_z^2 & 0 \\ 0 & -B_0 k_z & iq\Omega & -\eta k_z^2 \end{pmatrix} \begin{pmatrix} v_{1x} \\ v_{1y} \\ B_{1x} \\ B_{1y} \end{pmatrix} = \omega \begin{pmatrix} v_{1x} \\ v_{1y} \\ B_{1x} \\ B_{1y} \end{pmatrix}, \tag{4.3}$$

where v_A is the Alfven velocity defined as $v_A^2 = \frac{B_0^2}{4\pi\rho}$, and ν is kinematic viscosity defined as $\nu \equiv \mu/\rho$. The dispersion relation correspond to the eigenfunction of the matrix in Equation (4.3), and can be written as

$$(\omega_\nu \omega_\eta - v_A^2 k_z^2)^2 - 2(2-q)\Omega^2 \omega_\eta^2 - 2q\Omega^2 v_A^2 k_z^2 = 0, \tag{4.4}$$

where ω_ν and ω_η are defined as

$$\omega_\nu \equiv \omega + i\nu k_z^2, \quad \omega_\eta \equiv \omega + i\eta k_z^2, \tag{4.5}$$

respectively. Figures 4.1, 4.2, and 4.3 show the solution of this dispersion relation in the resistive, viscous, and the magnetic Prandtl number $Pm = \nu/\eta = 1$ conditions, respectively. Panel (a) and panel (b) in all figures show the growth rate $\Im(\omega)$ and the angle of perturbed velocity and magnetic field of instability mode that are $\theta_v = \arctan(\delta v_y / \delta v_x)$ and $\theta_B = \arctan(\delta B_y / \delta B_x)$, respectively (see Section 3.2). The colors of lines in all figures represent the strength of diffusivities indicated by Reynolds number and magnetic Reynolds number. The Reynolds number, magnetic Reynolds number, and magnetic Prandtl number are non-dimensional parameters which indicate the strength of viscosity, magnetic diffusivity, and those ratio,

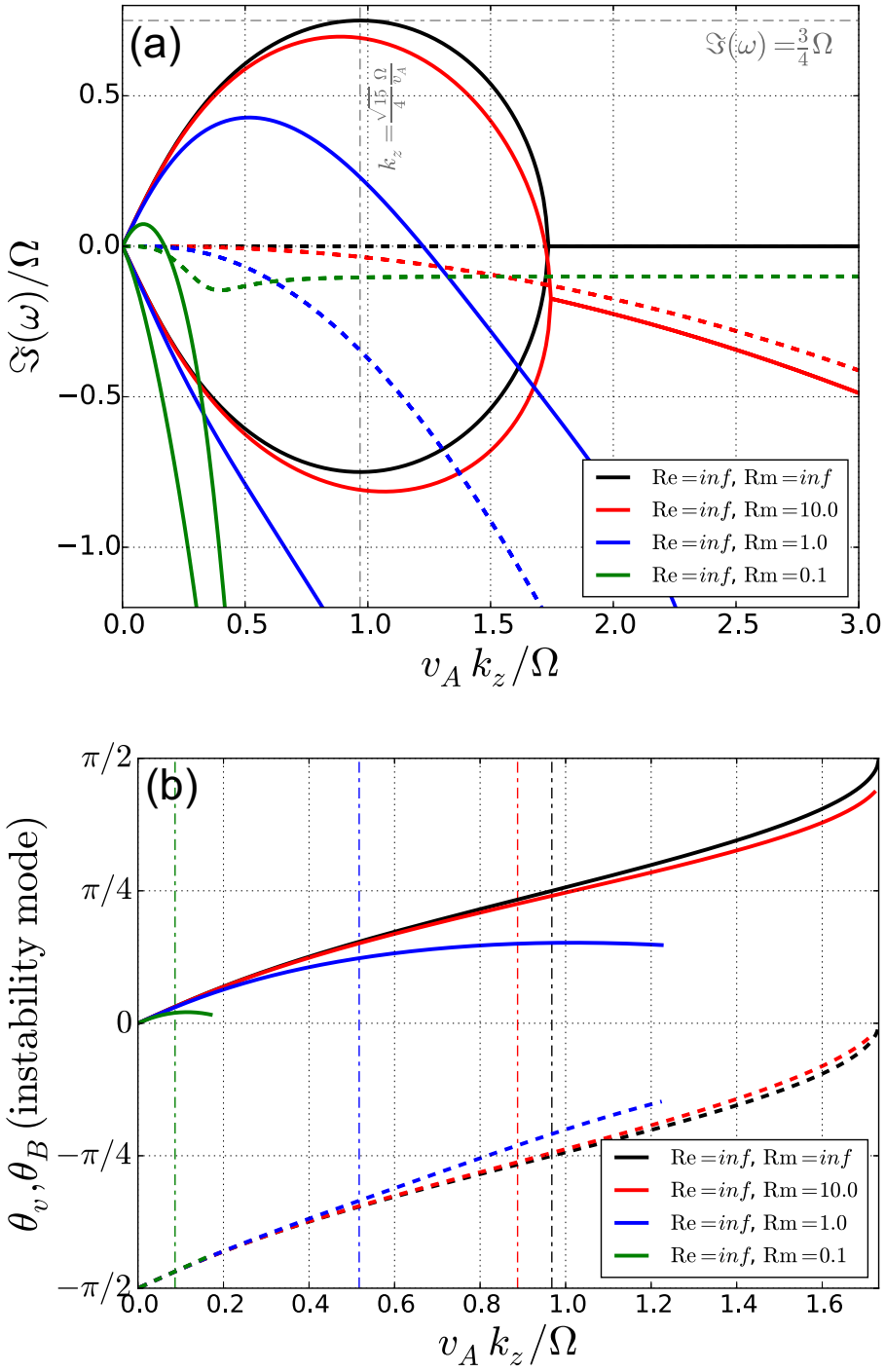

Fig. 4.1: The solution of linear analysis of MRI in the resistive MHD condition. Black, red, blue, and green colors of all lines in both panels represent $Rm = \infty$, 10, 1, and 0.1, respectively. Panel (a): imaginary part of angular frequency ω, i.e., the growth rate. Solid lines show the mode which has unstable solution, and dotted lines shows the mode which has purely oscillation solution. Vertical and horizontal dash-dotted gray lines denote the wavenumber and growth rate of the maximum growth mode in ideal MHD condition. Panel (b): The angles formed by perturbation components of velocity and magnetic field satisfying Equation (4.3), i.e., $\theta_v = \arctan(v_{1y}/v_{1x})$ (solid line) and $\theta_B = \arctan(B_{1y}/B_{1x})$ (dotted line), respectively. Vertical dash-dotted lines represent the maximum growth wavenumber of each color's diffusivity.

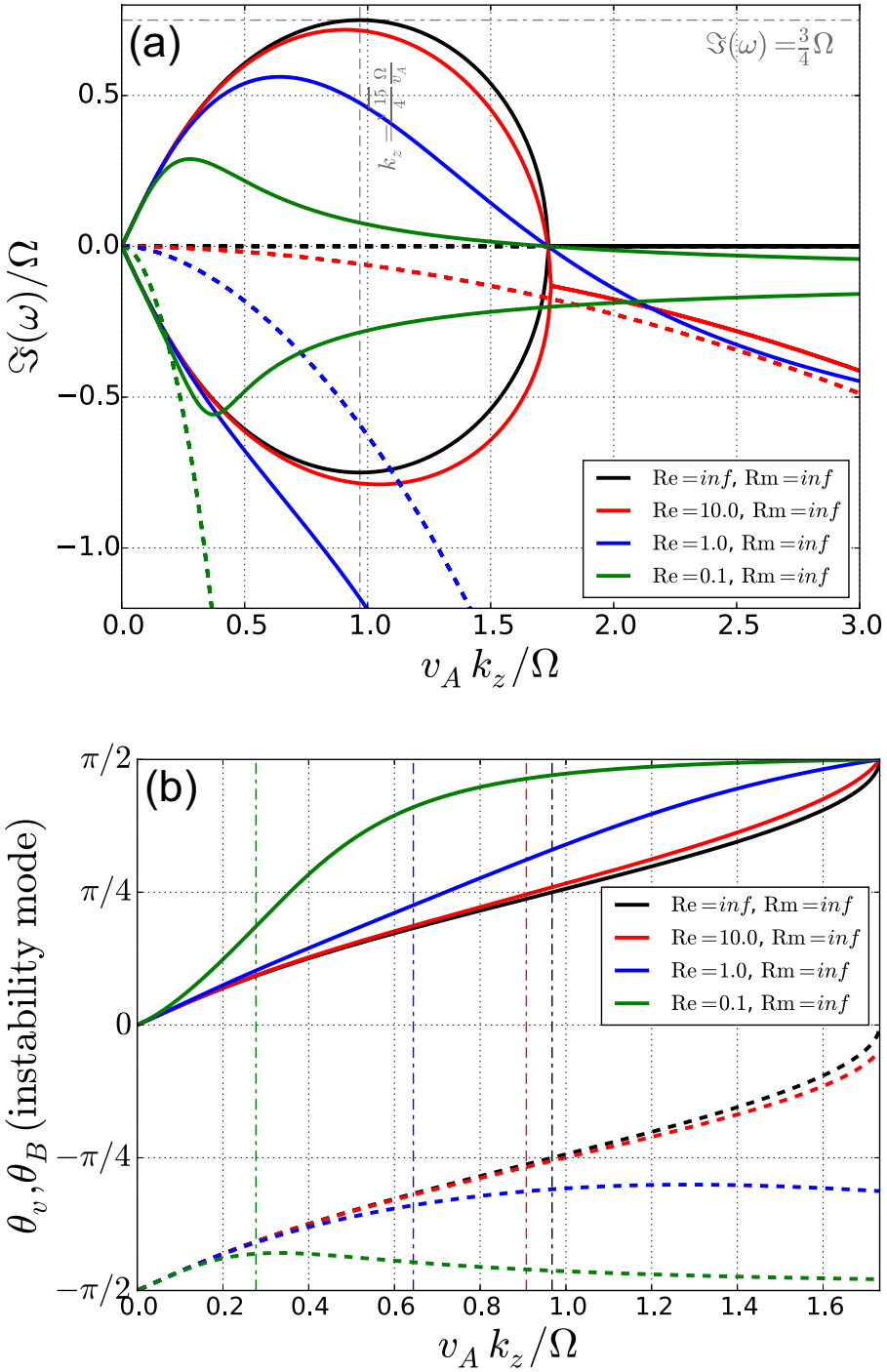

Fig. 4.2: Same plot as Figure 4.1 but for the viscous MHD condition. Black, red, blue, and green colors of all lines in both panels represent $Re = \infty$, 10, 1, and 0.1, respectively.

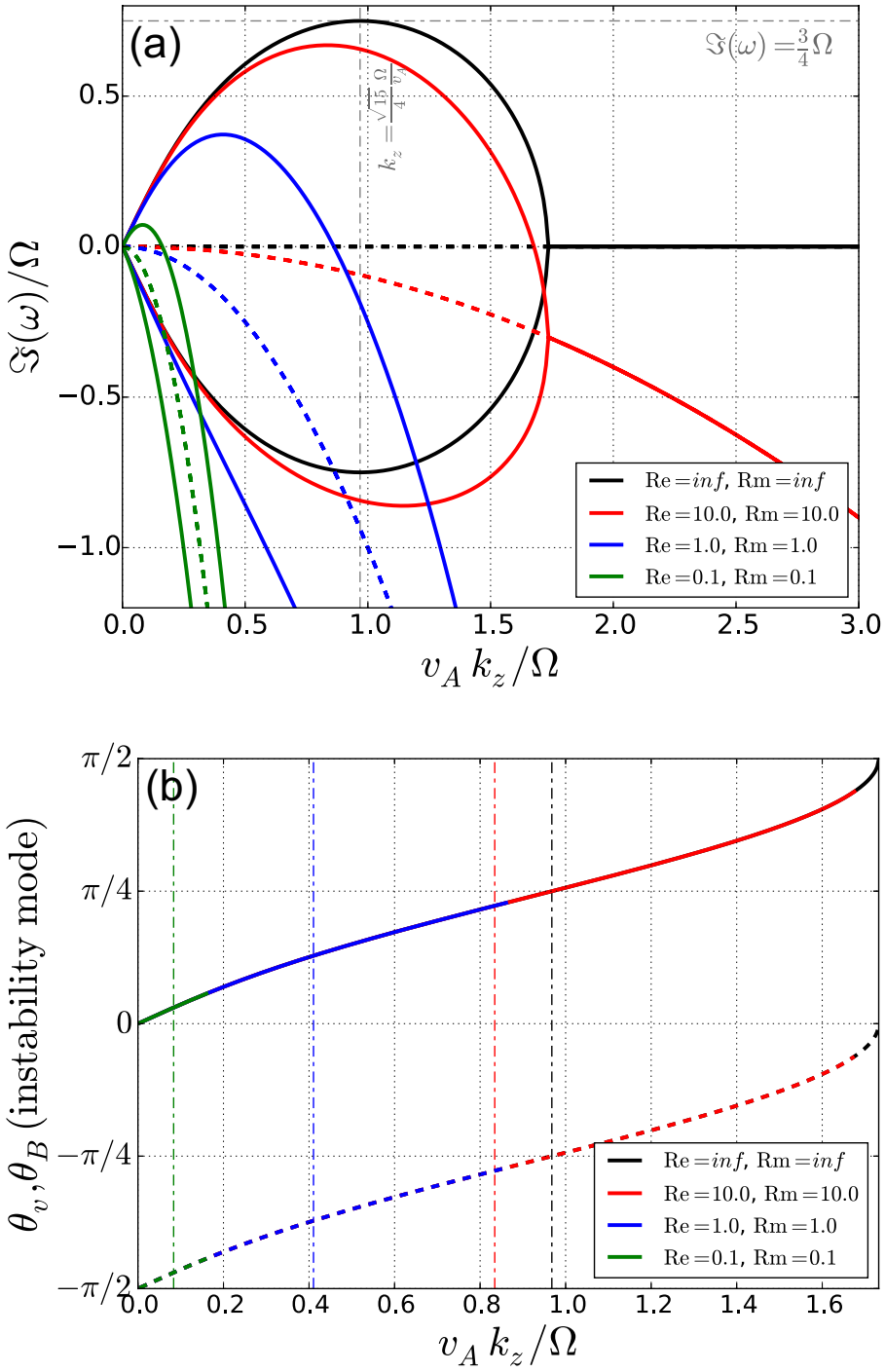

Fig. 4.3: Same plot as Figure 4.1 but for one of the visco-resistive MHD condition such as magnetic Prandtl number $Pm = Rm/Re = 1$. Black, red, blue, and green colors of all lines in both panels represent $Re = Rm = \infty$, 10, 1, and 0.1, respectively.

and defined as

$$Re \equiv \frac{\rho v_A^2}{\mu\Omega}, \quad Rm \equiv \frac{v_A^2}{\eta\Omega}, \quad Pm \equiv \frac{Rm}{Re} = \frac{\nu}{\eta}, \tag{4.6}$$

respectively. Black, red, blue, and green colors of all lines in both panels of Figure 4.1 represent $Rm = \infty$, 10, 1, and 0.1, respectively. Black, red, blue, and green colors of all lines in both panels of Figure 4.2 represent $Re = \infty$, 10, 1, and 0.1, respectively. Black, red, blue, and green colors of all lines in both panels of Figure 4.3 represent $Re = Rm = \infty$, 10, 1, and 0.1, respectively. In the panel (a) of all figures, the solid lines and the dashed lines represent the modes which have unstable or decay solutions and the modes which have purely oscillation solutions, respectively (see Section 3.2). We can confirm that decreasing Re and/or Rm, i.e., increasing viscosity and magnetic diffusivity, decreases the maximum growth rate of MRI. This tendency becomes remarkable particularly when Re, $Rm \leq 1$ as shown by Pessah & Chan (2008). In the case that Rm, $Re \geq 10$, modification of maximum growth rate and maximum growth wavenumber are relatively small. Therefore, in the condition of Rm, $Re \geq 10$, it is considered that the disturbance fields grow on similar structures and time scale in the linear process. In the panel (b) of all figures, the solid and dashed lines respectively show θ_v and θ_B of the instability mode. The angles of maximum growth mode are modified by decreasing Re or Rm. Decreasing Re and/or Rm basically decreases both θ_v and θ_B. This fact indicates that the diffusion terms not only control the balance of modes of parasitic instability between the K-H mode and magnetic reconnection mode but also change the direction of the shear flow and the antiparallel magnetic field that are created by MRI and become the energy source of the parasitic instability modes. From this reason, as Pessah & Goodman (2009) and Pessah (2010) pointed out, the direction and mode of parasitic instability become complicated when Re or Rm are around the unity. Note that both θ_v and θ_B in the condition that $Re, Rm \geq 10$ are not significantly changed from those in the ideal condition.

4.3 Simulation setup

We carried out visco-resistive simulations with similar physical settings to chapter 3, and introducing several strength of physical diffusivities. Besides introducing physical diffusivities, here we assume the plasma is isothermal, i.e., the temperature $Te = p/\rho = c_s^2$ keeps constant and specific heat $\gamma = 1$. This assumption prevent plasma from being heated unlimitedly because of the ohmic heating caused by

the magnetic diffusivity. The governing equations, Equations (2.1) to (2.3), are rewritten under the isothermal assumption as follows.

$$\frac{\partial \rho}{\partial t} + \boldsymbol{\nabla} \cdot (\rho \boldsymbol{v}) = 0, \tag{4.7}$$

$$\frac{\partial (\rho \boldsymbol{v})}{\partial t} + \boldsymbol{\nabla} \cdot \left[\rho \boldsymbol{v}\boldsymbol{u} - \boldsymbol{B}\boldsymbol{B} + \left(p + \frac{B^2}{2} \right) \boldsymbol{I} \right] = \boldsymbol{\nabla} \cdot \mathbf{R} + \boldsymbol{S}_{\mathrm{Momentum}}, \tag{4.8}$$

$$\frac{\partial \boldsymbol{B}}{\partial t} + \boldsymbol{\nabla} \cdot (\boldsymbol{v}\boldsymbol{B} - \boldsymbol{B}\boldsymbol{v}) = \boldsymbol{\nabla} \times (-\eta \boldsymbol{j}), \tag{4.9}$$

$$p/\rho = \text{constant}, \tag{4.10}$$

where all physical quantities are the same as explained in Section 2.2, and Equation (4.10) is the equation of state is isothermal fluid. The first terms of right hand side of Equation (4.8) and Equation (4.9) are diffusive parameters those are the different points from the ideal MHD equations such as Equation (3.8) and Equation (3.9), and $\mathbf{R}$ and $\boldsymbol{j}$ in these terms are the viscous stress tensor and current density described in Section 2.2 and calculated by Equation (2.7) and Equation (2.6), respectively. Similarly to Chapter 3, the coordinate system rotates around the central star with Keplerian angular velocity, thus the source terms $\boldsymbol{S}_{\mathrm{Momentum}}$ and S_{Energy} are arose and defined as

$$\boldsymbol{S}_{\mathrm{Momentum}} = 3\Omega^2 \rho x \hat{\boldsymbol{e}_x} - 2\rho \boldsymbol{\Omega} \times \boldsymbol{v}, \tag{4.11}$$

$$S_{\mathrm{Energy}} = 3\Omega^2 \rho x v_x. \tag{4.12}$$

Note that we use the same normalization as described in Section 3.3.1 and 3.3.3, thus the dimensionless normalization parameters, such as $Re_{\mathrm{norm}}, Rm_{\mathrm{norm}}$ and M_{norm} written in Section 2.2, are all 1 and omitted to write in Equation (4.7) to Equation (4.9). And also note that the terms originated by LAD are omitted to write though they are introduced.

Simulation domain is same as Section 3.3.3, that is $(L_x, L_y, L_z) = (2\sqrt{2}, 2\sqrt{2}, \sqrt{2}) = (2H, 2H, H)$. The initial conditions except for diffusion term are also same as Section 3.3.3, those are $\rho_0 = 1,\ p_0 \sim 1.06,\ \boldsymbol{v}_0 = 1.5\Omega x\, \hat{\boldsymbol{e}}_y$, and $\boldsymbol{B}_0 \sim 7.26 \times 10^{-2} \hat{\boldsymbol{e}}_z$. These initial conditions are corresponds to the condition where the maximum growth wavelength of MRI in ideal MHD corresponds to $L_z/3$ and the initial plasma beta is 400. The grid number is set as $N_x \times N_y \times N_z = 128 \times 128 \times 64$ basically, and we also carried out some additional calculation with double resolution such as $N_x \times N_y \times N_z = 256 \times 256 \times 128$ for comparison.

Table 4.1: Models of visco-resistive MHD simulations of MRI-driven turbulence

Model name	Re	Rm	Pm	Resolution	$t_{\rm orbit}$	$\alpha_{\rm ave}$	α_1	α_2
Very low diffusivity								
Re∞-Rm1000-128	∞	1000	0.0	$128\times128\times64$	~ 50	0.070	0.197	0.207
Re2000-Rm1000-128	2000	1000	0.5	$128\times128\times64$	~ 50	0.065	0.197	0.149
Re1000-Rm1000-128	1000	1000	1.0	$128\times128\times64$	~ 50	0.077	0.197	0.204
Re1000-Rm2000-128	1000	2000	2.0	$128\times128\times64$	~ 50	0.069	0.197	0.270
Re1000-Rm∞-128	1000	∞	∞	$128\times128\times64$	~ 50	0.066	0.197	0.167
Low diffusivity								
Re800-Rm400-128	800	400	0.5	$128\times128\times64$	~ 50	0.066	0.197	0.151
Re400-Rm800-128	400	800	2.0	$128\times128\times64$	~ 50	0.069	0.197	0.155
Middle diffusivity								
Re∞-Rm100-128	∞	100	0.0	$128\times128\times64$	~ 50	0.072	0.198	0.183
Re200-Rm100-128	200	100	0.5	$128\times128\times64$	~ 50	0.064	0.200	0.213
Re100-Rm100-128	100	100	1.0	$128\times128\times64$	~ 50	0.071	0.201	0.198
Re100-Rm200-128	100	200	2.0	$128\times128\times64$	~ 50	0.070	0.201	0.159
Re100-Rm∞-128	100	∞	∞	$128\times128\times64$	~ 50	0.074	0.199	0.264
High difusivity								
Re∞-Rm10-128	∞	10	0.0	$128\times128\times64$	~ 50	0.064	0.206	0.168
Re10-Rm10-128	10	10	1.0	$128\times128\times64$	~ 50	0.085	0.264	0.242
Re10-Rm∞-128	10	∞	∞	$128\times128\times64$	~ 50	0.084	0.215	0.207
Very high diffusivity								
Re∞-Rm1-128	∞	1	0.0	$128\times128\times64$	~ 50	0.051	0.466	0.171
Re1-Rm1-128	1	1	1.0	$128\times128\times64$	~ 50	0.146	1.763	0.496
Re1-Rm∞-128	1	∞	∞	$128\times128\times64$	~ 50	0.233	0.869	0.495
High resolution								
Re2000-Rm1000-128	2000	1000	0.5	$256\times256\times128$	~ 25	0.111	0.451	0.261
Re1000-Rm500-128	1000	500	0.5	$256\times256\times128$	~ 25	0.113	0.451	0.285
Re1000-Rm1000-128	1000	1000	1.0	$256\times256\times128$	~ 25	0.129	0.451	0.298
Re1000-Rm2000-256	1000	2000	2.0	$256\times256\times128$	~ 25	0.116	0.451	0.248
Re500-Rm1000-1256	500	1000	2.0	$256\times256\times128$	~ 25	0.108	0.450	0.221

We carried out several calculations of MRI with widely changing the initial Reynolds number for MRI, defined as $Re = \rho_0 v_{A0}^2/\mu\Omega$, and initial magnetic Reynolds number for MRI, defined as $Rm = v_{A0}^2/\eta\Omega$, i.e., similar calculations to chapter 3 but with visco-resistive, resistive-invisid ($Re = \infty$), and nonresistive-viscous ($Rm = \infty$) models. The simulation settings of the calculations are summarized in Table 4.1. The first column shows the name of model. The numbers after Re and Rm represents initial Reynolds number and magnetic Reynolds number respectively, and the final number denotes the number of grids in x-direction that is N_x. The second, third, and fourth columns show initial Reynolds number for MRI: Re, initial magnetic Reynolds number for MRI: Rm, and initial magnetic Prandtl number defined as $Pm = Rm/Re = \nu/\eta$, where

$\nu = \mu/\rho$, respectively. The fifth, sixth columns show the number of grid points and calculated time in orbital periods $t_{\rm orbit}$, respectively. The seventh, eighth, and ninth column shows spatially averaged values of $\alpha \equiv W_{xy}/p_0$ of the temporally averaged value, the value, and an arbitrary chosen peak value in nonlinear phase. The temporally averaged value is calculated by averaging over the range that $10 \sim t_{\rm orbit} \sim 50$. We categorize the models into six groups those are very low diffusivity models, such as $Re, Rm = 1000$ or 2000 (or ∞), low diffusivity models, such as $Re, Rm = 400$ or 800, middle diffusivity models, such as $Re, Rm = 100$ or 200 (or ∞), high diffusivity models, such as $Re, Rm = 10$ (or ∞), very high diffusivity models such as $Re, Rm = 1$(or ∞), and very low diffusivity with high resolution models.

4.4 Simulation results and discussion

4.4.1 Confirmation of the effect of diffusion term on linear growth rate of MRI

In order to verify that the diffusion effects are correctly introduced to the simulation, we compare the time evolution of vertical wavenumber spectra of horizontal velocity in the linear growth phase with theoretically obtained growth rate of MRI in visco-resistive MHD condition. Panel (a) and (b) of Figure 4.4 show time evolution of some wave modes of the z-directional wavenumber spectra of a sum of the radial and the azimuthal velocity averaged over the radial and the azimuthal wavenuber space, i.e., $\left\langle v_h(k_z)^2 \right\rangle_{k_x,k_y} = \left\langle v_x^2(k_z) + v_y^2(k_z) \right\rangle_{k_x,k_y}$, for (a) Re10-Rm10-128 model and (b) Re1-Rm1-128 model, respectively. This figure is a same plot as panel (a) of Figure 4.5 but for the diffusive models and shows only around the first peak. The horizontal axis represents the orbital period $t_{\rm orbit}$, and vertical axis shows $\left\langle v_h(k_z)^2 \right\rangle_{k_x,k_y}$. Red, orange, green, blue, and purple solid lines represent the modes with the wavelength $\lambda_z = L_z, L_z/2, L_z/3, L_z, 4, L_z/5$, respectively, and red, orange, green, and blue dash-dotted lines represent theoretically obtained growth rate of the mode with the wavelength $\lambda_z = L_z, L_z/2, L_z/3, L_z, 4$, respectively. In the condition of $Re = Rm = 10$, the wavelengths of the modes which can be resolved in the simulation domain are $\lambda_z = L_z, L_z/2, L_z/3,$ and $L_z/4$, and the modes of $\lambda_z \leq L_z/5$ are damping mode for the linear growth phase of MRI. Although $\lambda = L_z/4$ mode seems to be affected by nonlinear effects at earlier stage, we can see that the other modes grow with growth rates which almost equal to the

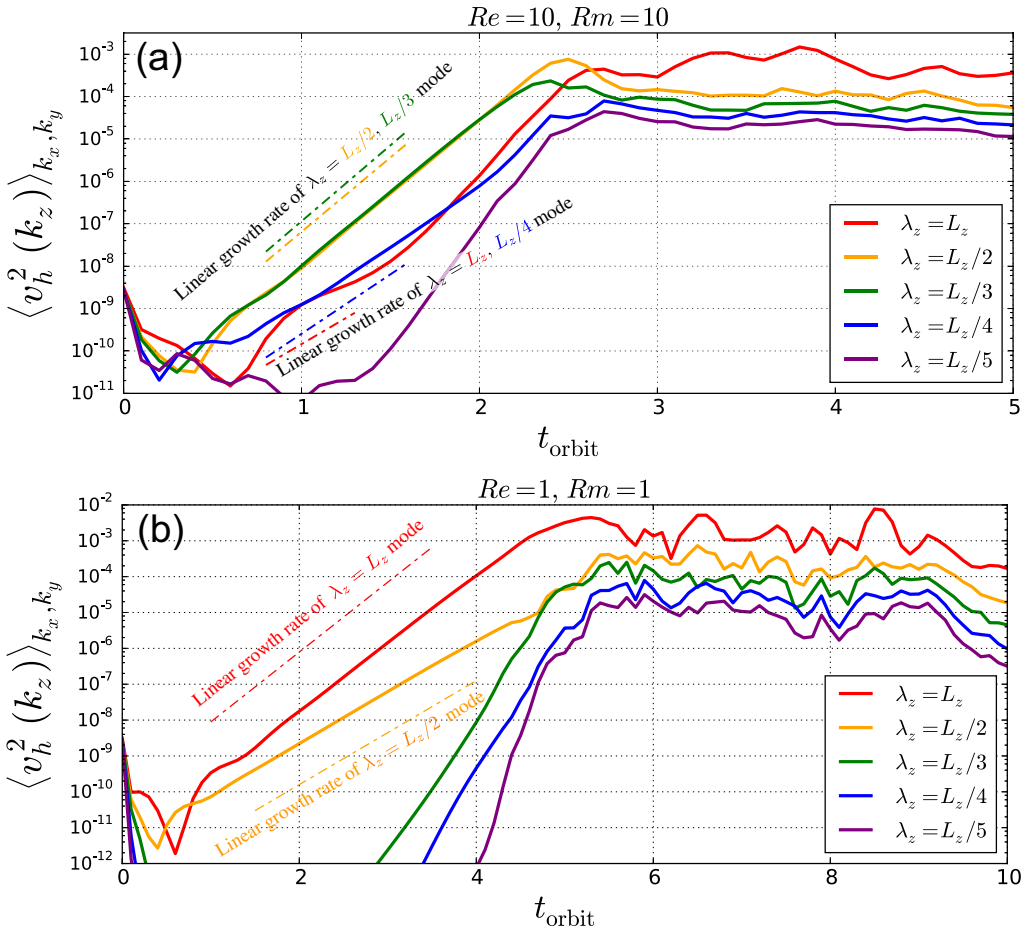

Fig. 4.4: Time evolution of some wave modes of the z-directional wavenumber spectra of a sum of the radial and the azimuthal velocity averaged over the radial and the azimuthal wavenuber space, i.e., $\left\langle v_h(k_z)^2 \right\rangle_{k_x,k_y} = \left\langle v_x^2(k_z) + v_y^2(k_z) \right\rangle_{k_x,k_y}$, for the (a) Re10-Rm10-128 model and (b) Re1-Rm1-128 model. Red, yellow, green, blue, and purple lines represent the modes with wavelength $\lambda_z = L_z, L_z/2, L_z/3, L_z, 4, L_z/5$, respectively, and dash-dotted lines plotted by same clolors represent theoretically obtained growth rate of the mode with each wavelength.

theoretically obtained values. In the condition of $Re = Rm = 1$, the wavelengths of the modes which can be resolved in the simulation domain are $\lambda_z = L_z$ and $L_z/2$, and the modes of $\lambda_z \leq L_z/3$ are damping mode for the linear growth phase of MRI. We can see that the two growth modes grow with growth rates which almost equal to the theoretically obtained values. From these results, it can be confirmed that viscosity and magnetic diffusivity are correctly introduced to our simulation.

4.4.2 Influence of changing diffusion effect on the time evolution of turbulent stress

In this secton, we show the results obtained by the same methods as Section 3.4, and discuss the differences between the results and how such differences are caused by diffusion effects. First, we show the time evolution of spatially averaged turbulent stress defined as Equation 3.14 normalized by the initial pressure p, the similar plotting to panel (b) of Figure 3.3. Figure 4.5 shows the same plot as panel (a) of Figure 3.3 but for some exmple diffusivity models that are (a) Rm1000-Re1000-128, (b) Rm800-Re400-128, (c) Rm400-Rm800-128, (d) Rm100-Re100-128, and (e) Rm10-Re10-128. The horizontal gray dash-dotted lines represent the temporally averaged value of total stress calculated by averaging in the range that $10 \sim t_{\rm orbit} \sim 50$. In this section, we focus on peaks at the first saturation of the turbulent stress (first peak; left gray vertical dashed lines) and at the saturation time where the turbulent stress takes maximum value in range of $20 \sim t_{\rm orbit} \sim 40$ (nonlinear peak; right gray vertical dashed lines). The first peaks of results in Figure 4.5 are almost at same orbital time that is $t_{\rm orbit} = 2.2$ except for the high-diffusivity model Re10-Rm10-128. In addition, though Re100-Rm100-128 model takes slightly higher value, the saturation levels of first peak are also almost same values except for the model Re10-Rm10-128. This indicates that the saturation mechanisms of very low and low diffusivity models are hardly modified still small diffusivities might change the small-scale flow and magentic field structure, and the modification of small scale flow in Re100-Rm100-128 model might be little more effective than others. We discuss the detailed mechanism of first peak in these models later. The difference between the high-diffusivity model Re10-Rm10-128 and others at the first peak can be explained by previous analytical studies. As reported by Pessah & Chan (2008) and also shown in Figure 4.3, the linear growth rate of MRI in $Re = Rm = 10$ condition are rather modified than $Re, Rm \leq 100$, and thus the fastest growth rate of the reproducible mode in the simulation domain, in this case $L_z/3$, takes much smaller value than that in other low diffusivity cases. Therefore, the amplification of turbulent stress are delayed. In addition, as described in Section 4.1, Pessah & Goodman (2009) and Pessah (2010) analytically showed that the turbulent stress at the time that linear growth rate of parasitic instability reaches that of MRI becomes larger value in the case that $Re = 10,$ and $Rm = 10$ (see figure 3 and figure 4 of Pessah, 2010). Although the results of our ideal

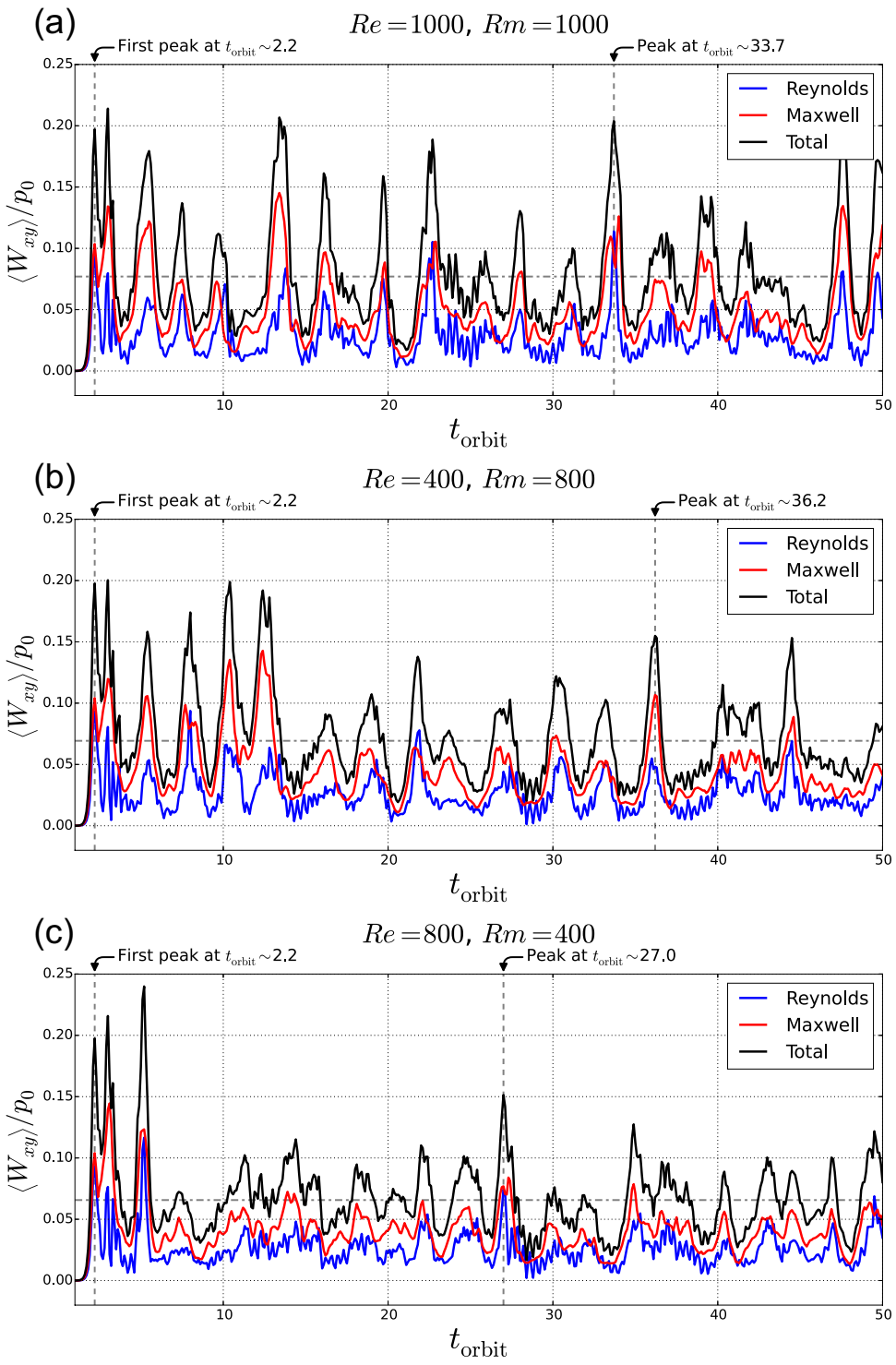

Fig. 4.5: Time evolution of spatilly averaged normalizd turbulent stress (i.e., same plot as panel (a) of Figure 3.3) with some diffusivity model that are (a) Rm1000-Re1000-128, (b) Rm800-Re400-128, (c) Rm400-Rm800-128, (d) Rm100-Re100-128, and (e) Rm10-Re10-128. Red, Blue, and black lines show Reynold, Maxwell, and total stress respectively. The hoizontal gray dash-dotted line represents the temporally averaged value of total stress. The left and right gray vertical dashed lines represents times at first and nonlinear peaks.

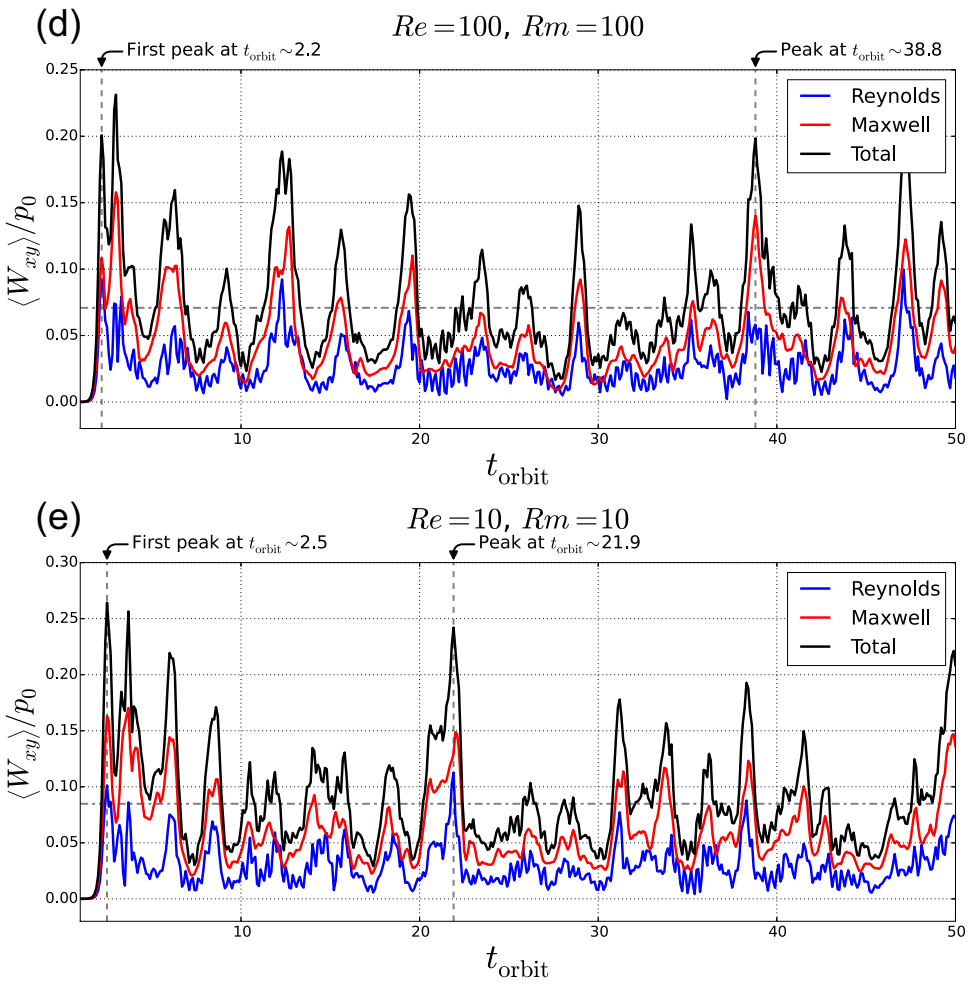

Fig. 4.5: (Continued)

calculation shown in chapter 3 showed that the actual saturation time should not be determined simply by the linearly obtained condition that $\omega_{\rm PI,max} = \omega_{\rm MRI,max}$ but be determined by more complicated interaction of vortices, the condition is good indicator to know time that parasitic instability are efficiently collapsed the flow structure. Pessah & Goodman (2009) and Pessah (2010) indicates that this feature is caused by the viscosity quenching the Kelvin-Helmholtz instability. Actually, the values of first peak with high viscosity models (see eighth column of table 4.1) take relatively larger value in our simulation. On the other hand, the time evolution of stress in non-linear phase are modified by changing the diffusivities. Although the temporally averaged values of stress are similar value, the peak values in nonlinear phase are different and its trend of the averaged values and peak values seems not simple.

4.4.3 Trends of the temporally averaged, first peak, and nonlinear peak values in Re and Rm space

To see the trend of stress of temporally averaged value, at first peak, and at nonlinear peak, we investigate these values of models except the high resolution calculations in Re_0 and Rm_0 space. Figure 4.6 shows (a) the temporally averaged stress values, (b) stress values at first peak, and (c) stress values at each nonlinear peak in Re_0 and Rm_0 space, i.e., these plots are summary of seventh, eighth, and ninth column of table 4.1. The horizontal and vertical axes denotes Re_0 and Rm_0, respectively, and colors of circle represent the stress value. We can obtain the trend from the distribution of temporally averaged stress (panel (a)) that the strong viscosity increases the temporally averaged stress value, and the strong magnetic diffusivity decreases that. The stress values at first peak (panel (b)) show the trend that the strong viscosity increases the value at first peak as describe above and the strong magnetic diffusivity also increases that a little. And the stress values at nonlinear peak (panel (c)) show the viscosity increase the value at nonlinear peak. From these trend, we obtain the effects of strong diffusivities; the strong viscosity increases the peak value at not only first peak but also peaks in nonlinear phase, and the strong magnetic diffusivity increases the value only at first peak and does not affect (or decreases) the nonlinear peaks. These facts indicate that the quenching K-H instability by the strong viscosity remains to be effective at peaks in nonlinear phase, and the strong magnetic diffusivity are not effective to determine the peak of stress except for the first peak.

In the range of $Re_0 \geq 100$ and $Rm \geq 100$ of all panels of Figure 4.6, there are no obvious enhancement of the stress values by changing Re and Rm like high and very high diffusivity models. Figure 4.7 is the same plot as Figure 4.6 but its plotting range is set to $Re \geq 100$ and $R \geq 100$. From panel (b) of Figure 4.7, there is a similar trend to the strong diffusivity cases, i.e., the diffusion effect make the value at the first peak large. The linear analysis of MRI and parasitic instability showed that the properties of linear growth are almost not different in $Re \geq 100$ and $Rm \geq 100$ region. Therefore, this variation is not caused by the difference of linear properties but should be due to generation and modification of small-scale flow around the transition to the nonlinear state, as explained in chapter 3.

The temporally averaged value (panel (a)) and the value at nonlinear peak (panel (c)) seem not to have obvious trend while the values itself are slightly different.

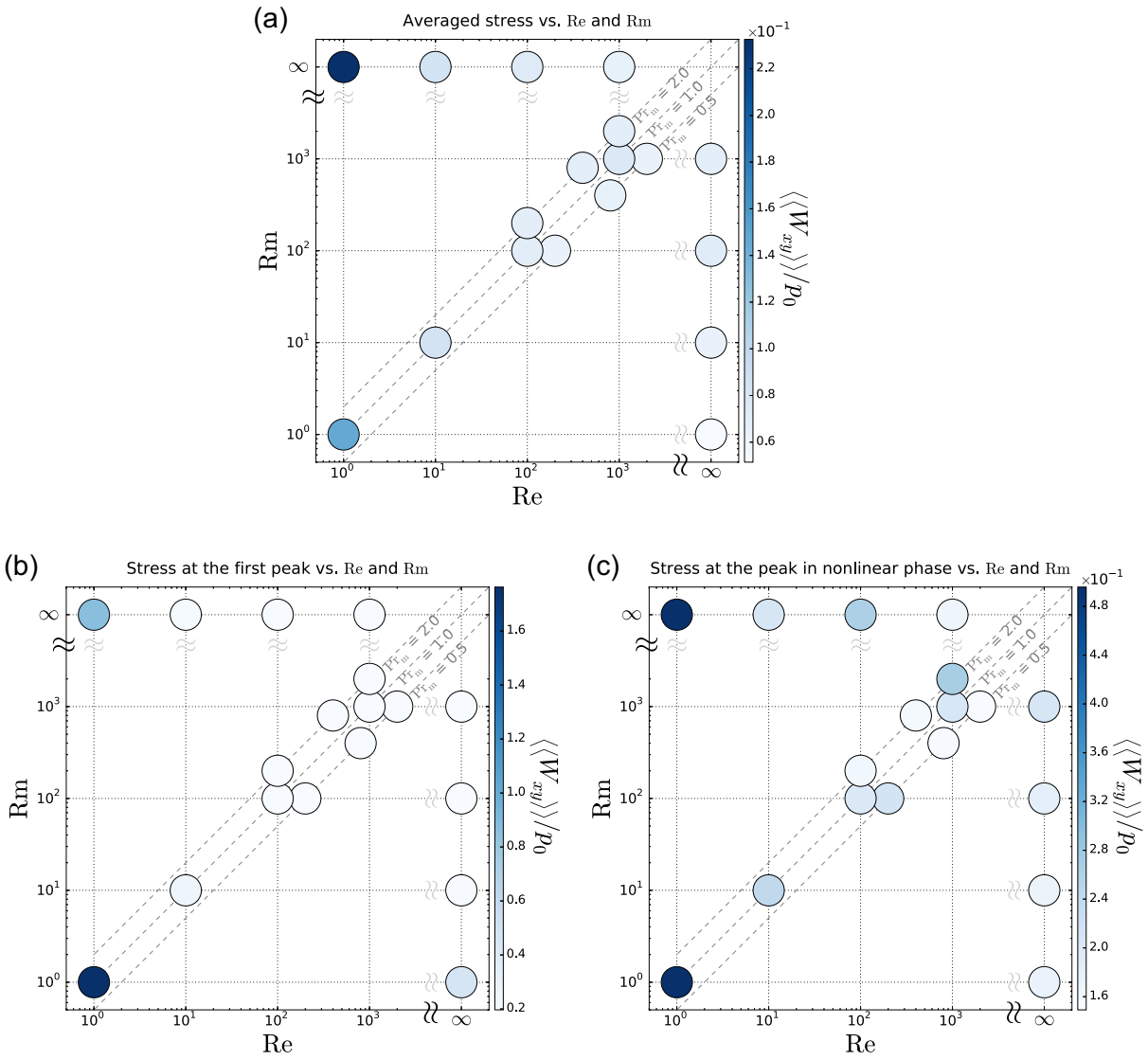

Fig. 4.6: (a) Temporally averaged stress, (b) stress values at first peak, and (c) stress values at nonlinear peak of each calculation in *Re* and *Rm* space.

In particular, the fact that the temporally averaged value does not have a trend is different feature from the previous numerical studies such as Lesur & Longaretti (2007) and Fromang et al. (2007). To see the difference between our study and Lesur & Longaretti (2007), we check the initial magnetic Prandtl number dependence of the peaks and averaged values. Figure 4.8 shows the Prandtl number dependence of the temporally averaged, first peak, and nonlinear peak values. The circle, rhombus, and cross markers denote the very low diffusivity models, low diffusivity models, and middle diffusivity models, respectively, and red, blue, and

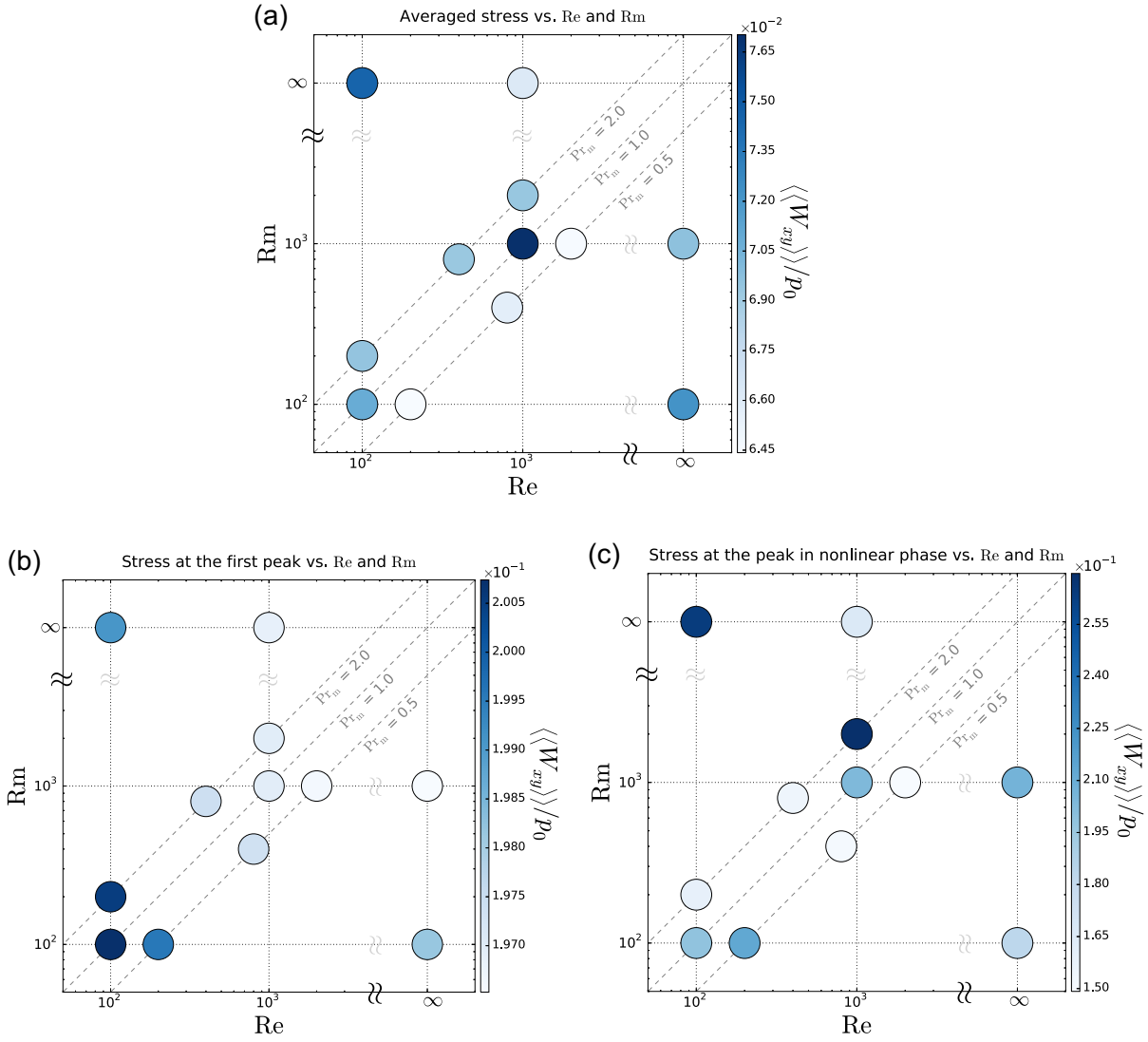

Fig. 4.7: Same as Figure 4.6 but in range of $Re_0 \geq 100$ and $Rm \geq 100$

green marker colors represent the values of first peak, nonlinear peak, and temporally averaged value, respectively. Lesur & Longaretti (2007) reported that the temporally averaged stress has a positive correlation with the Plandtl number, i.e., $\alpha = \langle\langle W_x y \rangle\rangle / p_0 = Pm^{0.25\sim0.5}$, by their numerical simulation. Figure 4.8 shows, however, the temporary averaged stress does not have the prandtl number dependence though the nonlinear peaks in very low diffusivity models slightly have positive correlation. What makes different result between their results and ours? One possible reason is the difference of aspect ratio of box size. We use the aspect ratio of simulation box which is $L_x : L_y : L_z = 2 : 2 : 1$ to resolve most unstable parasitic mode, whereas Lesur & Longaretti (2007) uses aspect ratio

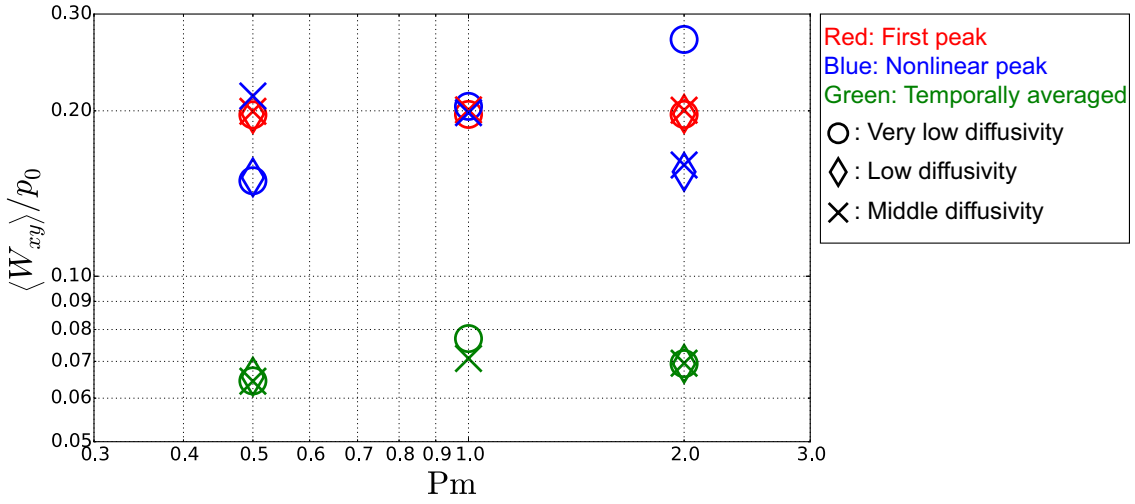

Fig. 4.8: Magnetic Prandtl number Pm dependence of the temporally averaged, first peak, and nonlinear peak values. The circle, rhombus, and cross markers denote the very low diffusivity models, low diffusivity models, and middle diffusivity models, respectively, and red, blue, and green marker colors represent the values of first peak, nonlinear peak, and temporally averaged value, respectively.

which is $L_x : L_y : L_z = 1 : 4 : 1$. Bodo et al. (2008) reported that the saturation value of the turbulent stress decreases when the aspect ratio $L_x : L_z$ varies 1 to 4. Pessah & Goodman (2009) reported this tendency depends of whether the fastest parasitic mode, i.e., $\boldsymbol{k}_{\mathrm{PI,max}} \sim 0.59 k_{\mathrm{MRI,max}} \hat{\boldsymbol{e}}_{k_x = k_y}$, is resolved or not in respective simulation box. When the fastest growth parasitic mode can be enough resolved (i.e., the box is enough large), there is almost no Prandtl number dependency, but when using the aspect ratio that $L_x : L_y : L_z = 1 : 4 : 1$, the Prandtl number dependency appears because the fastest growth mode of parasitic instability induced by restructured channel flow can not be resolved (see figure 2 of Pessah & Goodman, 2009). The aspect ratio of our calculation is set as $L_x : L_y : L_z = 2 : 2 : 1$ and thus our simulation can resolve the fastest growth parasitic mode induced by restructured channel flow, and thus, it might be natural result that our simulation results don't have dependence of magnetic Prandtl number.

4.4.4 Contribution of the diffusion effects for the saturation mechanism of MRI: first peak

From Figure 4.7, there was no significant trend in the spatially averaged turbulent stress by changing the diffusivity in the range that $Re, Rm \geq 100$. This fact

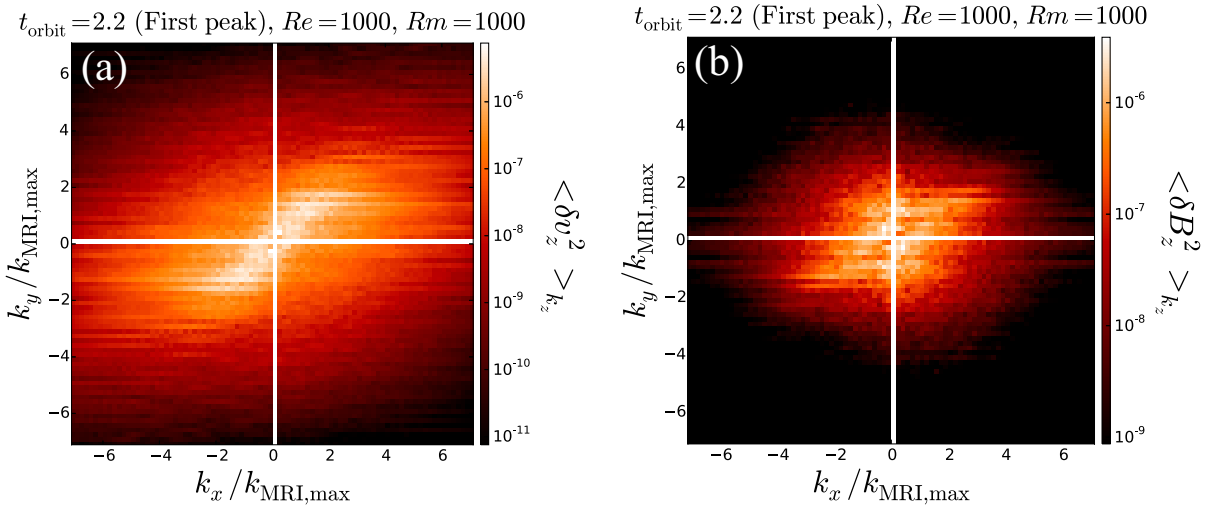

Fig. 4.9: Wavenumber spectra of (a) δv_z and (b) δB_z in the horizontal wavenumber plane averaged over vertical wavenumber direction (same as Figure 3.6) at the times of first peak in Re1000-Rm1000-128 model.

indicates the modified small scale flow structure does not affect to the collapse mechanism of initial and restructured channel flow effectively. On the other hand, Figure 4.5 shows the time evolution of stress surely modified by the small amount of diffusivity though the peak and mean values do not change much. In this section, we focus on the first peak of several calculations, and investigate how the small scale flow structures are modified. To determine these, we apply the same analytical method as chapter 3 to the visco-resistive simulation results. First, we apply the two-dimensional Fourier-transform to the vertical velocity and vertical disturbed magnetic field. As described in Section 3.4.2, the enhancement of vertical disturbed velocity δv_z and vertical disturbed magnetic field δB_z are related to the Kelvin-Helmholtz instability and magnetic reconnection, and thus the direction of their enhancement in horizontal (i.e., radial and azimuthal) wavenumber plane indicate which phenomena is occurring. Figure 4.9, Figure 4.10, and Figure 4.11 show wavenumber spectra of (a) δv_z and (b) δB_z in the horizontal wavenumber plane averaged over vertical wavenumber direction at the times of first peak obtained by Re1000-Rm1000-128, Re100-Rm100-128, and Re10-Rm10-128. Horizontal and vertical axes are the radial wavenumber k_x and azimuthal wavenumber k_y normalized by the maximum growth wavenumber of MRI in ideal MHD condition, and color contour represents wavenumber spectra of v_z averaged over the vertical wavenumber space. Comparing panel (a) in Figure 4.9, Figure 4.10, and

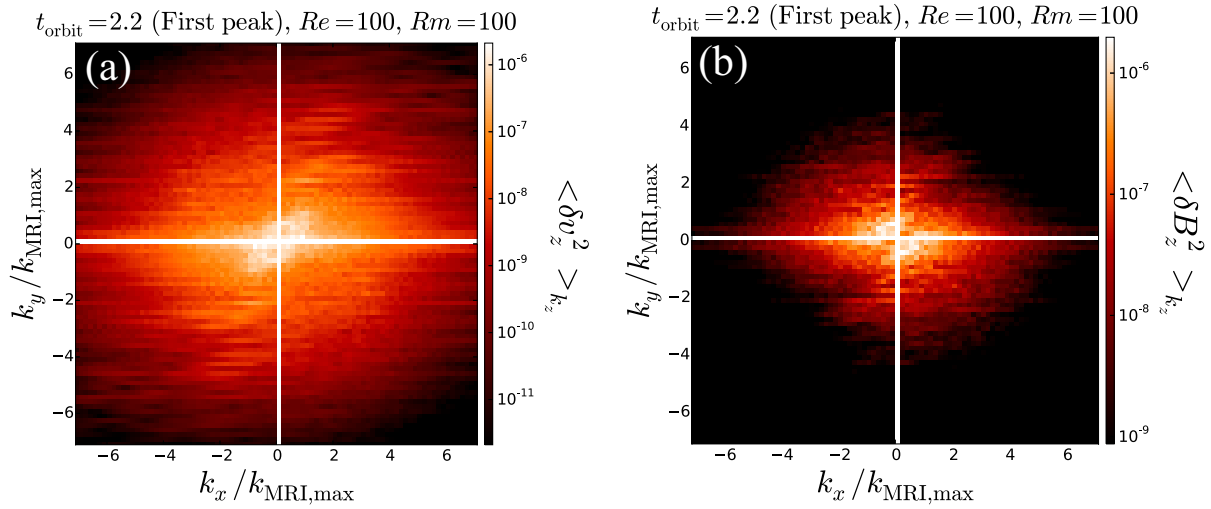

Fig. 4.10: Same as Figure 4.9 but for Re100-Rm100-128 model.

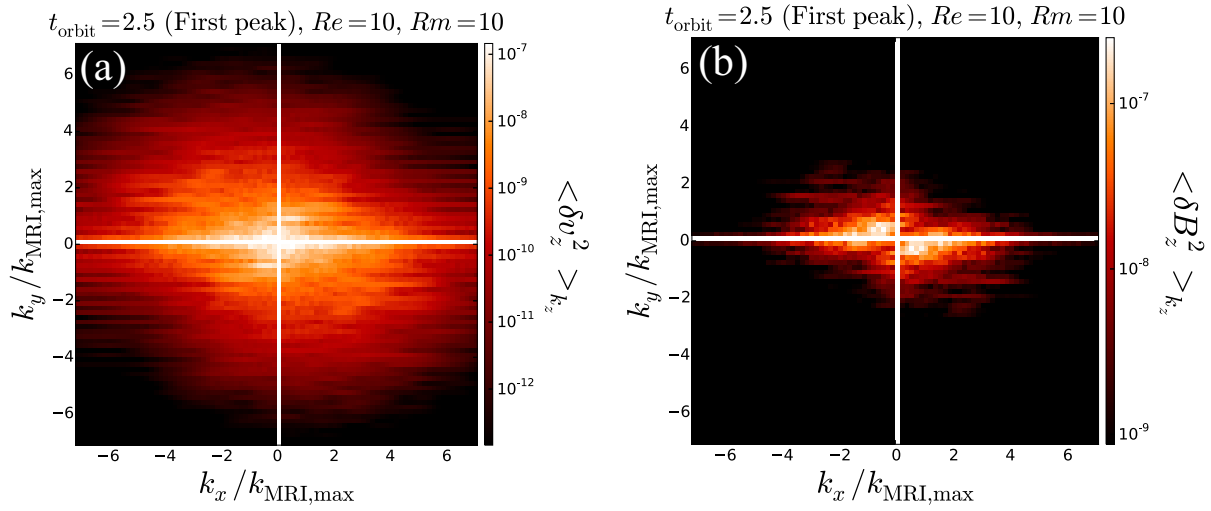

Fig. 4.11: Same as Figure 4.9 but for Re10-Rm10-128 model.

Figure 4.11, the enhancement of 45 degrees waves induced by shear flow is modified by changing the diffusivity models. Panel (a) of Figure 4.10 shows that the anisotropic wave enhancement in Re100-Rm100-128 model is occurred only in lower wavenumber region than that in Re1000-Rm1000-128 model and the spectra in high wavenumber region is more isotropic than that of Re1000-Rm1000-128 model. In addition, panel (a) of Figure 4.11 shows that the anisotropy in the direction of 45 degrees disappears and it seems that there is slight anisotropy in the direction

of 135 degrees. From these results, it can be seen that the anisotropic wave enhancement of v_z becomes weak as the diffusivity is increased. As shown in panel (b) of Figure 4.3, all the direction of velocity shear created by maximum growth mode of MRI in these three models are approximately 45 degrees, thus, this modification is considered to indicate that the dominant mode of parasitic instability changes from Kelvin-Helmholtz mode to magnetic-reconnection mode by increasing magnetic diffusivity. In fact, panel (b) in Figure 4.10, and Figure 4.11 show that vertical magnetic field seems to be enhanced with around 135 degrees direction, i.e., the direction of antiparallel magnetic field, and these spectra of δB_z indicates the evolving magnetic reconnection by increasing magnetic diffusivity. Threfore, the anisotropies of wavenumber spectra of Re100-Rm100-128 model, that the direction of v_z is 45 degrees and that of B_z is 135 degrees, indicate the Kelvin-Helmholts mode and magnetic reconnection mode parasitic instabilty is occured comparably. The anisotropies of wavenumber spectra of Re10-Rm10-128 model, that the direction of v_z is roughly 135 degrees and that of B_z is also 135 degrees, indicate the magnetic reconnection mode overtakes the Kelvin-Helmholtz mode at the first peak.

Comparing the anisotropic wave region in panel (a) in Figures 4.9, 4.10, and 4.11, the fastest growth wavenumber is also modified from the large wavenumber region to small wavenumber region by increasing diffusivities. The spectra of v_z in Re1000-Rm1000-128 model is similar to the result of ideal calculation shown in Figure 3.6, i.e., there is the fastest growth wave around $(k_x/k_{\rm MRI}, k_y/k_{\rm MRI}) = (2, 2)$. On the other hand, the fastest growth wave are located in a region closer to the origin in Re100-Rm100-128 model. To determine the fastest growth mode and its difference between these three models, we investigate the time evolution of spectra of v_z along $k_x = k_y$ in the same way as Section 3.4.2. Figure 4.12 shows the time evolution of wavenumber spectra of v_z along $k_x = k_y$ line averaged over the vertical wavenumber space in (a) Re1000-Rm1000-128 model, (b) Re100-Rm100-128 model, and (c) Re10-Rm10-128 model around the time of first peak. The horizontal axis is the horizontal wavenumber $k_h \equiv \sqrt{k_x^2 + k_y^2} = \sqrt{2}k_x$ normalized by the MRI maximum growth wave number. Line colors, from cold color to hot colors, represent the time elapsed. The dotted line at $k_h/k_{\rm MRI,max} = 0.59$ represents analytically obtained maximum growth wavenumber of K-H mode parasitic instability in the ideal MHD condition. It can be confirmed that the Re10-Rm10-128 model has the different slope of the energy cascade due to its high diffusivity effects, and Re1000-Rm1000-128 and Re100-Rm100-128 take the different time evolution of wavenum-

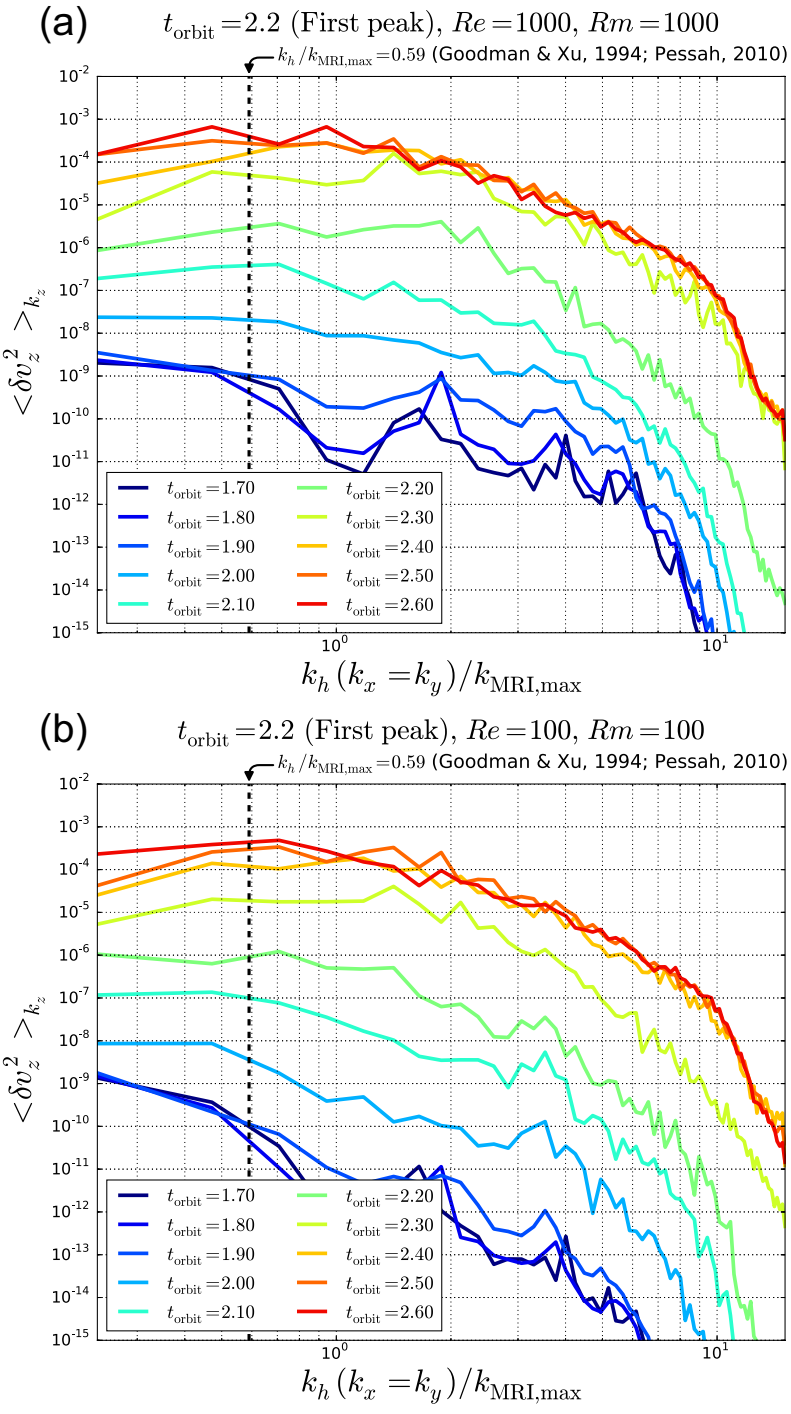

Fig. 4.12: Time evolution of wavenumber spectra of v_z along $k_x = k_y$ line averaged over the vertical wavenumber space in (a) Re1000-Rm1000-128 model, (b) Re100-Rm100-128 model, and (c) Re10-Rm10-128 model

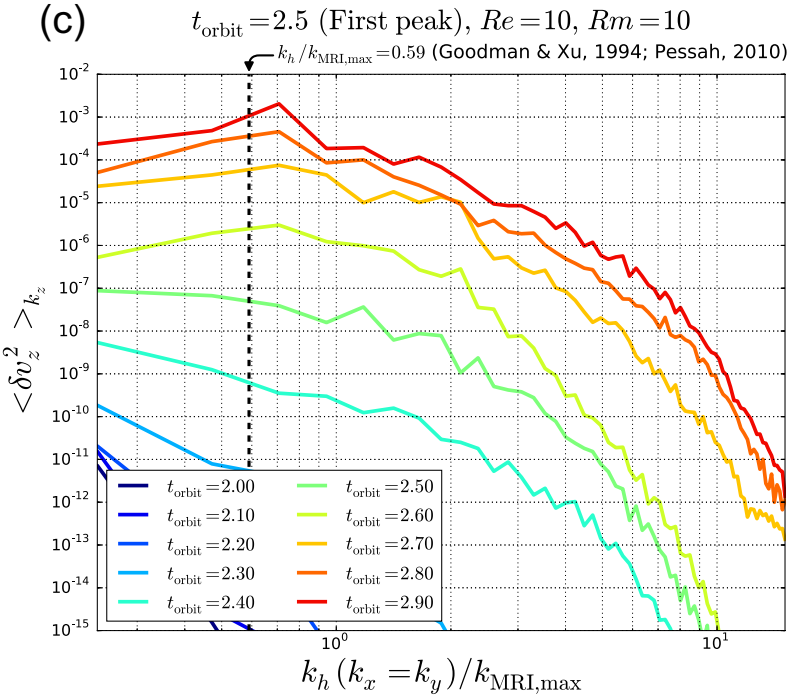

Fig. 4.12: (Continued)

ber spectrum toward the first peak though the linear properties are almost same between these two models. The fastest growth wavenumber in Re1000-Rm1000-128 model around the first peak shown in panel (a) is $k_h/k_{\rm MRI} = 1 \sim 2$. Although this value is slightly smaller than the value in the ideal simulation (Figure 3.7), the feature, that the fastest growth wavenumber is larger than the fastest growth wavenumber of parasitic instability, is similar to the ideal one. Comparing the results of Figure 4.12, we can confirm that this feature disappears when the diffusivities increase and the wavenumber nearer the theoretically obtained value which is $k_h/k_{\rm MRI} = 0.59$ has the energy dominantly. Therefore, in addition to the modification of the anisotropy due to changing the magnetic diffusivity, differences in the calculated models are also attributable to the modification of small-scale flow structure due to the viscosity.

To see how the flow structure modified by diffusivities, we investigate the shear flow structure in the 45 degree surface at the time of first peak in the same in the same way as Section 3.4.2. Figure 4.13 shows the structures of the parallel component of disturbed horizontal velocity $\delta v_{h,\parallel}$ in a surface with horizontal direction $h_{x=y}$ along the direction of $\hat{\boldsymbol{e}}_{x=y} \equiv (\hat{\boldsymbol{e}}_x + \hat{\boldsymbol{e}}_y)/\sqrt{2}$ and vertical direction z in (a) Re1000-Rm1000-128 model, (b) Re100-Rm100-128 model, and (c) Re10-Rm10-128

model at the time of first peak. The parallel component of disturbed horizontal velocity is defined as

$$\delta v_{h,\parallel} \equiv \delta v_x \cos(\pi/4) + \delta v_y \sin(\pi/4). \tag{4.13}$$

In the panel (a) of Figure 4.13, we can find the small-scale and winding flow structure at around $(h, z) = (0.4H, 0.15H)$ and $(-0.8H, 0.3H)$. These structures are similar to the small-scale and jet-like structure observed in the ideal simulation shown in Figure 3.8, and thus, the fastest growth wave shown in panel (a) of Figure 4.12, whose wavenumber is larger than maximum growth wavenumber of K-H mode parasitic instability, is considered to reflect this small-scale and winding flow structure. Comparing these structures with Re100-Rm100-128 model, although almost all structure of Re100-Rm100-128 model (panel (b)) are much similar to that of Re1000-Rm1000-128 model, the small scale structures are modified and those in Re100-Rm100-128 model become smooth due to the diffusion effects. In these two models, both the created small-scale flow are torn up and layered structures are collapsed into vortices similarly to the ideal case (Figure 4.13). The structures created in these processes are also different in two models, i.e., the generated structure in Re1000-Rm1000-128 model is much 'dirty' than that in Re100-Rm100-128 model. The flow structure in Re10-Rm10-128 model is much modified and smoothed by the diffusion effect than other two models. The small-scale structure is not effectively created and thus the tearing up the layered flow is not occurred. The layered flow is broken by rolling up of the large-scale vortices, which seems to be evolved by K-H mode parasitic instability.

From above results and discussions, the efficiencies of small amount of diffusion effects for the first peak are summarized as follows. The magnetic diffusivity changes a balance of K-H mode and magnetic reconnection mode parasitic instability, thus it controls the direction of the anisotropic wave enhancement. In our calculation, 45 degrees directional anisotropic wave enhancement of v_z decreases and 135 degrees directional anisotropic wave enhancement of B_z increases when the diffusivity model changes from the very low diffusivity model (Re1000-Rm1000-128; Figure 4.9) to middle diffusivity model (Re100-Rm100-128; Figure 4.10). On the other hand, shear viscosity changes the flow structure at the saturation, thus it controls the collapse process via the K-H mode parasitic instability. In our calculation, the small-scale structure and its tearing observed in ideal calculation are also reproduced in very-low diffusivity (panel (a) of Figure 4.9) and low-diffusivity

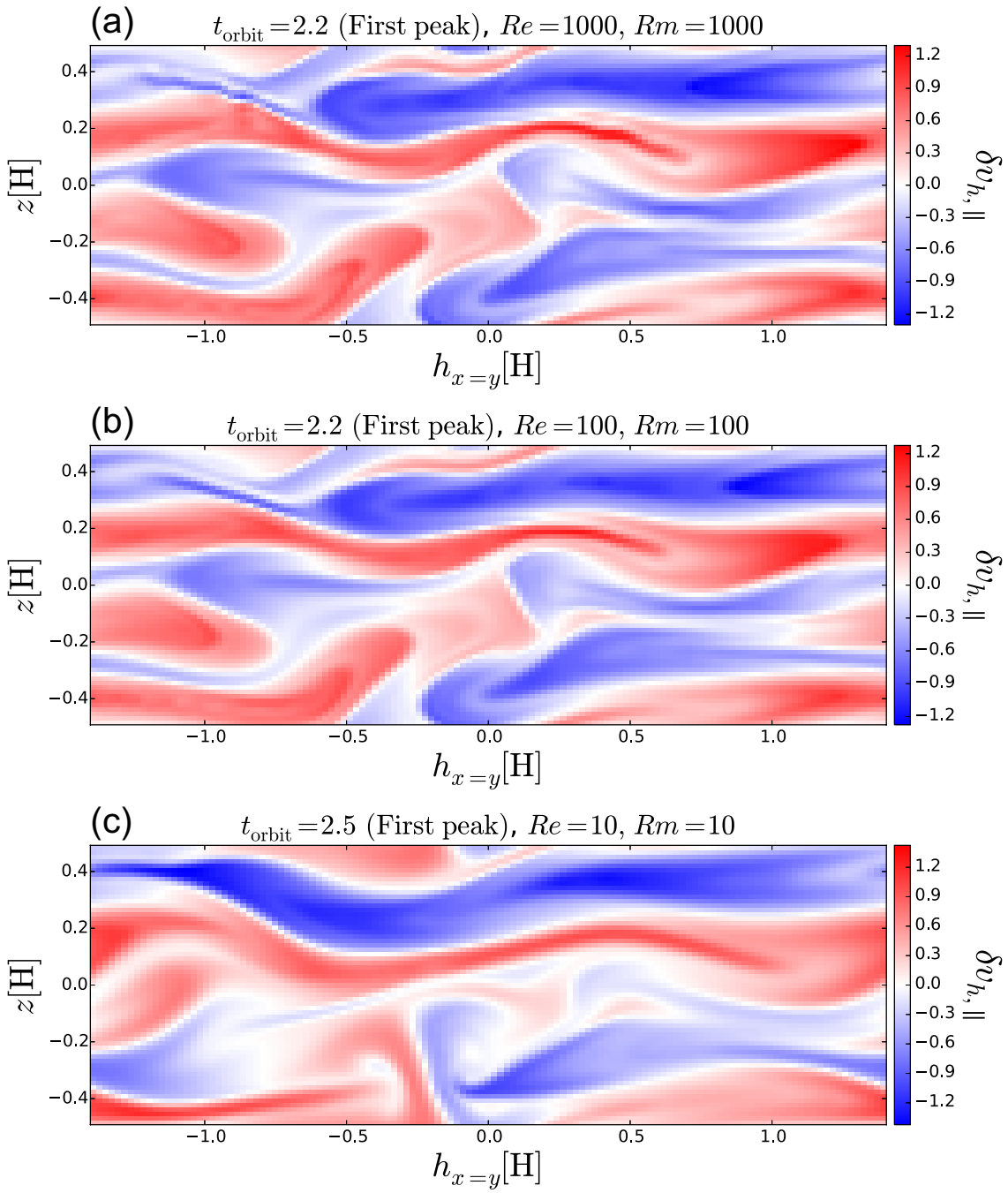

Fig. 4.13: Structures of the parallel component of disturbed horizontal velocity $\delta v_{h,\parallel}$ in a surface with horizontal direction $h_{x=y}$ along the direction of $\hat{\boldsymbol{e}}_{x=y} \equiv (\hat{\boldsymbol{e}}_x + \hat{\boldsymbol{e}}_y)/\sqrt{2}$ and vertical direction z in (a) Re1000-Rm1000-128 model, (b) Re100-Rm100-128 model, and (c) Re10-Rm10-128 model at the time of first peak

models (panel (b) of Figure 4.10). The collapse process of this small-scale flow is slightly different between two models due to the smoothing effect of viscosity, and thus this difference results in the modification of the fastest growth wavenumber (panel (a) and panel (b) of Figure 4.12). In addition, the calculation of higher viscosity model (Re10-Rm10-128) shows the delay of saturation and collapse of layered flow not by the tearing of small scale flow but by the large scale roll up. These are caused by quenching of K-H instability reported by Pessah & Goodman (2009) and effect of smoothing structure by viscosity, and result in the maximum growth wavenumber becomes comparable to the theoretically obtained maximum growth wavenumber of parasitic instability.

4.4.5 Contribution of the diffusion effects for the saturation mechanism of MRI: nonlinear peak

Finally, we investigate the contribution of the diffusion effects for the saturation mechanism of the turbulent stress at the nonlinear peak. As describe in Section 4.4.2, we choose a peak in the turbulent state whose value of stress takes maximum value in range of $20 \sim t_{\rm orbit} \sim 40$, and call this peak nonlinear peak. In Section 4.4.3, we show that the values of nonlinear peak don't have any obvious trend in Re and Rm space. On the other hand, the time evolution of stress shown in Section 4.4.2 is surely modified by the small amount of diffusivities. Therefore, although it does not appear as a temporally and spatially averaged value, a small amount of diffusion effects should have some influence to the flow pattern and wavenumber spectra. In this section, we investigate the difference of the property of spatial structure at the nonlinear peaks of several diffusivity models by using the same method of Section 4.4.4. Figures 4.14, 4.15, and 4.16 is same plot as Figures 4.9, 4.10, and 4.11, respectively, but at the time of each nonlinear peak.

Comparing panel (a) of Figures 4.9, 4.10, and 4.11, the 45 degrees wave are enhanced in all diffusivity models. The enhancement regions are located at the smaller wavenumber region than that at the first peak These are similar result to that of ideal simulation shown as Figure 3.10 in chapter 3. Although the anisotropic enhancement of v_z in Re1000-Rm1000-128 model has slightly sharper directivity than that in other two models, there are little difference between three models compared to that at the first peak. In addition, comparing panel (b), the disturbed vertical magnetic field B_z also has the 45 degrees anisotropic wave enhancement in all of three cases. Though the differences in the structure of the wavenumber

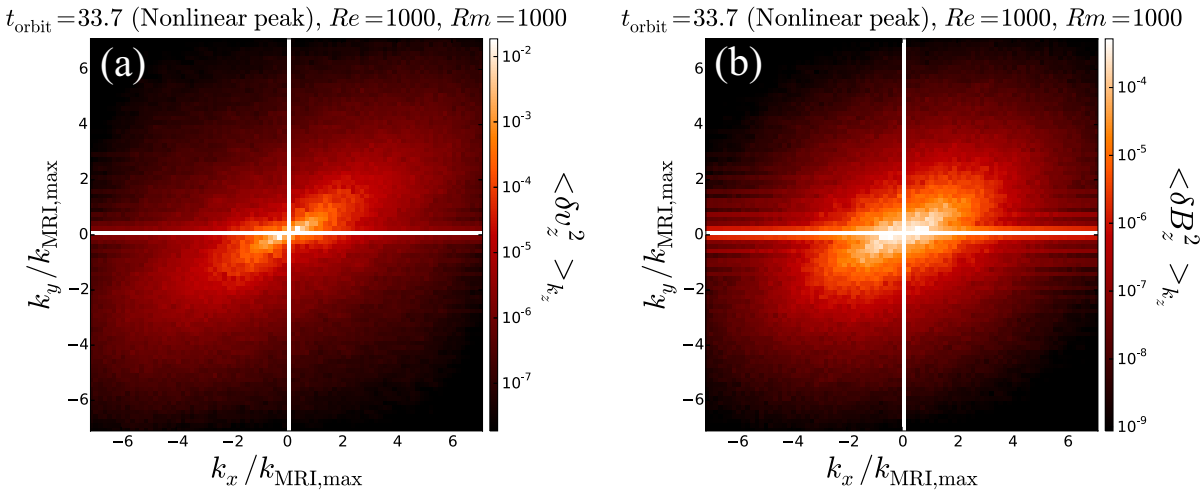

Fig. 4.14: same as Figure 4.9 but at the time of nonlinear peak

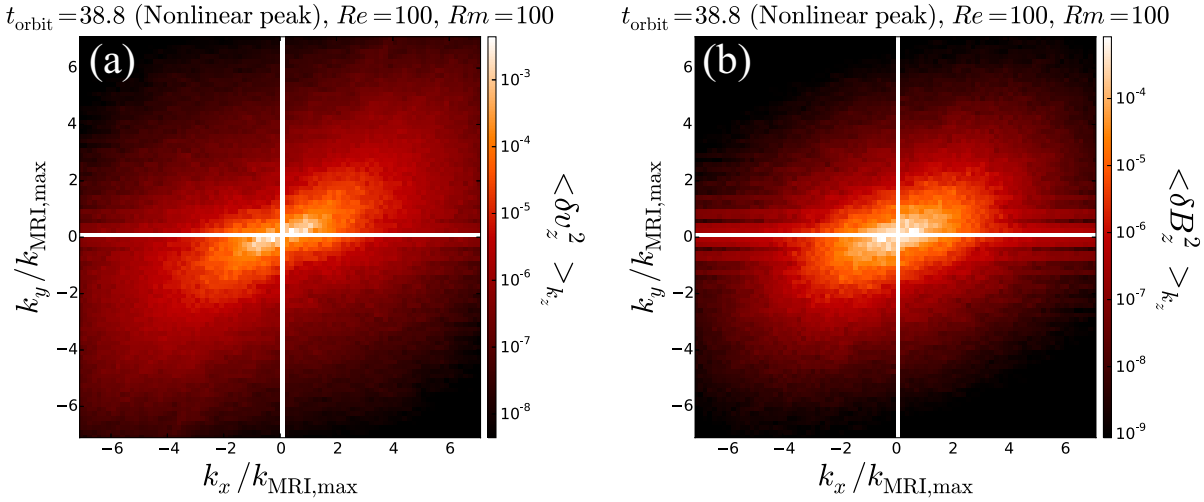

Fig. 4.15: Same as Figure 4.10 but at the time of nonlinear peak

spectra are observed depending on the diffusion at the first peak, the 45 degrees wave enhancements are observed in all the spectra of v_z and B_z, i.e., the collapse of restructured shear flow is caused by K-H instability regardless of diffusivity effects. To see the detail of phenomena occurring at the nonlinear peak, we investigate the flow pattern along the 45 degrees direction plane like Section 4.13. Figure 4.17 is a same plot as Figure 4.13 but at the time of nonlinear peaks. In all three diffusion models, there are restructured channel flow structures whose wavelength is

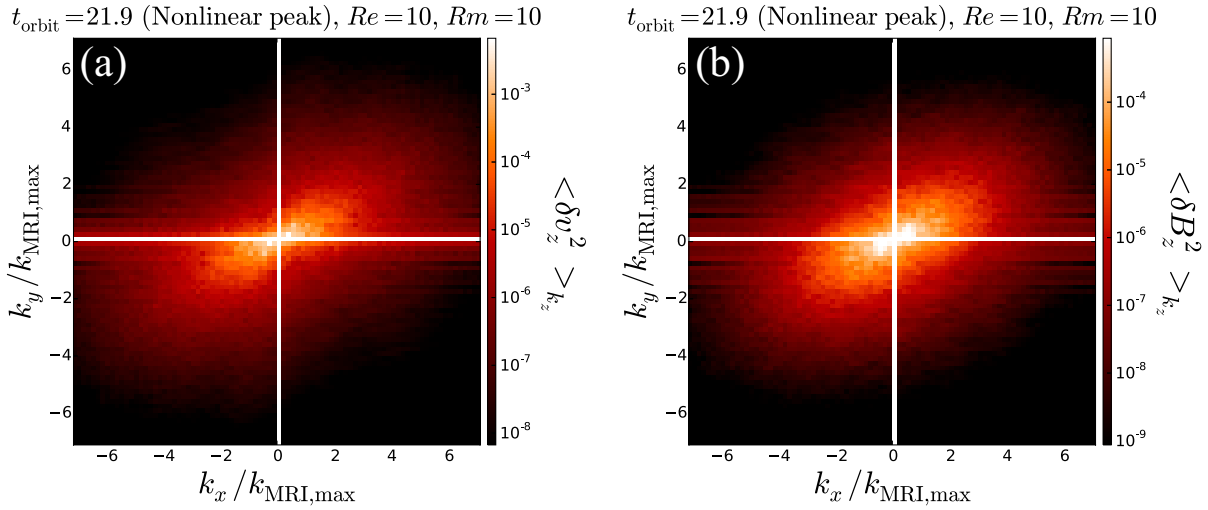

Fig. 4.16: Same as Figure 4.11 but at the time of nonlinear peak

$\lambda_z = L_z$. As mentioned in Section 3.4.3, this structure is caused by enhancement of B_z and modification of the maximum growth wavelength of MRI. The nonlinear peak is created by collapse of these restructured flow structure. The restructured channel flow in Re10-Rm10-128 model has much smoother structure than other two peaks, and those in Re1000-Rm1000-128 model and Re100-Rm100-128 model contains a lot of small-scale flow structure. The large-scale flow in lower diffusivity models seems to be collapsed from the inside due to the existence of fine structure flow. On the other hand, the large scale flow in middle diffusivity model seems to be collapsed not by the mixing of small-scale flow but by the large-scale vortices. Although it is difficult to reveal the detailed collapse mechanism because the collapse is occurred in the turbulent state, the flow structure around the nonlinear peak is different in the three models. The spatially average turbulent stress at the nonlinear peak is, however, not so different in three models. This fact indicates a possibility that the diffusivities do not affected to determine the peak value in nonlinear phase when the diffusivities are in range that $Re > 10$, $Rm > 10$ though the diffusivities modify flow structures.

4.5 Concluding remarks

In this chapter, we investigate the physical diffusion effects to the turbulent stress and peak creation mechanism. Previous studies reported that small amount of

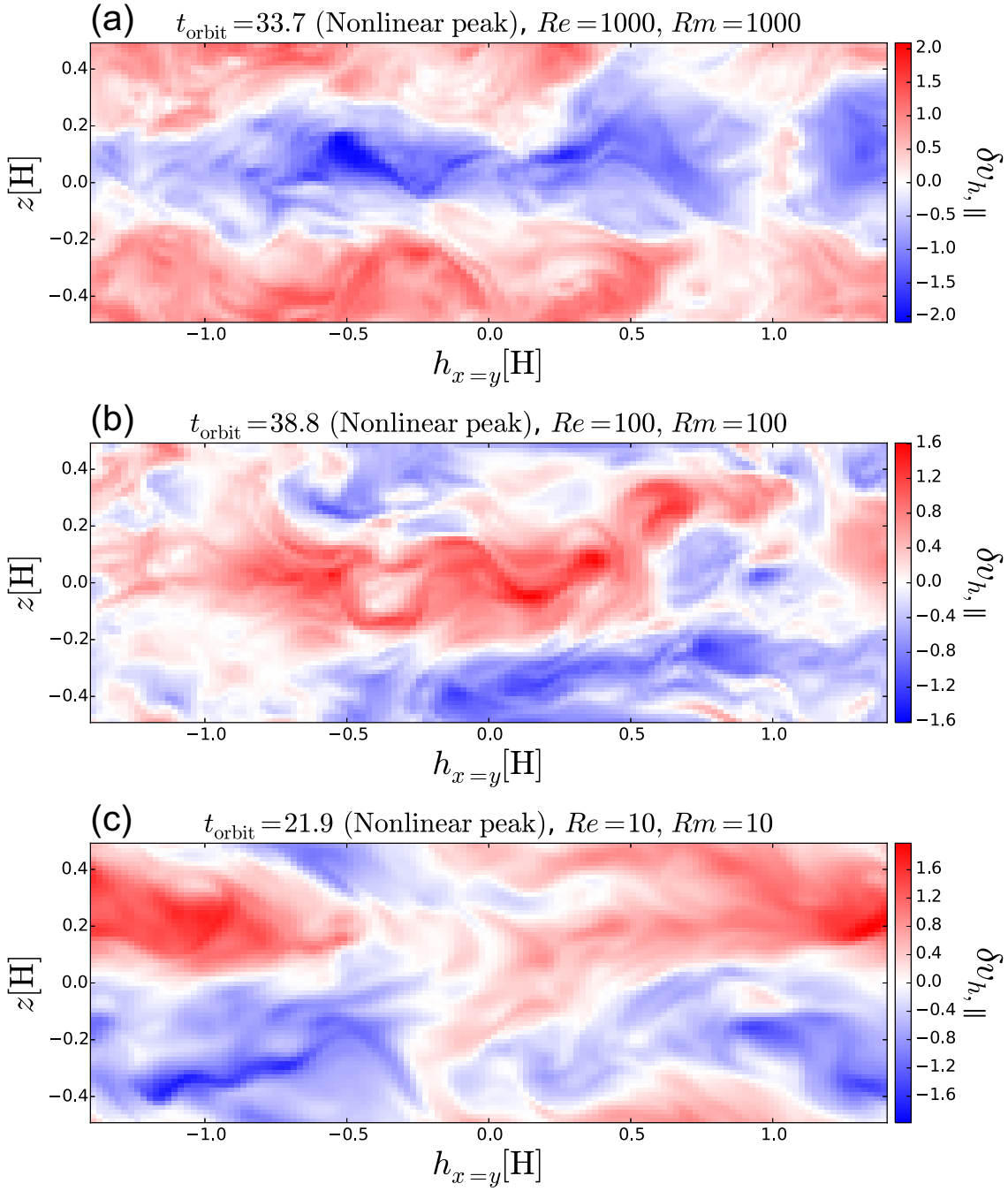

Fig. 4.17: Same as Figure 4.13 but at the time of nonlinear peak.

physical (Fromang et al., 2007) and numerical (Minoshima et al., 2015) diffusivities and magnetic Prandtl number (Lesur & Longaretti, 2007) change the time evolution of the spatially averaged turbulent stress. As shown in chapter 3, our newly developed MHD simulation code (chapter 2) reveal that the shear flow induced by MRI becomes small-scale and jet-like flow structures and collapses from these regions at the first peak, and the restructured shear flow in nonlinear phase seems to be collapsed by coexistence of the small-scale mixing and large scale vortices. Because the small amount of diffusivity only works to the small-scale structure, it can be expected that our code can capture what phenomena are modified by changing the diffusion effects at around peaks of turbulent stress.

We carried out three-dimensional MHD simulations with changing initial Reynolds number Re and initial magnetic Reynolds number Rm. The time evolution of turbulent stresses until the first peak in very low, low, and middle diffusivity models take almost the same value. This indicates that the saturation mechanism at the first peak obtained by lower diffusivity models are hardly modified, even though small diffusivities might change the small-scale flow and magnetic field structure. On the other hand, the turbulent stress at the first peak in the larger viscosity cases ($Re \sim 1$) take larger values and the timing of first peak is later than lower diffusivity models. This trend should reflect the quenching effect of K-H instability analytically shown by Pessah & Goodman (2009) and Pessah (2010). The time evolutions of stress after the first peak are different in all diffusivity models. Nonetheless, the amplitude of stress in lower diffusivity cases are not obviously different.

To study the trend of the values of the first peak, nonlinear peak, and temporally averaged value, we investigate these values in Re and Rm space. In the strong diffusivity cases ($Re, Rm \sim 1$), the viscosity increases the peak value at not only first peak but also peaks in nonlinear phase and the magnetic diffusivity increases the value only at first peak and does not affect (or decreases) the nonlinear peaks. These effects of viscosity and magnetic diffusivity seem to remain in the case of $Re, Rm \sim 100$ slightly. On the other hand, there is no trend of nonlinear peaks and averaged values in lower diffusivity cases ($Re, Rm \geq 100$). The dependence of magnetic Prandtl number is also not exist in our calculation, unlike Lesur & Longaretti (2007). The possible cause of this different feature from previous study is the setting of aspect ratio of simulation box. Pessah & Goodman (2009) reported the aspect ratio that cannot resolve parasitic instabilities induced by recurrently created channel flow causes the magnetic Prandtl number dependence of the sat-

uration value of turbulent stress. The aspect ratio of our simulation is suitable for resolving the parasitic instabilities induced by recurrently created channel flow, and thus, it is considered that there was no magnetic Prandtl number dependence in our calculation.

Next, we investigate detailed structure of the flow and its difference in several diffusivity models. At the first peak, wave enhancement of v_z directing 45 degrees from radial direction is observed in two-dimensional wavenumber space in $Re = Rm = 1000$ and $Re = Rm = 100$ diffusivity models. This is a similar feature to the results of ideal calculation. The direction of wave enhancement of B_z in the condition of $Re = Rm = 100$ is not 45 degrees but approximately 135 degrees though that angle in $Re = Rm = 1000$ is 45 degrees. In the case of $Re = Rm = 10$ model, not only B_z but also v_z have 135 degrees anisotropy. Theses results indicate that the dominant mode of parasitic instability is modified from K-H mode to magnetic reconnection mode by increasing magnetic diffusivity. In addition, the modification of fastest growth wavenumber is observed at first peak. The fastest growth wavenumber in the condition of $Re = Rm = 1000$ is larger than the theoretically obtained fastest growth wavenumber of parasitic instability, similarly to the result of ideal MHD. This wavenumber slightly becomes small in the condition of $Re = Rm = 100$, and take a similar value to the theoretical wavenumber of parasitic instability in the condition of $Re = Rm = 10$. These results indicate that the viscous effect controls the fastest growth wavelength of small-scale parasitic instability at the first peak. As shown in chapter 3, the layered flow becomes narrow due to vortices induced by the parasitic instability and that flow evolve small scale waves at the first peak. Viscous effect smoothen this small scale structure, and thus the fastest growth wavenumber becomes small when viscosity increases. From above results and discussions, we confirm the diffusion terms modify the distribution of wavenumber spectra at the first peak though the linear property of MRI is almost similar.

We also showed the analysis result at the nonlinear peak, which is arbitrarily chosen peak in fully developed turbulence. The 2-dimensional wavenumber spectra of both v_z and B_z at the nonlinear peak have 45 degree wave enhancement in all the $Re = Rm = 1000$, 100, and 10 models. Although the anisotropy is slightly different between the models, this fact indicates that the nonlinear peaks are generated mainly due to the K-H mode parasitic instability despite the existence of magnetic diffusivity. All of the flow structures of the $Re = Rm = 1000$, 100, and 10 models at the nonlinear peak have the restructured channels whose dominant wavelength

corresponds to the vertical box length. The difference between these three models are appeared as whether the smaller scale turbulent flow coexist. Comparing the trend analysis, we confirmed that the smoothing effects due to diffusivities slightly increases the value of nonlinear peak in relatively high diffusivity model such as $Re = Rm = 10$. On the other hand, we confirmed that smoothing effect hardly modify the value of nonlinear peak in relatively low diffusivity model such as $Re = Rm = 100$ and 10, though the wavenumber spectra and flow structures are slightly modified.

From our simulation and analysis, the excited structure of parasitic instability at the first peak is changed relatively largely due to the diffusion effect, but in the nonlinear peak it was shown that the diffusion effects hardly affect to both the average value of the stress and the structures of wavenumber spectra related to parasitic instability.

Chapter 5

Conclusion

We investigated the driving mechanism of the magnetic turbulence via the MRI and parasitic instability in accretion disks, and reveal the role of small-scale waves and flow structures for it by using the newly developed high-order MHD simulation code. The parasitic instability is non-axisymmetric instability (Goodman & Xu, 1994), thus the MHD simulation is required to be three-dimensional calculation. In addition, previous analytical and numerical studies (e.g., Latter et al., 2009; Rembiasz et al., 2016) suggested that the MHD simulation also required to be compressible and have efficiency to resolve small scale waves and flow structures. In order to realize the requirements, we newly developed a three-dimensional parallelized MHD simulation code by using the high-order MHD scheme proposed by Kawai (2013). We applied the shearing box approximation (Hawley et al., 1995) to the code and carried out local disk simulations with the ideal MHD condition and several visco-resistive MHD conditions.

5.1 Development of the three-dimensional parallelized high-order MHD simulation code

Since we focused on resolving MRI-driven magnetic turbulence accurately, we developed the MHD simulation code by employing the MHD scheme proposed by Kawai (2013). This scheme is based on the high-order compact difference scheme (Lele, 1992) and high-order compact-type filtering scheme (Lele, 1992; Gaitonde & Visbal, 2000), and localized artificial diffusivity (LAD) method. Since the compact difference and compact-type filtering schemes require doing sequential calculation and thus they can not be simply parallelized by domain decomposition using MPI,

we employed the pipeline algorithm to parallelize without diminishing the accuracy. The developed code is successfully parallelized by using this algorithm and the acceleration ratio is increased by increasing the number of processes. We carried out some numerical tests and confirmed that developed code has following capabilities; high wavenumber accuracy, i.e., the code can solve the wave propagation with a few grids per wavelength, capturing discontinuities accurately, i.e., the calculation is not broken by numerical noise, and conservation of the solenoidal condition, i.e., $\boldsymbol{\nabla} \cdot \boldsymbol{B}$ is suppressed in machine error level as long as we use periodic boundary conditions. From these numerical tests, we could confirm that developed code works properly and has the capabilities for resolving MRI-driven turbulence.

5.2 Driving mechanism of turbulence and the role of small-scale flow in ideal MHD condition

We applied the developed code to the local disk model by using the shearing box approximation (Hawley et al., 1995), and carried out three-dimensional ideal MHD simulation of MRI-driven turbulence. We observed that spatially averaged turbulent stress repeatedly increase and decrease after the first saturation. We defined the initial saturation of the stress as 'first peak' and arbitrarily chosen peak created in fully developed turbulence as 'nonlinear peak', and investigated detailed structure at these two peaks.

5.2.1 Mechanisms of peak creation and driving turbulence at the first peak

We showed the anisotropic wave enhancement in two-dimensional wavenumber spectra of vertical velocity due to the excitation of parasitic instability at the first peak. The fastest enhancement wavenumber is much larger than that obtained analytically, and this feature is similar result to Rembiasz et al. (2016) though they assumed different setting from ours. We found that this feature is because the interaction of vertically located growing vortices induced by parasitic instability makes the layered structure of disturbed flow narrower and faster, and then the jet-like structure induces much smaller and faster growing K-H-like instability just before the peak. This newly induced small-scale instability tears off the MRI-created layered flow structure and thus the turbulent stress decreases. The first

peak creation process in our simulation is summarised as follows. First, MRI is linearly grows and results in layered structures of disturbed field. Meanwhile, K-H mode parasitic instability grows and results in a few vortices. Then, the vertically located vortices make the layered flow structure narrower and faster. Finally, the created jet-like structure becomes unstable and the layered structure tears off, and thus the turbulent stress decreases.

5.2.2 Mechanisms of peak creation and driving turbulence at the nonlinear peak

We also showed the analysis results of the arbitrarily chosen nonlinear peak at $t_{\rm orbit} \sim 29.8$ to discuss the creation mechanism of the peak and the difference from the first peak. The anisotropic wave enhancement of parasitic instability is observed in two-dimensional wavenumber spectra of vertical velocity. The anisotropic spectra is, however, found only in the small wavenumber region, while large wavenumber waves are more isotropic than those at the first peak. This indicates that a nonlinear peak is created in an environment where large-scale and anisotropic parasitic mode waves and isotropic turbulent waves coexist. The restructured channel flow starts to collapse at the nonlinear peak, but the mechanism is not obvious because of the existence of the small-scale turbulent structure. We showed that large-scale vortices induced by restructured flow effectively advect small-scale shear structures from the shear region toward the flow region of the restructured channel, and the advected structure seems to mix and break the restructured channel structure.

We determined that the peak creation and driving magnetic turbulence mechanism, i.e., the collapse mechanism of channel flow structure, is related to the destruction of large-scale structure by small-scale flow in both linear phase and nonlinear phase.

5.3 Driving mechanism of turbulence and the role of small-scale flow in visco-resistive MHD conditions

We investigated the physical diffusion effects to the turbulent stress and peak creation mechanism. Because the small amount of diffusivity only works to the small-scale structure, we would like to reveal what phenomena are modified by changing the diffusion effects at around peaks of turbulent stress by developed

high-order code. We carried out three-dimensional MHD simulations with changing initial Reynolds number Re and initial magnetic Reynolds number Rm. The time evolution of turbulent stresses until the first peak take almost the same value in the case of lower diffusivities. On the other hand, the turbulent stress at the first peak in the larger viscosity cases ($Re \sim 1$) take larger values and its time of first peak is later than lower diffusivity models. This trend should reflect the quenching effect of K-H instability analytically shown by Pessah & Goodman (2009) and Pessah (2010). The time evolutions of stress after the first peak are different in all diffusivity models.

To see the trend of the values of the first peak, nonlinear peak, and temporally averaged value, we investigate these values in Re and Rm space. In the strong diffusivity cases ($Re, Rm \sim 1$), the viscosity increases the peak value at not only first peak but also peaks in nonlinear phase and the magnetic diffusivity increases the value only at first peak and does not affect (or decreases) the nonlinear peaks. On the other hand, there is no trend of nonlinear peaks and averaged values in lower diffusivity cases ($Re, Rm \geq 100$). The dependence of magnetic Prandtl number is also not exist in our calculation, unlike Lesur & Longaretti (2007). The possible cause of this different feature from previous study is the setting of aspect ratio of the simulation box. Pessah & Goodman (2009) reported the aspect ratio that cannot resolve parasitic instabilities induced by recurrently created channel flow causes the Prandtl number dependence of the saturation value of turbulent stress. The aspect ratio of our simulation is suitable for resolving the parasitic instabilities induced by recurrently created channel flow, and thus, it is considered that there was no magnetic Prandtl number dependence in our calculation.

5.3.1 Mechanisms of peak creation and driving turbulence at the first peak in visco-resistive MHD

We investigated detailed structure of the flow and its difference in several diffusivity models. At the first peak, wave enhancement of v_z directing 45 degrees from radial direction is observed in two-dimensional wavenumber space in $Re = Rm = 1000$ and $Re = Rm = 100$ diffusivity models. This is a similar feature to the results of ideal calculation. The direction of wave enhancement of B_z in the condition of $Re = Rm = 100$ is not 45 degrees but approximately 135 degrees though that angle in $Re = Rm = 1000$ is 45 degrees. In the case of $Re = Rm = 10$ model, not only B_z but also v_z have 135 degrees anisotropy. Theses results indicate that the dominant

mode of parasitic instability is modified from K-H mode to magnetic reconnection mode by increasing magnetic diffusivity. In addition, the modification of fastest growth wavenumber is observed at first peak. The fastest growth wavenumber in the condition of $Re = Rm = 1000$ is larger than the theoretically obtained fastest growth wavenumber of parasitic instability, similarly to the result of ideal MHD. This wavenumber slightly becomes small in the condition of $Re = Rm = 100$, and take a similar value to the theoretical wavenumber of parasitic instability in the condition of $Re = Rm = 10$. These results indicate that the viscous effect controls the fastest growth wavelength at the first peak. As shown in chapter 3, the layered flow becomes narrow due to vortices induced by the parasitic instability and that flow evolve small scale waves at the first peak. Viscous effect smoothen this small scale structure, and thus the fastest growth wavenumber becomes small when viscosity increases. From above results and discussions, we conclude that the diffusion terms modify the distribution of wavenumber spectra at the first peak though the linear property of MRI is almost similar.

5.3.2 Mechanisms of peak creation and driving turbulence at the nonlinear peak in visco-resistive MHD

We also showed the analysis result at the nonlinear peak, which is arbitrarily chosen peak in fully developed turbulence. The 2-dimensional wavenumber spectra of both v_z and B_z at the nonlinear peak have 45 degree wave enhancement in all the $Re = Rm = 1000$, 100, and 10 models. Although the anisotropy is slightly different between the models, this fact indicates that the nonlinear peaks are generated mainly due to the K-H mode parasitic instability despite the existence of magnetic diffusivity. All of the flow structures of $Re = Rm = 1000$, 100, and 10 models at the nonlinear peak have the restructured channels whose dominant wavelength correspond to the vertical box length. The difference between these three models are appeared as whether the smaller scale turbulent flow coexist. Comparing the trend analysis, we confirmed that the smoothing effects due to diffusivities slightly increases the value of nonlinear peak in relatively high diffusivity model such as $Re = Rm = 10$. On the other hand, we concluded that smoothing effect hardly modify the value of nonlinear peak in relatively low diffusivity model such as $Re = Rm = 100$ and 10, though the wavenumber spectra and flow structures are slightly modified.

From our simulation and analysis, the excited structure of parasitic instability

and driving mechanism of turbulence at the first peak is changed relatively largely due to the diffusion effects. The diffusion effects hardly affect to the spatially averaged value of the stress. The modification of structures of wavenumber spectra related to parasitic instability at the nonlinear peak due to the diffusion effects seems relatively weaker than that identified at the first peak. The small-scale flow structures, however, are significantly modified by diffusion effects though the spatially averaged stresses take similar values. These facts indicate that spatially (and temporally) averaged turbulent stress, i.e., α parameter, is determined only by large-scale channel and is less sensitive to the effects of small-scale turbulent structure. We conclude that the high precision MHD simulation is particularly required for the precise study of the detailed structure and time evolutional process of MRI-driven turbulence (and possibly the evaluation of mass accretion rate).

5.4 Application of this study

Throughout this study, we have investigated how the small-scale waves and flow structures evolve at the peaks of spatially averaged turbulent stress and affect the large-scale structure through the use of the newly developed MHD simulation code. Our ideal simulation revealed that the enhancement or coexisting waves smaller than the typical wavelengths of MRI and parasitic instability result in breakdown of large-scale structures at the peaks of the turbulent stress. In addition, although the effect of a small amount of diffusion is seen at the first peak, our visco-resistive simulation also revealed that the value of the temporally and spatially averaged stress hardly changes despite the modification of flow structure due to the diffusion effect. Our simulation results revealed that the flow structure itself can be strongly affected due to the effect of the physical and numerical diffusivity even if the temporally averaged stress takes similar values. Therefore, estimation of the disk structure using turbulent stress becomes inappropriate for studies that focus on the turbulent flow itself.

One of the example is simulation studies of the planetesimal formation in protoplanetary disks. Johansen et al. (2011) and Kato et al. (2012) carried out the MHD+dust simulation which solve the MRI-driven turbulence and the motions of dust in such a turbulent state simultaneously, and reported that the dusts are accumulated at the specified region by the interaction with the turbulent flow, and that helps the formation of planetesimals In addition, Kimura et al. (2016) carried out the MHD+test particle simulation and investigated the particle acceleration in

the MRI-driven turbulence. These types of simulations focus on the turbulent flow itself, and thus it is required to solve turbulence accurately. Therefore, it is considered that it becomes important to solve not only the temporally and spatially averaged turbulent stress but also the turbulent flow and wavenumber spectrum accurately, as our simulation results and developed code revealed the importance clearly.

References

Armitage, P. J. 2007, Arxiv preprint astro-ph/0701485, arXiv:0701485v3

Balbus, S. A., & Hawley, J. F. 1991, The Astrophysical Journal, 376, 214

—. 1998, Reviews of Modern Physics, 70, 1

Blaes, O. M., & Balbus, S. A. 1994, The Astrophysical Journal, 421, 163

Bodo, G., Mignone, A., Cattaneo, F., Rossi, P., & Ferrari, A. 2008, Astronomy and Astrophysics, 487, 1

Brio, M., & Wu, C. C. 1988, Journal of Computational Physics, 75, 400

Cook, A. W., & Cabot, W. H. 2004, Journal of Computational Physics, 195, 594

Dedner, A., Kemm, F., Kröner, D., et al. 2002, Journal of Computational Physics, 175, 645

Fromang, S., & Papaloizou, J. 2007, Astronomy and Astrophysics, 476, 1113

Fromang, S., Papaloizou, J., Lesur, G., & Heinemann, T. 2007, Astronomy and Astrophysics, 476, 1123

Fukue, J., Wada, K., & Umemura, M. 2014, Fundamentals in Astrophysical Fluid Dynamics (Nihonhyoronsha)

Gaitonde, D. V., & Visbal, M. R. 2000, AIAA Journal, 38, 2103

Goodman, J., & Xu, G. 1994, The Astrophysical Journal, 432, 213

Hartmann, L. 2001, Workshop on Cool Stars, Stellar Systems and the ...

Hartmann, L., Calvet, N., Gullbring, E., & D'Alessio, P. 1998, The Astrophysical Journal, 495, 385

Hawley, J. F., & Balbus, S. A. 1992, The Astrophysical Journal, 400, 595

Hawley, J. F., Gammie, C. F., & Balbus, S. A. 1995, The Astrophysical Journal, 440, 742

Jaffe, W., Ford, H. C., Ferrarese, L., van den Bosch, F., & O'Connell, R. W. 1993, Nature, 364, 213

Jin, L. 1996, The Astrophysical Journal, 457, 798

Johansen, A., Klahr, H., & Henning, T. 2011, Astronomy & Astrophysics, 529, A62

Kato, M., Fujimoto, M., & Ida, S. 2012, The Astrophysical Journal, 747, 11

Kawai, S. 2013, Journal of Computational Physics, 251, 292

Kawai, S., & Lele, S. K. 2008, Journal of Computational Physics, 227, 9498

Kawai, S., Shankar, S. K., & Lele, S. K. 2010, Journal of Computational Physics

Kimura, S. S., Toma, K., Suzuki, T. K., & Inutsuka, S.-i. 2016, The Astrophysical Journal, 822, 88

Latter, H. N., Lesaffre, P., & Balbus, S. a. 2009, Monthly Notices of the Royal Astronomical Society, 394, 715

Lele, S. K. 1992, Journal of Computational Physics, 103, 16

Lesur, G., & Longaretti, P. Y. 2007, Monthly Notices of the Royal Astronomical Society, 378, 1471

Lesur, G., & Longaretti, P.-Y. 2011, Astronomy & Astrophysics, 528, A17

Machida, M. N. 2014, The Astrophysical Journal, 796, L17

Mani, A., Larsson, J., & Moin, P. 2009, Journal of Computational Physics, 228, 7368

Masada, Y., Kawanaka, N., Sano, T., & Shibata, K. 2007, The Astrophysical Journal, 663, 437

Masada, Y., & Sano, T. 2008, The Astrophysical Journal, 689, 1234

Matsumoto, Y., & Hoshino, M. 2004, Geophysical Research Letters, 31, L02807

Matsumoto, Y., Asahina, Y., Kudoh, Y., et al. 2016, ArXiv e-prints, 1

Matsuura, K., & Kato, C. 2007, AIAA Journal, 45, 442

McCaughrean, M. J., & O'dell, C. R. 1996, The Astronomical Journal, 111, 1977

Mignone, A., Bodo, G., Massaglia, S., et al. 2007, The Astrophysical Journal Supplement Series, 170, 228

Minoshima, T., Hirose, S., & Sano, T. 2015, The Astrophysical Journal, 808, 54

Murphy, G. C., & Pessah, M. E. 2015, The Astrophysical Journal, 802, 139

Nornberg, M. D., Ji, H., Schartman, E., Roach, A., & Goodman, J. 2010, Physical Review Letters, 104, 7

Pessah, M. E. 2010, The Astrophysical Journal, 716, 1012

Pessah, M. E., & Chan, C.-k. 2008, The Astrophysical Journal, 684, 498

Pessah, M. E., & Goodman, J. 2009, The Astrophysical Journal, 698, L72

Rembiasz, T., Obergaulinger, M., Cerdá-Durán, P., Müller, E., & Aloy, M. A. 2016, Monthly Notices of the Royal Astronomical Society, 456, 3782

Romanova, M. M., Ustyugova, G. V., Koldoba, a. V., & Lovelace, R. V. E. 2011, Monthly Notices of the Royal Astronomical Society, 438, no

Romanova, M. M., Ustyugova, G. V., Koldoba, A. V., & Lovelace, R. V. E. 2012,

Monthly Notices of the Royal Astronomical Society, 421, no

Ryu, D., & Jones, T. 1995, The Astrophysical Journal

Sai, K., Katoh, Y., Terada, N., & Ono, T. 2013, The Astrophysical Journal, 767, 165

Sano, T., & Inutsuka, S.-i. 2001, The Astrophysical Journal, 561, L179

Sano, T., & Miyama, S. M. 1999, The Astrophysical Journal, 515, 776

Sano, T., Miyama, S. M., Umebayashi, T., & Nakano, T. 2000, The Astrophysical Journal, 543, 486

Shakura, N. I., & Sunyaev, R. a. 1973, Astronomy and Astrophysics, 24, 337

Shi, J., Krolik, J. H., & Hirose, S. 2010, The Astrophysical Journal, 708, 1716

Stone, J. M., Gardiner, T. a., Teuben, P., Hawley, J. F., & Simon, J. B. 2008, The Astrophysical Journal Supplement Series, 178, 137

Stone, J. M., Hawley, J. F., Gammie, C. F., & Balbus, S. A. 1996, The Astrophysical Journal, 463, 656

Suzuki, T. K., & Inutsuka, S.-i. 2009, The Astrophysical Journal, 691, L49

Terashima, H., Kawai, S., & Koshi, M. 2013, Computers & Fluids, 88, 484

Tomida, K., Tomisaka, K., Matsumoto, T., et al. 2013, The Astrophysical Journal, 763, 6

Tóth, G. 2000, Journal of Computational Physics, 161, 605

Umebayashi, T., & Nakano, T. 1988, Progress of Theoretical Physics Supplement, 96, 151

Zenitani, S., & Miyoshi, T. 2011, Physics of Plasmas, 18, 022105